

1-1-2009

Molecular Structures And Pulsed Discharge Emission Studies Of Volatile Organic Compound Derivatives

Ashley Osthoff

Eastern Illinois University

This research is a product of the graduate program in [Chemistry](#) at Eastern Illinois University. [Find out more](#) about the program.

Recommended Citation

Osthoff, Ashley, "Molecular Structures And Pulsed Discharge Emission Studies Of Volatile Organic Compound Derivatives" (2009). *Masters Theses*. 85.
<http://thekeep.eiu.edu/theses/85>

This Thesis is brought to you for free and open access by the Student Theses & Publications at The Keep. It has been accepted for inclusion in Masters Theses by an authorized administrator of The Keep. For more information, please contact tabruns@eiu.edu.

THESIS MAINTENANCE AND REPRODUCTION CERTIFICATE

TO: Graduate Degree Candidates (who have written formal theses)

SUBJECT: Permission to Reproduce Theses

The University Library is receiving a number of request from other institutions asking permission to reproduce dissertations for inclusion in their library holdings. Although no copyright laws are involved, we feel that professional courtesy demands that permission be obtained from the author before we allow these to be copied.

PLEASE SIGN ONE OF THE FOLLOWING STATEMENTS:

Booth Library of Eastern Illinois University has my permission to lend my thesis to a reputable college or university for the purpose of copying it for inclusion in that institution's library or research holdings.



Author's Signature

10/3/2009

Date

I respectfully request Booth Library of Eastern Illinois University **NOT** allow my thesis to be reproduced because:

Author's Signature

Date

This form must be submitted in duplicate.

Molecular Structures and Pulsed Discharge Emission Studies of

Volatile Organic Compound Derivatives

(TITLE)

BY

Ashley Osthoff

THESIS

SUBMITTED IN PARTIAL FULFILLMENT OF THE REQUIREMENTS
FOR THE DEGREE OF

Master of Science in Chemistry

IN THE GRADUATE SCHOOL, EASTERN ILLINOIS UNIVERSITY
CHARLESTON, ILLINOIS

2009

YEAR

I HEREBY RECOMMEND THAT THIS THESIS BE ACCEPTED AS FULFILLING
THIS PART OF THE GRADUATE DEGREE CITED ABOVE

Tom J. Decker 12/3/09
THESIS COMMITTEE CHAIR DATE

Mark E M. Quinn 12/3/09
DEPARTMENT/SCHOOL CHAIR DATE
OR CHAIR'S DESIGNEE

Sean A. Keebler 12/3/09
THESIS COMMITTEE MEMBER DATE

Edward M. Freadwell 12/3/09
THESIS COMMITTEE MEMBER DATE

Barbara Lawrence 12/3/09
THESIS COMMITTEE MEMBER DATE

THESIS COMMITTEE MEMBER DATE

Dedicated to my parents Kelly Kress and Roger Osthoff, and my husband Nathan Elliott.
Completion of this work would not have been possible without them.

Acknowledgements

The author would like to acknowledge Dr. Rebecca Peebles for all of the helpful advice over the course of the research included in this work as well as the work itself.

Also, the author would also like to acknowledge her thesis committee members Dr. Sean Peebles, Dr. Edward Treadwell and Dr. Barbara Lawrence.

Abstract

Understanding the structure and reactivity of volatile organic compounds (VOCs), hydrochlorofluorocarbons (HCFCs) and their derivatives is a fundamental concern in the study of atmospheric chemistry. Recently, a series of studies were done aimed at constructing and optimizing a rapid-scan, midinfrared spectrometer in order to study the structure and intermolecular interactions of these compounds. Visible emission spectroscopy was used to optimize the pulsed discharge nozzle that would be used within the infrared spectrometer. The emission spectra of toluene and xylene were used to characterize production of free radical compounds. In addition, control programs were written in the LabVIEW programming language to control the emission spectrometer and nozzle.

Fourier-transform and chirped-pulse Fourier-transform microwave spectroscopy were used to study the gas phase VOC derivatives 2,3,4,5,6-pentafluorotoluene, or PFTOL, and 1-chloro-2,3,4,5,6-pentafluorobenzene, or CPFB. These microwave studies were done to gain background information on the pentafluorobenzyl radical precursor, PFTOL. Heavy-atom structures of both compounds were determined using assigned rotational constants for all single ^{13}C isotopologues. The ground state rotational constants for PFTOL are $A = 1036.61221(15)$ MHz, $B = 1030.94086(16)$ MHz, and $C = 516.92066(11)$ MHz. The ground state rotational constants for CPFB are $A = 1028.5412(2)$ MHz, $B = 751.82072(17)$ MHz and $C = 434.3531(3)$ MHz for ^{35}Cl and $A = 1028.5439(7)$

MHz, $B = 734.47954(18)$ MHz and $C = 428.5081(2)$ MHz for ^{37}Cl . These spectra are to be compared with chlorobenzene, toluene and pentafluorobenzene to observe the effects on the structure of the benzene ring when substituting a chlorine atom for a methyl group. Through these studies, PFTOL is estimated to have a low energy barrier (<1 kJ/mol) to internal rotation. Also, the $\angle(\text{C}_5\text{-C}_6\text{-C}_1)$ angle is decreased from the predicted 120° in both PFTOL and CPFEB, seemingly due to effects from the fluorine atoms present around the ring.

TABLE OF CONTENTS

CHAPTER 1: INTRODUCTION	1
1.1 INITIAL CONCEPTS	1
1.1.1 <i>Introduction to Infrared Spectroscopy</i>	2
1.2 BACKGROUND OF INFRARED PROJECT	6
1.3 EMISSION SPECTROSCOPY EXPERIMENT	10
1.4 MICROWAVE STUDIES	13
REFERENCES: CHAPTER 1	16
CHAPTER 2: EXPERIMENTAL	17
2.1 PULSED DISCHARGE NOZZLE EMISSION SPECTROSCOPY	17
2.2 MICROWAVE SPECTROSCOPY	20
2.3 EXPERIMENTAL DETAILS	25
REFERENCES: CHAPTER 2	33
CHAPTER 3: EMISSION SPECTROSCOPY STUDIES OF VOLATILE ORGANIC COMPOUND DERIVATIVES	35
3.1 INTRODUCTION	35
3.2 SOFTWARE DEVELOPMENT	38
3.2.1: <i>PMT and Nozzle Programs</i>	38
3.2.2: <i>Instrument Control and Optimization Programs</i>	41
3.2.3: <i>Early testing of the program</i>	46
3.2.4: <i>Iodine</i>	51
3.3 TOLUENE	56
3.4 XYLENE	59
3.5 RESULTS AND CONCLUSIONS	60
REFERENCES: CHAPTER 3	66
CHAPTER 4: MICROWAVE SPECTROSCOPY OF PENTAFLUOROTOLUENE	67
4.1 INTRODUCTION	67
4.1.1: <i>Stark Effect Measurements</i>	68
4.1.2: <i>Internal Rotation</i>	69
4.2 MEASUREMENT OBSERVATIONS	70
4.3 RESULTS	74
CHAPTER 4: REFERENCES	86
CHAPTER 5: MICROWAVE SPECTROSCOPY OF CHLOROPENTAFLUOROBENZENE	87
5.1 INTRODUCTION	87
5.2 MEASUREMENT OBSERVATIONS	89
5.3 RESULTS	91
REFERENCES: CHAPTER 5	102
CHAPTER 6: DISCUSSION AND CONCLUSIONS	103
6.1 DISCUSSION OF STRUCTURAL RESULTS	103
6.2 FUTURE WORK	111
6.3 CONCLUSIONS	112
REFERENCES: CHAPTER 6	114
APPENDIX A – CONSTANTS AND VARIABLES	I
APPENDIX B – LABVIEW CONTROLS, INDICATORS AND FUNCTIONS	IV
APPENDIX C – LABVIEW PROGRAMS	IX

List of Figures

Figure 1.1: An energy plot for the harmonic oscillator model for vibration showing energy levels and wave functions. $V_{(r)}$ represents the energy while r represents the displacement from the equilibrium distance, r_e , of the bond.....	4
Figure 1.2: Rotational transitions within the $\Pi_u - \Sigma^+_g$ infrared vibrational transition of a linear polyatomic molecule.....	5
Figure 1.3: The $3^1_0, \Sigma^+ - \Sigma^+$ infrared band of HCN along with two overlapping bands which are much weaker. P and R branches such as the ones that are discussed above are displayed.....	5
Figure 1.4: Schematic of the experimental set-up of the rapid-scan midinfrared spectrometer used by DePiante, et al.....	7
Figure 1.5: Schematic of the infrared spectrometer built by McKellar, et al.....	8
Figure 1.6: Timing sequence for the data acquisition cycle used with the instrument constructed by McKellar, et al. Data acquisition is controlled by the laser settings and triggered by the ramp peak shown by the top signal.....	9
Figure 1.7: Reaction scheme for the destruction of ozone into the OH radical...	11
Figure 1.8: The molecular structure of the pentafluorobenzyl radical.....	13
Figure 1.9: The molecular structure of 2,3,4,5,6-pentafluorotoluene (left) and of 1-chloro-2,3,4,5,6-pentafluorobenzene (right).....	15
Figure 2.1: Vibrational progressions within the electronic spectrum of a diatomic molecule.....	19
Figure 2.2: Methyl Iodide; an example of a prolate rotor.....	23
Figure 2.3: Benzene; an example of an oblate rotor.....	23
Figure 2.4: Rotational energy levels for a prolate rotor (a) and an oblate rotor (b).....	24
Figure 2.5: Block diagram of the pulsed discharge nozzle, showing the electrodes used as well as their orientation within the nozzle body.....	26

Figure 2.6: Block diagram of the visible emission spectrometer at EIU. The nozzle acts as the sample source while the monochromator selects the appropriate wavelength to be detected by the PMT.....	27
Figure 2.7: Schematic of the Balle-Flygare type FTMW spectrometer located at EIU, showing the relative microwave source, supersonic expansion chamber and detector locations.....	28
Figure 2.8: Schematic of the CP-FTMW located at the University of North Texas. In this spectrometer, the microwave frequency range is created by 1 and 2, sent into the expansion chamber indicated by 16 and finally detected by the oscilloscope indicated by number 12.....	30
Figure 2.9: Schematic of the CP-FTMW located at the University of Virginia. The microwave pulse generation is contained in the box labeled 1), with excitation taking place within the box labeled 2), and finally detected by the scope within 3). This spectrometer contains a larger waveform generator and oscilloscope than the instrument in Figure 2.8 resulting in a broader frequency range used.....	31
Figure 3.1: Diagram of the pulsed discharge nozzle used by the Zwier group, showing similarity to the EIU nozzle (Figure 2.5).....	37
Figure 3.2: a) Block diagram and b) front panel of the <u>PMTmeas.vi</u> program. The waveform chart shows data being collected in real time and the waveform graph shows the final spectrum, in this case of argon. Also note the controls for Number of Scans, PMT Delay and Path.....	40
Figure 3.3: a) Block diagram and b) front panel of the <u>NozzleFire.vi</u> program. Note the controls for the High Time, Low Time and Initial Delay of the Nozzle...	42
Figure 3.4: Block diagram of the <u>MainControl2.vi</u> program, showing where <u>PMTmeas.vi</u> and <u>NozzleFire.vi</u> (shown by their names on the diagram) have been integrated into a case structure.....	43
Figure 3.5: Front panel of the <u>MainControl2.vi</u> program. All controls and functions below the "Scan Parameters" section originate from the written VIs and were integrated into the provided monochromator VI. Note the regions corresponding to nozzle and PMT control with controls and indicators corresponding to Figure 3.3 and Figure 3.4.....	44
Figure 3.6: Hydrogen spectrum from the atomic discharge lamp source showing early results that the program was working as intended. The literature line spectrum is shown superimposed.....	47

Figure 3.7: Emission spectrum of mercury using an atomic discharge lamp. This spectrum showed a need to adjust the intensity limit of the PMT as the strong two lines are actually one line split in the center. Literature line spectrum is shown superimposed.....	49
Figure 3.8: Emission spectrum of helium using an atomic discharge lamp. The accuracy of this spectrum indicated that the program was working properly and the PDN could be integrated. Literature line spectrum is shown superimposed.....	51
Figure 3.9: Emission spectrum of the argon carrier gas in the 700 – 800 nm region. Literature line spectrum is shown superimposed.....	52
Figure 3.10: Emission spectrum of iodine in the 300 – 320 nm region indicating that the PDN was working properly. Literature line spectrum is shown superimposed.....	55
Figure 3.11: Emission spectrum of iodine in the 610 – 630 nm region indicating that the PDN was working properly. Literature line spectrum is shown superimposed.....	55
Figure 3.12: Emission spectrum of the discharge products of toluene in the 400 – 450 nm region.....	57
Figure 3.13: Emission spectrum of the discharge products of xylene in the 400 – 500 nm region.....	60
Figure 3.14: Toluene emission data by controlled electron impact ^[11] . Wavelength data is displayed in nm. H and CH fragments in the 400 – 450 nm region seem to match toluene and xylene PDN data.....	61
Figure 3.15: Comparison of the 400 – 450 nm region of the discharge products of toluene and xylene. The blue line represents toluene data with the red line indicating xylene data. Both compounds have a similar pattern in this region indicating that the discharge products for both compounds are similar.....	62
Figure 3.16: Emission spectrum of C ₂ in the 465 – 475 nm region. Wavelengths are displayed in angstroms, (Å). This pattern appears to match weak transitions in the xylene spectrum around 470 nm.....	64
Figure 4.1: An example of transition grouping found in the rotational spectrum of pentafluorotoluene. Within this series, each ΔJ value is equal to +1. This pattern is indicative of an oblate molecule.....	71

Figure 4.2: One portion of the Q-branch found in the rotational spectrum of pentafluorotoluene. Only once this branch was assigned were the distortion constants able to be determined.....	72
Figure 4.3: Example of transition splitting occurring throughout the spectrum. Transition (a) shows Doppler splitting characteristic of axial nozzle configuration. Transition (b) shows same splitting with additional small splitting of around 16 kHz due to internal rotation.....	73
Figure 4.4: A portion of the broadband spectrum of PFTOL with torsionally excited states indicated. Frequency scale represents the frequency offset from the center frequency of 9800 MHz.....	74
Figure 4.5: Structure of pentafluorotoluene.....	80
Figure 4.6: StrfitQ input structures for CPF. The first input structure is seen in (a) with the second input structure represented in (b). Both structures were needed due to complications with the program in closing the aromatic rings.....	81
Figure 4.7: Plot used to extrapolate the reduced energy barrier, s , based on Appendix C of Herschbach P_{cc} present in units of ($\mu * \text{\AA}^2$).....	84
Figure 5.1: Comparison of broadband spectrum between (b) initial acquisition and (a) second acquisition with bandpass filter added. ^{13}C isotopologue lines are shown in the center inset and good measurement of these lines was a result of the improved S/N ratio.....	89
Figure 5.2: Unresolved hyperfine components due to nuclear quadrupole coupling in chloropentafluorobenzene.....	91
Figure 5.3: Structure and axes of chloropentafluorobenzene.....	99
Figure 6.1: Comparison of pentafluorotoluene vs chloropentafluorobenzene. The main structural observation obtained from this analysis was angle distortion located at the $\langle \text{C}_5\text{-C}_6\text{-C}_1 \rangle$ angle.....	104
Figure 6.2: Experimental structure of toluene ^[2] . Notice that the purple angle, corresponding to the distorted angle in PFTOL and CPF is closer to the predicted 120°	106
Figure 6.3: Electrostatic potential maps calculated to observe electronegative substituent effects. Colors range from blue, which indicates a positive electrostatic potential, to red, indicating a negative electrostatic potential.....	110

List of Tables

Table 3.1: Peaks from hydrogen spectrum compared to literature data. Uncertainties in experimental data are around +/- 1.0 nm.....	47
Table 3.2: Peaks from the mercury spectrum compared to literature data. Uncertainties in experimental data are around +/- 1.0 nm.....	48
Table 3.3: Helium emission peaks compared to literature data. Uncertainties in experimental data are around +/- 1.0 nm.....	50
Table 3.4: Argon emission peaks compared to literature data. Uncertainties in experimental data are around +/- 1.0 nm.....	52
Table 3.5: Iodine emission peaks compared to literature data. Uncertainties in experimental data are around +/- 0.1 nm.....	54
Table 3.6: Toluene and Xylene emission peaks compared to literature data ^[11] on emission products from electron impact experiments. Uncertainty for wavelength measurements was around +/- 0.1 nm.....	58
Table 4.1: Measured transitions of the normal species of pentafluorotoluene...	75
Table 4.2: Spectroscopic constants of pentafluorotoluene. See Figure 4.5 for atom numbering.....	77
Table 4.3: Pentafluorotoluene principal axis coordinates (Å) of the carbon atom framework. See figure 4.5 for atom numbers.....	80
Table 4.4: Bond distances and angles of pentafluorotoluene.....	81
Table 4.5: Dipole moment determinations of pentafluorotoluene. $J - J^p$ and M columns represent different combinations of fits that were used to fit μ	83
Table 5.1: Measured transitions of the normal species of CPF B.....	92
Table 5.2: Spectroscopic constants determined for chloropentafluorobenzene. See Figure 5.3 for atom numbering.....	97
Table 5.3: Principal axis coordinates (Å) for the carbon atom framework of CPF B. (italic values represent <i>ab initio</i> calculations).....	100
Table 5.4: Bond distances and angles determined for CPF B.....	100

Table 6.1: Comparison of PFTOL, CPFB and Toluene ^[2] values. Previous angle distortion in PFTOL and CPFB is not seen in the toluene structure.....	103
Table 6.2: Comparison of <i>ab initio</i> values of PFTOL to pentafluorobenzene...	108
Table 6.3: Comparison of CPFB to chlorobenzene.....	108

Chapter 1: Introduction

1.1 Initial concepts

Recently, work in the Peebles laboratory at Eastern Illinois University (EIU) has focused on studying the rovibrational spectra of weakly-bound complexes and free radical species to determine the structure and intermolecular interactions of these compounds. The types of molecules which will be involved in future studies at EIU are volatile organic compounds, hydrochlorofluorocarbons and their derivatives. These types of molecules are of interest due to their high concentration in pollution emissions into the atmosphere^[1]. Characterizing the structure and reactivity of these types of molecules will give a better understanding of the chemistry that is occurring in the earth's stratosphere and troposphere. The method that will be used to accomplish this is gas-phase absorption using a rapid-scan midinfrared spectrometer.

This spectrometer is currently being constructed and will use a lead-salt diode laser operating in the midinfrared region around 2350 cm^{-1} . The rapid-scan technique that will be used allows for decreased sample consumption and shorter acquisition times along with a higher resolution to accurately assign the rovibrational spectrum of the molecule^[2]. In order to confirm that the instrument is operating properly, an experiment studying the $\text{CO}_2\text{-SO}_2$ weakly-bound complex will be done for comparison with previous results from the Jager group^[3]. The pulsed discharge nozzle that will act as the sample source has

been optimized through emission spectroscopy work. Free radical production through the nozzle will be confirmed by the recreation of a project studying the emission spectrum of the pentafluorobenzyl radical, which was previously studied by laser-induced fluorescence^[4]. The focus of the work presented here is preparatory towards building a rapid-scan midinfrared spectrometer at EIU and includes computer programming, visible emission spectroscopy, and microwave spectroscopy studies.

1.1.1 Introduction to Infrared Spectroscopy

Infrared spectroscopy is a common technique used to obtain information on the vibrational transitions of the molecule. The vibrational energy levels of a diatomic molecule are given by Equation (1.1) and depend on a net change in the dipole moment of the molecule within that vibration to be infrared active. In this equation, E_v represents the energy of a particular vibrational level, or $v' - v''$, with ν standing for the frequency, v the vibrational quantum number and h representing Planck's constant. A table of all the variables seen throughout this thesis is located in Appendix A. The more the dipole moment of a molecule changes with a particular vibration, the stronger the absorbance will be when the molecule reaches that vibrational excited state. Furthermore, the energy absorbed, or vibrational wavenumber, is related to the force constant, k , and reduced mass, μ , by Equation (1.2), which helps determine the strength of the bond holding the two atoms together^[5].

$$E_v = h\nu(v + \frac{1}{2}) \quad (1.1)$$

$$\nu = (1/2\pi) (k/\mu)^{1/2} \quad (1.2)$$

The vibration of a diatomic molecule is often represented by a “ball-and-spring” model, with the different energy levels being represented by a harmonic oscillator. A representation of the harmonic oscillator energy levels can be seen in Figure 1.1. When studying the infrared spectrum of a polyatomic molecule, the determinations quickly become more complicated. Vibrational spectra of polyatomic molecules contain both bending and stretching modes of vibration. The number of modes can be determined by using $3N - 5$ for linear molecules and $3N - 6$ for nonlinear molecules where N stands for the number of atoms present. The displacement of one atom will now mean the various stretching and bending of multiple “springs”, or bonds and angles, rapidly complicating Equations (1.1) and (1.2). Treatment of the harmonic oscillator approximation with quantum mechanics results in Equation (1.3) to represent a polyatomic molecule^[5].

$$G(v_i) = \omega_i(v_i + 1/2) \quad (1.3)$$

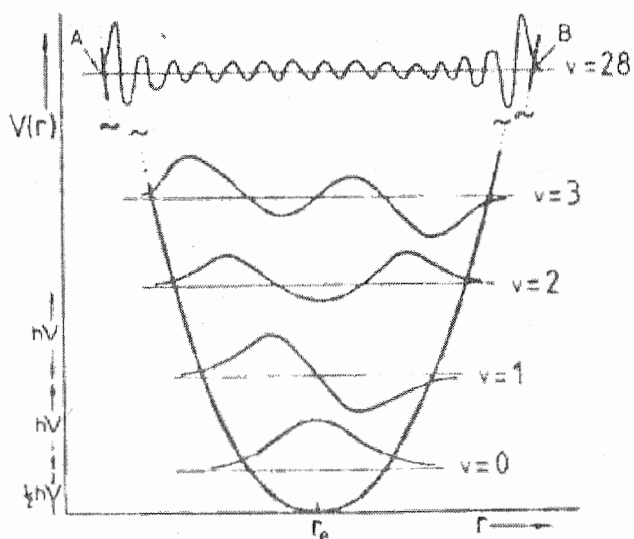


Figure 1.1^[5]: An energy plot for the harmonic oscillator model for vibration showing energy levels and wave functions. $V(r)$ in the plot represents the energy while r represents the displacement from the equilibrium distance, r_e , of the bond.

Equation (1.3) characterizes a system where all vibrations are non-degenerate. Within this calculation $G(v_i)$ stands for the vibrational term energy levels, with ω_i symbolizing the classical vibration wavenumber and v_i representing the vibrational quantum number. Despite the added complications, the system is still considered to undergo harmonic motion and can still be used to determine the strength of individual bonds within the molecule^[5].

Within each vibrational level is a series of rotational energy levels which show up as fine structure in the infrared spectrum. This spectrum consisting of vibrational bands along with stacks of rotational lines is commonly referred to as the rovibrational spectrum of a molecule. A set of these transitions with a vibrational transition can be seen in Figure 1.2. These rotational lines will form a P and R branch around the origin of the vibrational band. A P branch stands for a rotational series where $\Delta J = -1$ and the R branch representing $\Delta J = +1$, where J is the rotational quantum number. This will be discussed in more detail in

Chapter 2. One infrared band of HCN with corresponding branches can be seen in Figure 1.3. The rotational energy levels present will give data about the bond angles and distances of the molecule when put through a series of quantum mechanical calculations^[5]. This process will also be discussed further in Chapter 2.

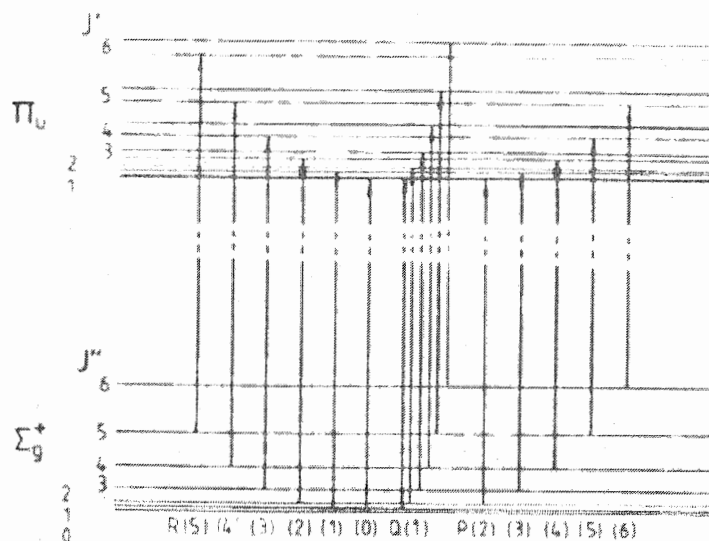


Figure 1.2^[5]: Rotational transitions within the $\Pi_u - \Sigma_g^+$ infrared vibrational transition of a linear polyatomic molecule.

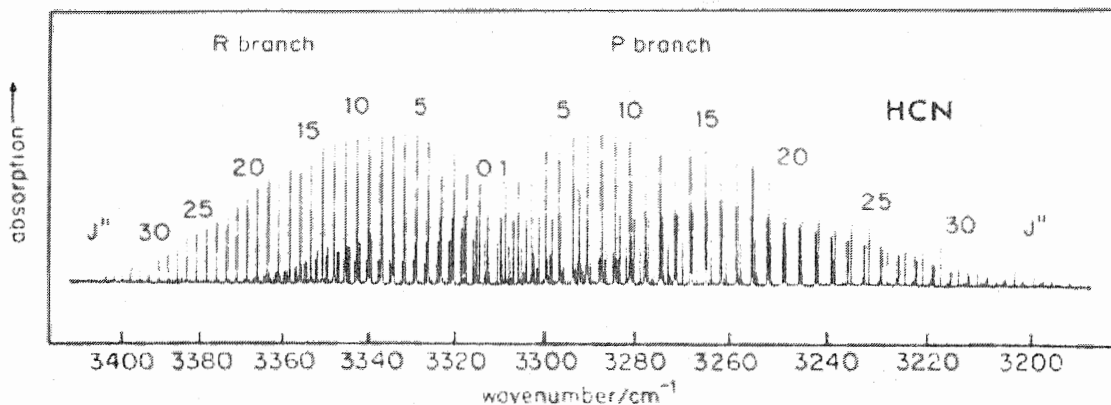


Figure 1.3^[5]: The $3^1_0, \Sigma^+ - \Sigma^+$ infrared band of HCN along with two overlapping bands which are much weaker. *P* and *R* branches such as the ones that are discussed above are displayed.

1.2 Background of infrared project

High resolution infrared spectroscopy has become an effective tool for studying intermolecular forces of weakly-bound complexes such as van der Waals interactions^[6]. The midinfrared spectrometer which will be constructed will use an instrumental set-up similar to the ones used by the Xu and Jager groups^{[7],[3]} as well as the McKellar group^[6] which were all used to study van der Waals interactions of weakly bound complexes. Recreation of the experiment studying CO₂-SO₂ done by the Jager group^[3] should confirm the presence of a properly working instrument and allow optimization of experimental conditions so that the lab can continue forward with experiments aimed at characterizing volatile organic compounds and hydrochlorofluorocarbons.

The original rapid scan technique used as the basis for all three previously built instruments was presented by De Piante, et. al^[2]. This set-up used a lead salt-diode laser, with the beam being sent into a monochromator for mode selection. The beam was then split and sent into a reference cell as well as an etalon, which was used for frequency calibration. The beam from the reference cell was focused and sent through a pulsed supersonic expansion from a pinhole-type nozzle. A typical acquisition cycle consisted of subtracting a spectrum taken when the nozzle was off, from a spectrum taken when the nozzle was on. Within the vacuum chamber a White cell was used to focus the infrared beam as well as extend the path length^[2]. A schematic of this instrument is seen in Figure 1.4. Two separate infrared detectors were used; one detecting the beam from the White cell and the reference cell, the other detecting the beam

from the etalon. Both detectors were attached to a digital oscilloscope connected to a computer for data analysis. Each laser mode was scanned at a rate of 0.2 cm^{-1}/ms over a $0.75 - 2.00 \text{ cm}^{-1}$ long mode^[2].

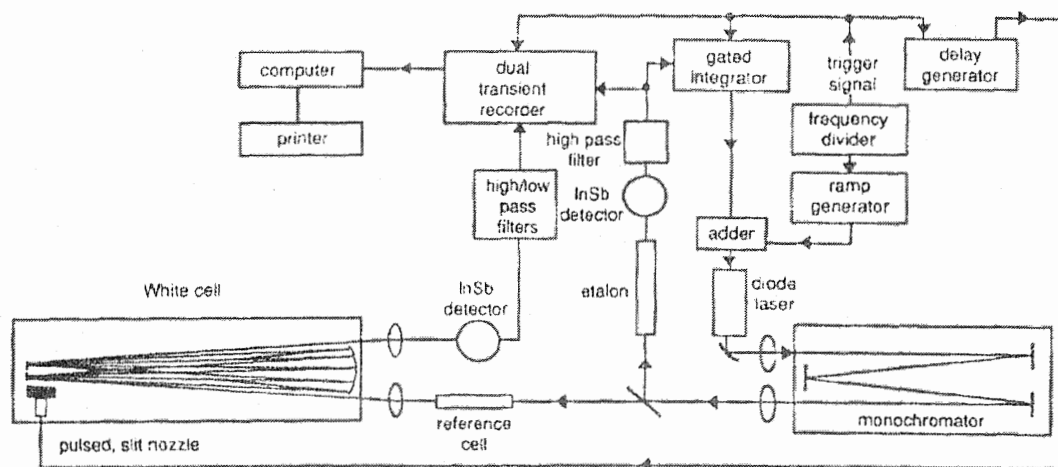


Figure 1.4^[2]: Schematic of the experimental set-up of the rapid-scan midinfrared spectrometer used by DePiante, et al.

The spectrometer built by the McKellar group employed these same principles while improving the instrumentation^[6]. The set-up for this instrument can be seen in Figure 1.5. The vacuum chamber used, for example, is able to sustain significantly higher backing pressures leading to a greater number of complexes that are able to be studied. Also, integration of a new optical system led to a significant improvement in the signal. The newer system proved to be more stable while increasing the absorption path. It also reduced the area that

the laser would probe within the cell and increased the number of passes through the cell from 80 to over 100^[6].

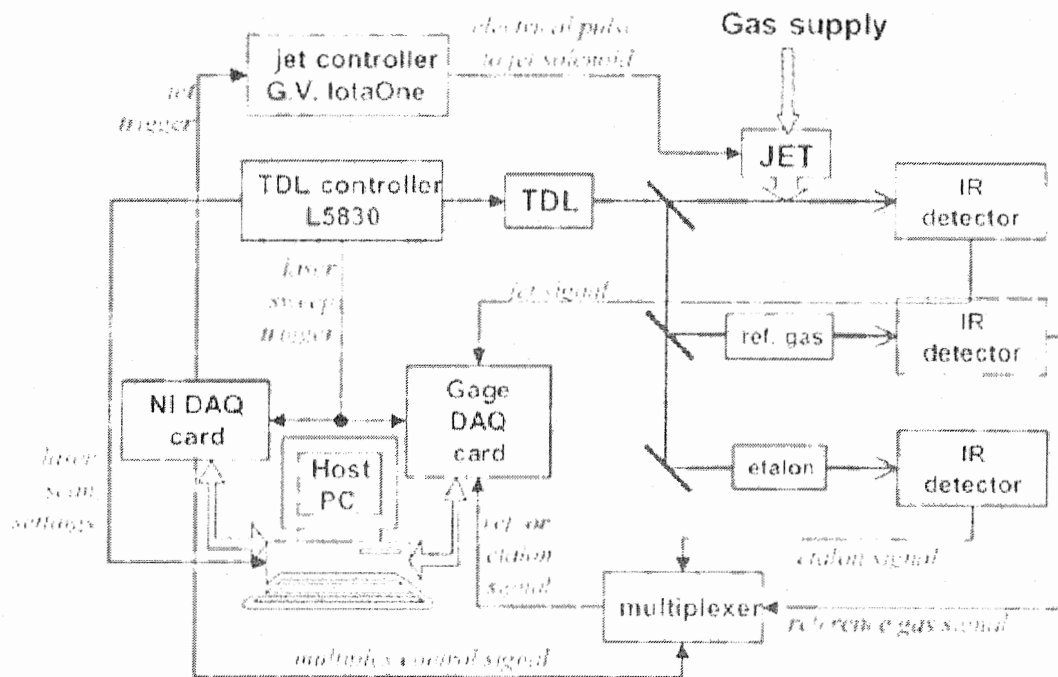


Figure 1.5^[6]: Schematic of the infrared spectrometer built by McKellar, et al.

Timing and data acquisition were also improved upon in the instrument built by McKellar, et. al. The laser could now be controlled by its own power supply allowing the controller to program the ramp settings and greatly simplifying data acquisition. The ramp is set to $0.5 \text{ cm}^{-1}/\text{ms}$ allowing for a quicker scan. Computer software controls data acquisition and synchronization of the instrument leading to greater reproducibility and larger data sets. The timing

sequence used for this instrument can be seen in Figure 1.6. Finally, three separate detectors are being used (Fig. 1.5), one for the jet spectrum, one for the beam as it passes through the reference gas and a third for the etalon spectrum. Using the same computer software the spectra for these three are produced and displayed simultaneously^[6].

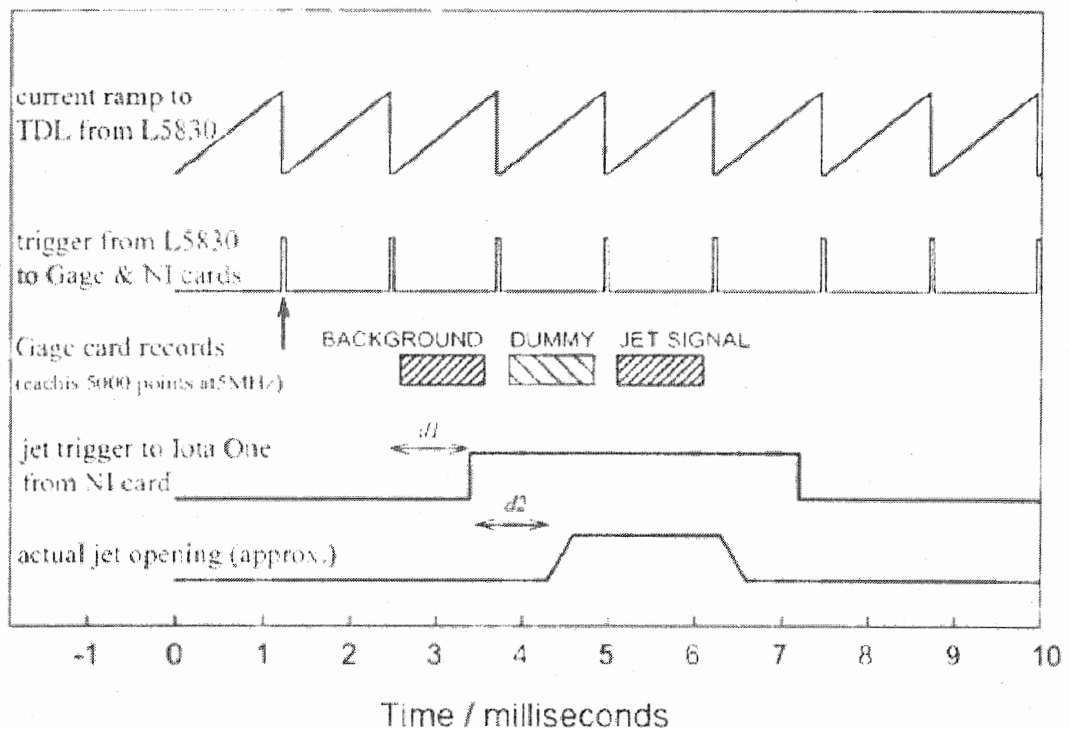


Figure 1.6^[6]: Timing sequence for the data acquisition cycle used with the instrument constructed by McKellar, et al. Data acquisition is controlled by the laser settings and triggered by the ramp peak shown by the top signal.

It is this, most recent, set-up that will be the basis for the future rapid-scan midinfrared spectrometer at Eastern Illinois University. This spectrometer is nearly complete with optical alignment in progress and all other parts of the spectrometer in place. Successful observation of CO₂-SO₂ will serve as confirmation of a working instrument. The lab can then move forward to further weakly-bound complex and free radical structure determinations of molecules common to atmospheric species. Once the instrument is constructed it will be used to study CO₂ complexes with volatile organic compounds (VOCs) and then complexes of CO₂ with hydrochlorofluorocarbons (HCFCs) and HCFC radicals which are a common objective of these experiments, due in large part to their importance in atmospheric modeling. Free radical species and HCFCs constitute some of the most important human-generated pollutants within our atmosphere and the formation of CO₂-HCFC complexes is thought to have an effect on the CO₂ IR absorbance frequencies involved in the greenhouse effect^[8].

1.3 Emission spectroscopy experiment

In order to study free radicals spectroscopically, an efficient method of forming them is needed. These molecules are highly reactive species due to the presence of an unpaired electron in their valence shell^[1]. One example of the type of reactions that these molecules undergo is shown in Figure 1.7. Their highly reactive nature is the cause of the difficulty in synthesizing these molecules for later analysis. When synthesis occurs, the concentration of the

species is very small and they are reactive enough that storage of the molecule is nearly impossible^[9]. Therefore, extreme environments are needed for free radical synthesis and once synthesis occurs they must be studied as soon as possible.

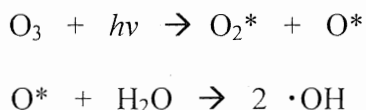


Figure 1.7^[1]: Reaction scheme for the destruction of ozone into the OH radical

Various methods have been used to solve this problem including direct absorption experiments using plasmas within hollow cathode geometries and magnetically enhanced negative glow discharges^[9]. The problem with these methods was that temperatures within the spectrometer were high for rovibrational spectroscopy, complicating the spectra. Also, these methods showed poor resolution due to Doppler broadening^[9]. Increasing in popularity is the method of studying these species using a pulsed discharge nozzle connected to a supersonic expansion chamber.

Using this technique, the pulsed discharge nozzle will create a high density of free radicals which will then be rovibrationally cooled in the expansion chamber. The temperature within the chamber will be low enough to avoid congestion of the spectrum as well as increasing resolution. A collision-free environment is also created which prevents immediate reactions of the radicals that are formed^[10]. An experimental set-up for this type of free-radical source will

be discussed in detail in Chapter 2. When the discharge created by the set-up is probed by an IR laser in a spectrometer similar to the one being constructed, valuable information can be obtained such as molecular structures, spin densities and radical concentrations^[10]. Obtaining this information, particularly on weakly bound and radical complexes is the ultimate goal of the high resolution spectroscopy group at EIU.

The operation of the discharge nozzle within a visible emission spectrometer is serving to optimize the conditions of the nozzle to produce the highest concentration of free radicals possible while also obtaining the emission spectra of these molecules. This can be done while other portions of the infrared spectrometer are being calibrated. The main advantage of optimizing the nozzle conditions within an emission spectrometer is simply the ability to view the discharge directly while conditions are being changed to observe characteristics such as color change, rise in intensity or a decrease in intensity.

Recently, a supersonic jet experiment was done by Lee, et al, which characterized the visible emission spectrum of the pentafluorobenzyl radical using laser induced fluorescence^[4]. The structure of this radical can be seen in Figure 1.8. Successful recreation of the pentafluorobenzyl spectrum should confirm free-radical production from the discharge nozzle present in the lab. This molecule was chosen by the Lee group because of the importance of benzyl radicals in aromatic compound reactions^[4]. The common occurrence of aromatic compounds being emitted into the atmosphere makes the study of their radical species very important to atmospheric chemistry. Although the

pentafluorobenzyl radical itself is unlikely in the atmosphere, the confirmation of its production will allow the group to move forward with its own experiments characterizing radical species of HCFCs or aromatic compounds that are more likely in the atmosphere, such as some volatile organic compounds. Our initial discharge studies will focus on toluene and xylene, two widely available VOCs which are closely related to pentafluorotoluene, and which would be expected to give emission spectra similar to that expected for the pentafluorobenzyl radical.

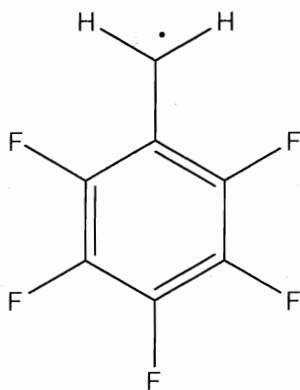


Figure 1.8: The molecular structure of the pentafluorobenzyl radical

1.4 Microwave studies

The goal of the spectroscopy group at EIU with respect to the emission spectrometer was to form the pentafluorobenzyl radical with the discharge nozzle. It would be necessary, therefore, to obtain information on its precursor 2,3,4,5,6-pentafluorotoluene, or PFTOL. In order to fully understand the spectra

of free radical species, the structure and reactivity of their precursors must be fully understood and from searching the literature for information on the precursor, it was found that no microwave work had been done on pentafluorotoluene. Fourier-transform microwave spectroscopy, or FTMW spectroscopy, is an effective way of determining the structure of a compound in its gaseous state^[5]. This method uses the rotational spectrum of the molecule to determine bond angles and distances of that species or weakly bound complex. A project was started in order to determine the structure and reactivity of pentafluorotoluene. A full understanding of the structure of the radical precursor will help determine the structure of the radical after its creation.

The microwave spectroscopy study of pentafluorotoluene resulted in some interesting observations which will be discussed in detail in Chapter 4. To further expand on this project, it was decided to also study the rotational spectrum of 1-chloro-2,3,4,5,6-pentafluorobenzene, or CPFB. The structures of both molecules that were studied using microwave spectroscopy can be seen in Figure 1.9. The substitution of a chlorine atom for the methyl group should help to determine the internal rotation effects present in pentafluorotoluene.

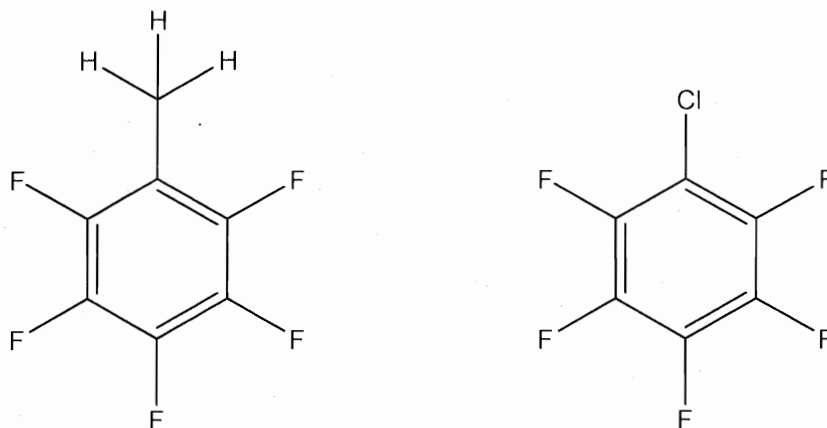


Figure 1.9: The molecular structure of 2,3,4,5,6-pentafluorotoluene (left) and of 1-chloro-2,3,4,5,6-pentafluorobenzene (right)

The following chapters will discuss the preparations made for constructing a rapid-scan midinfrared spectrometer. Experimental details of the discharge and microwave experiments are located in Chapter 2. Chapter 3 will include optimization of the pulsed discharge nozzle constructed at Eastern Illinois University using visible emission spectroscopy work to study toluene and xylene, as well as computer programming aimed at the overall control and synchronization of both the emission and infrared spectrometers. Microwave studies were then performed in order to fully understand the precursor molecules of the free radical species which will be synthesized in the pulsed discharge nozzle. These microwave experiments are described in Chapters 4 and 5. Finally, overall conclusions that were drawn from the series of experiments are located in Chapter 6.

References: Chapter 1

- [¹]Duffy, S.J.; vanLoon, G.W. In *Environmental Chemistry: A Global Perspective*. Oxford University Press: New York, NY 2005.
- [²]DePiante, A.; Campbell, E.J.; Buelow, S.J. *Rev. Sci. Instrum.* **1989**, *60*(5), 858 – 862.
- [³]Jager, W.; Osthoff, H.D.; Walls, J.; van Wijngaarden, W.A. *Rev. Sci. Instrum.* **2004**, *75*(1), 46 – 53.
- [⁴]Lee, S.K.; Baek, D.Y. *Chem. Phys. Lett.* **1999**, *311*, 36 – 40.
- [⁵]Hollas, M.J. In *Modern Spectroscopy*, 3rd ed; John Wiley & Sons: New York, NY 1996.
- [⁶]Brookes, M.D.; Xia, C.; Tang, J.; Anstey, J.A.; Fulsom, B.G.; Yong, K.A.; King, J.M.; McKellar, A.R.W. *Spectro. Act. A.* **2004**, *60*, 3235 – 3242.
- [⁷]Xu, Y.; Tam, W.S.; Su, Z. *J. Chem. Phys.* **2006**, *124*, 024311(1-9).
- [⁸]Chrysos, M.; Kouzov, A.P.; Egorova, N.I.; Ratchet, F. *Phys. Rev. Lett.* **2008**, *100*, 133007.
- [⁹]Motylewski, T.; Linnartz, H. *Rev. Sci. Instrum.* **1999**, *70*(2), 1305 – 1312.
- [¹⁰]Davis, S.; Anderson, D.T.; Duxbury, G.; Nesbitt, D.J. *J. Chem. Phys.* **1997**, *107*(15), 661 – 6675.

Chapter 2: Experimental

2.1 Pulsed discharge nozzle emission spectroscopy

As stated in the previous chapter, a pulsed discharge nozzle attached to a supersonic expansion chamber has become a very powerful method for the synthesis of free radicals. These types of nozzles have been used in the past to study anions, cations, aromatic hydrocarbon species as well as organic molecules^[1]. These types of compounds, however, can often be synthesized elsewhere before characterization. The appeal of a discharge source for the synthesis of free radicals comes from the extreme environment that using a high powered electrical discharge creates, which can generate the radical compound within the nozzle leading to immediate characterization within the chamber^[2]. The supersonic expansion will immediately cool the radical species avoiding side reactions of the compound within the cell. This set-up avoids the congested spectra and Doppler broadening seen using previous methods due to the high rovibrational temperatures present in those methods^[3]. Furthermore, using a pulsed discharge rather than a continuous nozzle will further lower the rovibrational temperatures and improve radical density^[4].

Two separate methods are employed when forming a target compound. The one being used with the current discharge nozzle and that is most common to free radical experiments is to form the compound from a precursor molecule. This precursor molecule has some functional group that it can lose to form the desired radical species. A second option is to rely on the chemistry that is taking

place within the discharge to form a target compound^[1]. An example of this is the study on discharge aromatic products from 1,3-butadiene done by Newby, et al^[5]. This discharge source can be used in different experimental techniques such as laser-induced fluorescence, time-of-flight mass spectrometry and cavity ring down spectroscopy^[1].

The pulsed discharge nozzle constructed at Eastern Illinois University is currently being used as the source of a visible emission spectrometer. This is being done simply to optimize the pulsed discharge nozzle conditions as described in Chapter 1. As stated previously, recreation of an experiment which focused on the pentafluorobenzyl radical emission spectrum will confirm radical production^[6]. The main advantage in using visible emission spectroscopy when optimizing the nozzle is the ability to view the discharge within the chamber as the settings are being changed. The effects of certain conditions, such as variation of the applied voltage, on the discharge will be seen immediately before full characterization.

Emission spectroscopy can be used to determine vibronic or electronic excited states. In the case of the pentafluorobenzyl radical, it is the vibronic emission spectrum that will be recreated. The vibronic spectrum will include a series of vibrational transitions for each electronic transition present. As the molecule is being excited by the discharge nozzle, it is cooled by the expansion into the vacuum chamber. This causes the molecule to relax back to the ground state, at which time it emits light at a series of wavelengths. The wavelengths of light that are emitted correspond to electronic and vibrational transitions.

Vibronic transitions appear as numerous smaller lines within an electronic spectrum. An example of the transitions that can occur is shown in Figure 2.1. This figure shows how multiple vibrational transitions can occur within one electronic transition^[7].

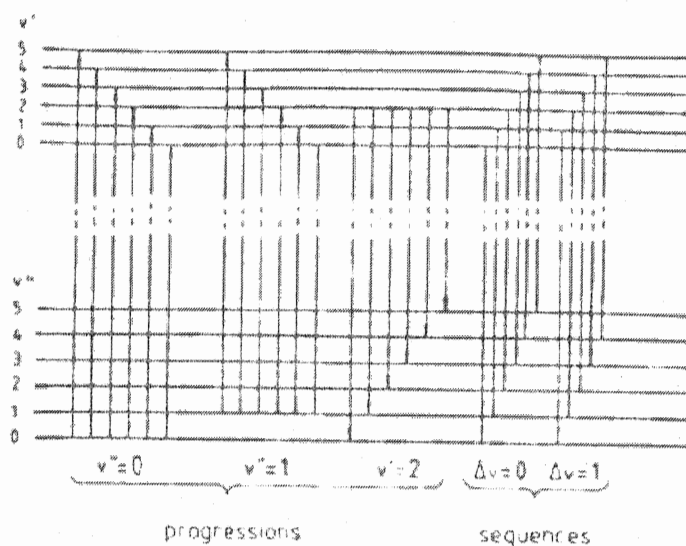


Figure 2.1^[7]: Vibrational progressions within the electronic spectrum of a diatomic molecule

In order to control the visible emission spectrometer that was being used, a series of computer programs was written using LabVIEW software^[8]. LabVIEW 7.1 is graphical programming software released by National Instruments. Made mainly for the scientific community, it focuses on data collection and instrument control. Text-based code is represented in the form of icons, which are then placed on a block diagram and linked together through a series of wires. A list of the different controls and functions used in LabVIEW programs throughout this

thesis can be seen in Appendix B. LabVIEW simplifies the programming significantly for users who do not have previous computer programming experience. The code is controlled by a user interface referred to as the front panel which utilizes specific control and indicator functions to run the program. The final compilation of this code creates a file called a VI, short for Virtual Instrumentation. The main benefit of this way of programming is that errors in a program are shown graphically before it is ever run, unlike text-based programs^[9]. LabVIEW was used in order to write a series of programs aimed at controlling the emission spectrometer as well as performing data analysis. Programs were needed that control the nozzle, acquire data from the PMT, scan the monochromator and one that runs all three programs simultaneously. These are discussed in more detail in Chapter 3. Data analysis programs including one to analyze the results of a recently constructed broadband microwave spectrometer were also developed in addition to the instrument control VIs and are discussed in Appendix C.

2.2 Microwave spectroscopy

Creation of the pentafluorobenzyl radical would be done through the pulsed discharge nozzle previously mentioned, using pentafluorotoluene as a precursor molecule. It is believed that placing pentafluorotoluene directly into the discharge nozzle will cause a dissociation of an H atom to form the pentafluorobenzyl radical^[6]. Since pentafluorotoluene would be used as the

radical precursor, it was necessary to gather information on the structure and reactivity of the molecule. A series of microwave spectroscopy studies was then done studying PFTOL followed by chloropentafluorobenzene, or CPFb for comparison.

Microwave spectroscopy is a powerful tool for studying the rotational spectrum of a molecule in the gas phase. The rotational spectrum of a particular molecule is dependent on the magnitude of its moments of inertia around one of the three principal axes. The total moment of inertia of a molecule, I , can be determined by Equation (2.1). In this equation, m represents the mass of a particular atom and r represents that atom's distance from the axis. The i index seen in the equations stands for a particular principal axis, a , b or c . The principal axes of a molecule are determined in such a way so that the maximum moment of inertia will correspond to the c axis leading to Equation (2.2). Finally, in order for the microwave spectrum to be measured, the molecule must have a permanent dipole moment^[7].

$$I_i = \sum m_i r_i^2 \quad (2.1)$$

$$I_c \geq I_b \geq I_a \quad (2.2)$$

The spectrum produced by microwave spectroscopy can then be used to determine the moments of inertia of the molecule. Each line seen in the spectrum coincides to a transition between rotational energy levels represented by the quantum number J which stands for the total rotational angular

momentum. A particular energy level for a diatomic molecule is related to J by Equation (2.3). The frequency required for a particular transition is given by Equation (2.4). Involved in the determination of J are a series of rotational constants, A , B and C , which correspond to the principal axes a , b and c . They are related to the moment of inertia about that axis by Equation (2.5)^[7]. The rotational constant located in Equation (2.5) is equivalent to the constant in Equation 2.4 and the term in square brackets in Equation (2.3).

$$E_r = [h^2 / (8\pi^2 I)] J(J + 1) \quad (2.3)$$

$$\nu = 2B (J + 1) \quad (2.4)$$

$$B = h^2 / 8\pi^2 I_b \quad (2.5)$$

After determination of the moments of inertia of a molecule, the molecular geometry and structure can be determined. Due to the relation of the moment of inertia to the distance of the atoms from the axis given by Equation (2.1), the bond angles and distances of the molecule can then be calculated^[7]. The types of overall geometry of a molecule include an asymmetric rotor, prolate symmetric rotor or oblate symmetric rotor. For a pure symmetric rotor, two moments of inertia are equivalent. For a prolate symmetric rotor, I_c and I_b are equivalent indicating an elongated molecule, such as methyl iodide shown in Figure 2.2. If I_b and I_a are equivalent, this indicates the oblate rotor of a "pancake"-shaped molecule, of which benzene is an example, shown in Figure 2.3. The differences in energy levels of these two types of symmetric rotor can be seen in Figure 2.4.

These originate from Equation (2.6) which shows the determination of energy levels for a prolate symmetric rotor^[7].

$$F(J,K) = BJ(J + 1) + (A - B)K^2 \quad (2.6)$$

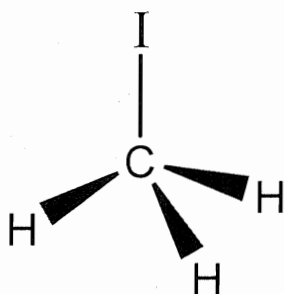


Figure 2.2: Methyl Iodide; an example of a prolate rotor

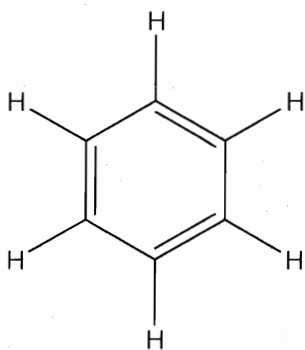


Figure 2.3: Benzene; an example of an oblate rotor

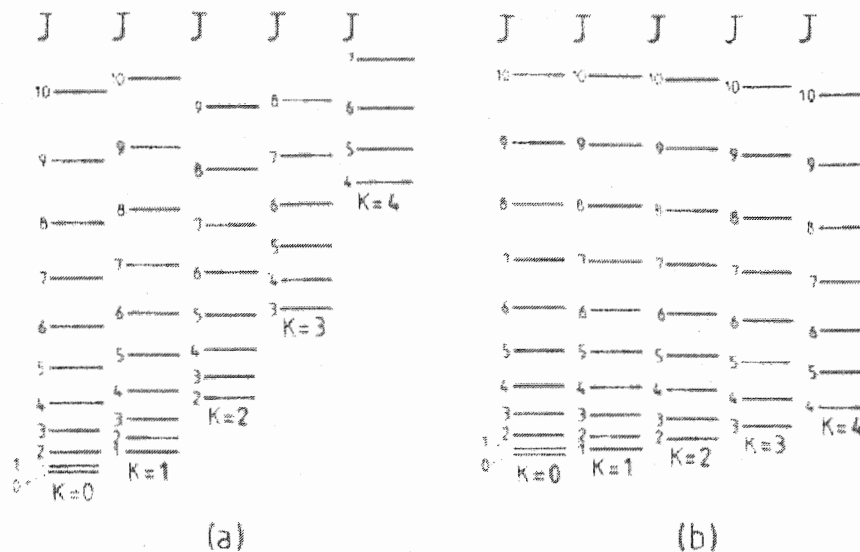


Figure 2.4^[7]: Rotational energy levels for a prolate rotor (a) and an oblate rotor (b)

Although the molecules discussed in the current work are asymmetric rotors, they can be analyzed by adapting the basic theory described above, with the main difference being the addition of a second K quantum number and multiple centrifugal distortion constants. This K quantum number, seen in Figure 2.4 and Equation (2.6), is a projection of the rotational angular momentum (J) along the corresponding axis. Of final note, the differences in the spacing of the transitions as J increases are due to the centrifugal distortion of a molecule represented by the constant D . This type of distortion occurs from the centrifugal force exerted on the molecule as it is rotating.

Assignment of the rotational spectrum of a molecule requires several steps which includes several computer programs. The first step in this procedure involves *ab initio* calculations in order to predict the geometry of the molecule as well as the rotational constants. These calculations are performed using

Gaussian 03^[10] at the MP2 level with a 6-311++G(2d,2p) basis set. Once this has been done the SPCAT^[11] program is used to predict the rotational spectrum based off of the rotational constants obtained from *ab initio* results. Transitions are then chosen and searched for within the microwave spectrum based on the frequency given from SPCAT. Once four to five transitions have been measured, a preliminary fit is performed using the SPFIT^[11] program in order to determine experimental rotational constants. This program uses a Watson-type Hamiltonian to least-squares fit the spectroscopic constants to the observed transition frequencies^[12]. These constants are then put back into SPCAT, which uses the same Hamiltonian in a predictive sense, and the process continues until all transitions have been measured and the experimental spectroscopic constants have been determined with the desired level of precision according to the instrumental error of the spectrometer. Once this has been done further determinations, such as structure and dipole moment, can be made. The results of these determinations for PFTOL and CPF B will be discussed in Chapters 4 and 5.

2.3 Experimental details

Before the microwave projects were started, a series of discharge experiments were done aimed at optimizing nozzle conditions within a visible emission spectrometer. A basic block diagram of the nozzle can be seen in Figure 2.5 and the emission spectrometer in Figure 2.6. The discharge nozzle is

a pinhole-type pulsed discharge nozzle with two stainless-steel electrodes within the body of the nozzle. A (+/-) 950 V electrical discharge is placed on the two electrodes with the positive electrode positioned towards the body of the nozzle and the negative electrode positioned towards the opening. The nozzle was pulsed at a rate of 10 Hz. A pulse length of 700 μ s was used during the discharge experiments. During optimization of the nozzle, conditions such as voltage, pulse length, backing pressures and electrode configuration were varied to determine when the brightest and most reliable discharge occurred.

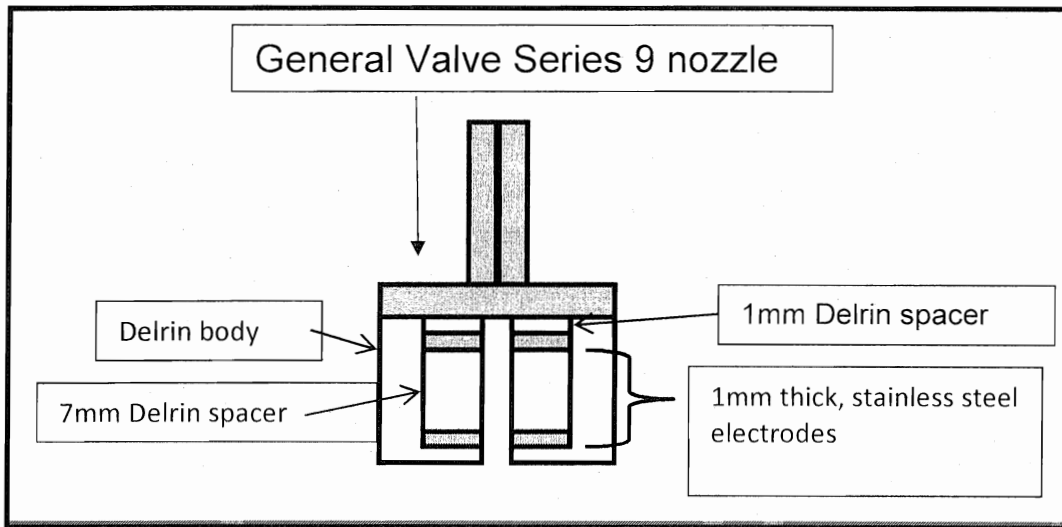


Figure 2.5: Block diagram of the pulsed discharge nozzle, showing the electrodes used as well as their orientation within the nozzle body.

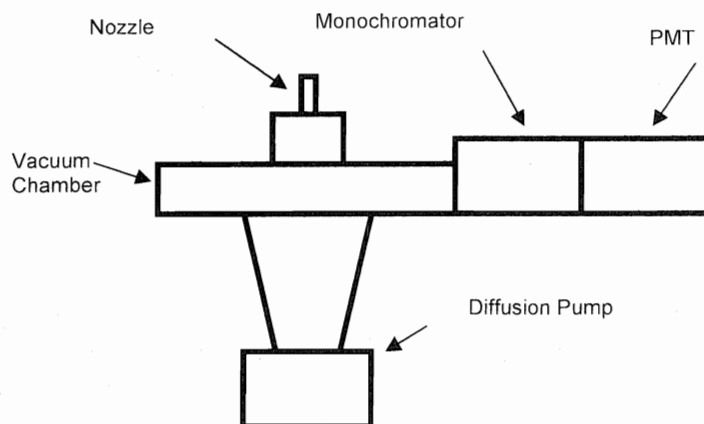


Figure 2.6: Block diagram of the visible emission spectrometer at EIU. The nozzle acts as the sample source while the monochromator selects the appropriate wavelength to be detected by the PMT.

The discharge emission studies used liquid samples obtained from Aldrich of the precursor compounds, toluene and xylene. Xylene was studied using a mixture of *ortho*-, *meta*-, and *para*-xylene. Around 100 μL of sample was placed with a glass pipet into a metal U-tube. Teflon tubing then led from this U-tube to the discharge nozzle with argon being used as the carrier gas flowing over the sample at around 20 psi. General scans of the emission spectrum were recorded from 300 – 800 nm in 100 nm segments. Each 100 nm interval used 1 nm monochromator steps. Focus was then placed on areas where multiple emission bands were detected by rescanning a 100 nm region using 10 nm segments with 0.1 nm monochromator steps to improve resolution. After initial testing, the monochromator also was set with a slit width of 5 μm . Five thousand

PMT averages were obtained per monochromator step. The resulting emission spectra can be seen in Chapter 3.

Three separate instruments were used during the microwave studies of both PFTOL and CPF. Pentafluorotoluene was studied using the Balle-Flygare type Fourier-transform microwave, or FTMW, spectrometer located at Eastern Illinois University^[13] (Figure 2.7) as well as a chirped-pulse broadband FTMW, or CP-FTMW, spectrometer located at the University of North Texas^[14].

Chloropentafluorobenzene was studied using the CP-FTMW located at the University of Virginia^[15].

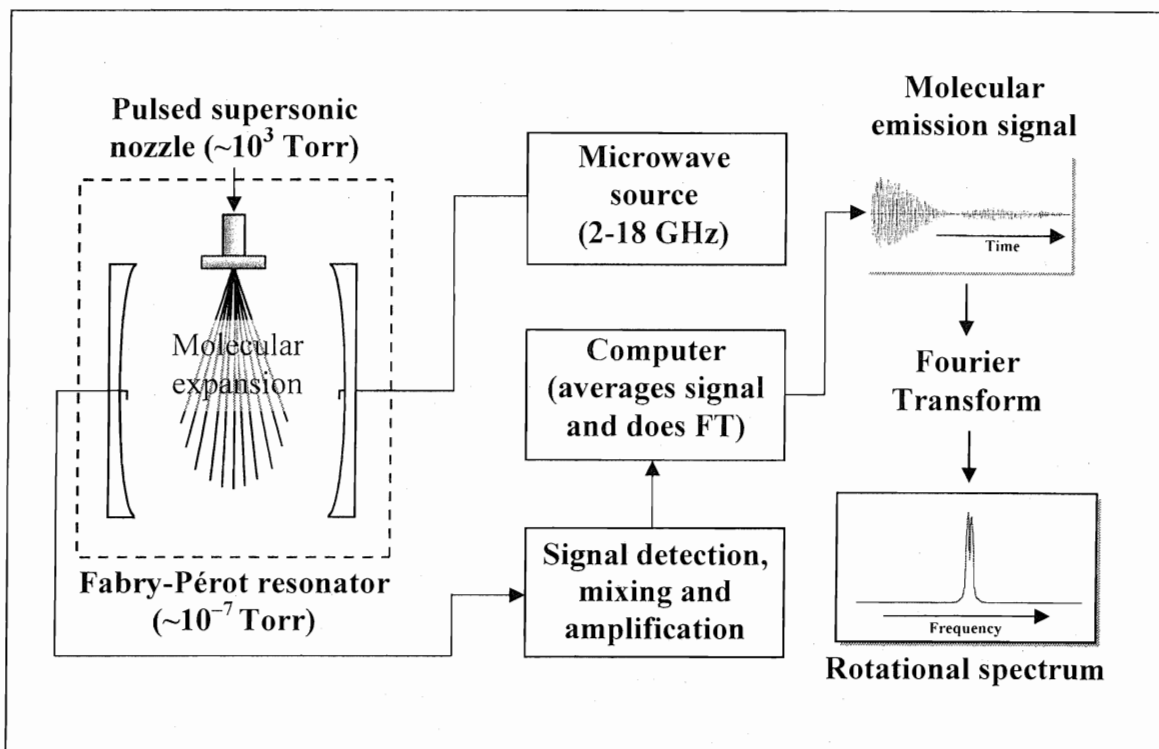


Figure 2.7^[13]: Schematic of the Balle-Flygare type FTMW spectrometer located at EIU, showing the relative microwave source, supersonic expansion chamber and detector locations.

The basic theory behind an FTMW spectrometer relies on every step taken by the instrument being well synchronized. The instrument begins by introduction of a gaseous sample through a pulsed nozzle into the Fabry-Perot cavity formed by two large mirrors. A band of microwave radiation is then pulsed from the generator (microwave source in Figure 2.7) spanning around 1 MHz with a chosen center frequency. If the molecule contains a transition with a frequency within the given range, the radiation will excite the molecule to an excited rotational state. After the microwave pulse ends, the sample then decays back down to the ground state, emitting radiation as it does. This decay is detected in the time domain and a Fourier-transform is used to change the spectrum into the frequency domain^[16].

Chirped-pulse broadband FTMW spectroscopy is a recent development used to expand on the Balle-Flygare type FTMW instrument. A basic schematic of the instrument located at the University of North Texas (UNT) is shown in Figure 2.8 as well as the one located at the University of Virginia (UVa) in Figure 2.9. The theory behind this type of spectrometer was developed by the Pate group^[15]. CP-FTMW uses an arbitrary waveform generator to output a large frequency range and mixes this signal with a center frequency from the microwave source. This creates a linear frequency sweep which is pulsed into the spectrometer cavity and takes around 1 μ s to complete. A much broader spectrum can be taken in a single step than is capable with the Balle-Flygare FTMW. The CP-FTMW at UVa, for example, can measure an 11 GHz spectrum in one acquisition^[15]. The frequency range that can be measured at one time is

limited only by the size of the waveform generator and oscilloscope which detects the signal. This significantly decreases acquisition time as well as sample consumption^[15]. These advantages are at the expense, however, of resolution of the overall spectrum, which is lowered in the CP-FTMW by around a factor of 10.

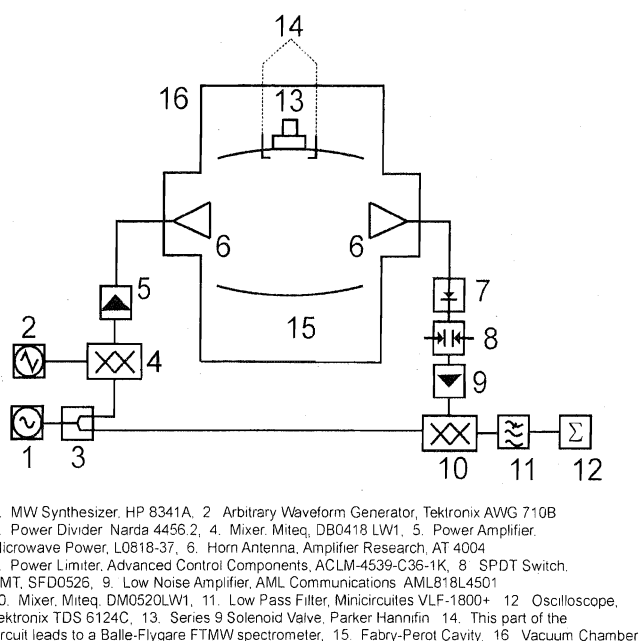


Figure 2.8^[14]: Schematic of the CP-FTMW located at the University of North Texas. In this spectrometer, the microwave frequency range is created by 1 and 2, sent into the expansion chamber indicated by 16 and finally detected by the oscilloscope indicated by number 12.

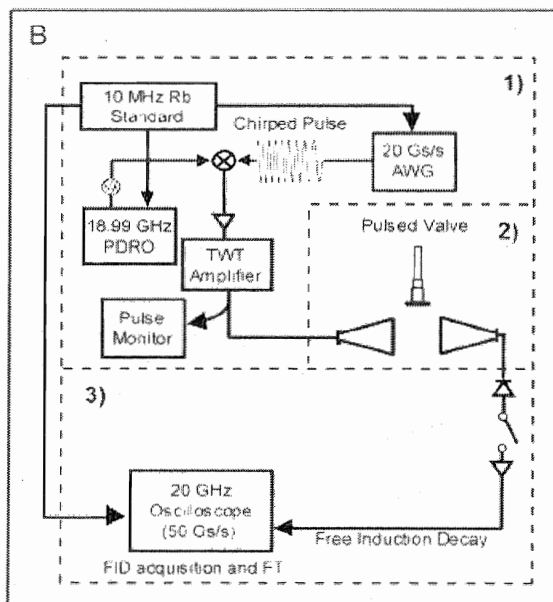


Figure 2.9^[15]: Schematic of the CP-FTMW located at the University of Virginia. The microwave pulse generation is contained in the box labeled 1), with excitation taking place within the box labeled 2), and finally detected by the scope within 3). This spectrometer contains a larger waveform generator and oscilloscope than the instrument in Figure 2.8 resulting in a broader frequency range used.

For the study of PFTOL using both the EIU FTMW and the UNT CP-FTMW, liquid sample (Aldrich) was placed in Teflon tubing connected to the nozzle. A He/Ne carrier gas was flowed over the sample at around 1.5 to 2 atm. When using the FTMW at EIU, the rotational transitions were measured by searching 300 kHz frequency steps using 500 – 2000 nozzle fires per acquisition with an axial nozzle configuration. Measuring pentafluorotoluene at UNT measured an 8 – 18 GHz range in four 3 GHz steps with 30,000 nozzle fires per step. CPFEB used a sampling technique similar to PFTOL with a He/Ne carrier gas flowed over a liquid sample. Two separate spectra were obtained for this molecule at UVa. The first was measured spanning an 11 GHz range in a single

step, using 320,000 sample averages. The second spectrum attempted to improve signal to noise ratio by employing a bandpass filter. The microwave chirp was lowered to 6.8 – 9 GHz and the filter was then added to rid the signal of noise that would leak through at other frequencies. The signal was also improved in this second spectrum by using 8.4 million sample averages with 50 averages per nozzle fire rather than 10, used previously. The results of these microwave studies can be seen in Chapters 4 and 5.

References: Chapter 2

- [1] Stearns, J. The fate of electronically excited molecules: Photochemical reactivity and excitonic interaction. Ph.D. Thesis, Purdue University, West Lafayette, IN, 2005.
- [2] Davis, S.; Anderson, D.T.; Duxbury, G.; Nesbitt, D.J. *J. Chem. Phys.* **1997**, *107*(15), 5661 – 5675.
- [3] Motylewski, T.; Linnartz, H. *Rev. Sci. Instrum.* **1999**, *70*(2), 1305 – 1312.
- [4] Davis, S. High resolution infrared spectroscopy of slit-jet cooled transient molecules: from van der waals clusters, to hydrogen bound dimers, to small organic radicals. Ph.D. Thesis, University of Colorado, Boulder, CO, 2000.
- [5] Newby, J.J.; Stearns, J.A.; Liu, C.; Zwier, T.S. *J. Phys. Chem. A.*, **2007**, *111*(43), 10915 – 10927.
- [6] Lee, S.K.; Baek, D.Y. *Chem. Phys. Lett.* **1999**, *311*, 36 – 40.
- [7] Hollas, M.J. In *Modern Spectroscopy 3rd ed.* John Wiley & Sons: New York, NY 1996.
- [8] LabView 7.1, National Instruments Inc., 2004.
- [9] Beyon, J. In *LabVIEW; Programming, Data Acquisition and Analysis.* Prentice Hall PTR: New Jersey 2001.
- [10] Gaussian 03, Revision C.02, M. J. Frisch, G. W. Trucks, H. B. Schlegel, G. E. Scuseria, M. A. Robb, J. R. Cheeseman, J. A. Montgomery, Jr., T. Vreven, K. N. Kudin, J. C. Burant, J. M. Millam, S. S. Iyengar, J. Tomasi, V. Barone, B. Mennucci, M. Cossi, G. Scalmani, N. Rega, G. A. Petersson, H. Nakatsuji, M. Hada, M. Ehara, K. Toyota, R. Fukuda, J. Hasegawa, M. Ishida, T. Nakajima, Y. Honda, O. Kitao, H. Nakai, M. Klene, X. Li, J. E. Knox, H. P. Hratchian, J. B. Cross, V. Bakken, C. Adamo, J. Jaramillo, R. Gomperts, R. E. Stratmann, O. Yazyev, A. J. Austin, R. Cammi, C. Pomelli, J. W. Ochterski, P. Y. Ayala, K. Morokuma, G. A. Voth, P. Salvador, J. J. Dannenberg, V. G. Zakrzewski, S. Dapprich, A. D. Daniels, M. C. Strain, O. Farkas, D. K. Malick, A. D. Rabuck, K. Raghavachari, J. B. Foresman, J. V. Ortiz, Q. Cui, A. G. Baboul, S. Clifford, J. Cioslowski, B. B. Stefanov, G. Liu, A. Liashenko, P. Piskorz, I. Komaromi, R. L. Martin, D. J. Fox, T. Keith, M. A. Al-Laham, C. Y. Peng, A. Nanayakkara, M. Challacombe, P. M. W. Gill, B. Johnson, W. Chen, M. W. Wong, C. Gonzalez, and J. A. Pople, Gaussian, Inc., Wallingford CT, 2004.

- [11] Pickett, H. M. *J. Mol. Spectrosc.* **1991**, *148*, 371.
- [12] Watson, J.K.G. *Vib. Spectra Struct.* **1977**, *6*, 1.
- [13] Grabow, J.-U. Ph.D. Thesis, University of Kiel, 1992
- [14] Cooke, S. University of North Texas. Private Communication. 2009.
- [15] Brown, G. G.; Dian, B. C.; Douglass, K. O.; Geyer, S. M.; Shipman, S. T.; Pate, B. H. *Rev. Sci. Instrum.* **2008**, *79*, 053103.
- [16] Legon, A.C. *Ann. Rev. Phys. Chem.* **1983**, *34*, 275 – 300.

Chapter 3: Emission Spectroscopy Studies of Volatile Organic Compound Derivatives

3.1 Introduction

The visible emission spectroscopy experiment was conceived, as discussed previously, in order to optimize the conditions of the pulsed discharge nozzle (PDN), and confirm the creation of free radicals. This would be accomplished by creation of the pentafluorobenzyl radical emission spectrum observed in an experiment which has previously been published^[1]. That study used a discharge set-up similar to that located at EIU. A pin-hole type nozzle is used with a high-power electrical discharge. The nozzle is attached to a supersonic expansion chamber and pumping system, with the spectrometer being set up to measure vibronic emission spectra as described in Chapter 2. Before recreation of the pentafluorobenzyl radical, a series of emission studies was done on toluene and xylene. These two compounds were believed to be similar enough to the pentafluorotoluene molecule that they would give a good representation of the conditions needed to recreate the target experiment. The conditions needed to create the benzyl radical, for example, should be similar to the conditions needed to create the pentafluorobenzyl radical. This was also done for preliminary indication of the type of products that would be created from putting similar molecules through the PDN, and identification of these products was a primary focus of the toluene and xylene studies.

This chapter will first explain the computer programming that was done in order to make the discharge experiments possible as well as early testing done on these programs. This programming was done using the scientific programming software LabVIEW^[2]. Then, the discharge experiment on I₂ will be described which was done to provide early confirmation of a properly working instrument. Finally, it will discuss the series of discharge emission studies that were done on toluene and xylene in order to optimize the PDN settings and observe the types of products that were forming from the discharge.

The nozzle that was constructed at EIU was based off of the pin-hole type nozzle of the Zwier group^[3]. The set-up of the nozzle that is currently being used can be seen in Chapter 2. While this is similar to the PDN used by the Zwier group some differences were made in order to obtain the most intense discharge possible. The nozzle built by the Zwier group used a (+/-)300 - 500 V electrical discharge placed on the two electrodes. This creates an electrical arc between the electrodes, which are separated by a 1 mm spacer. A diagram of the nozzle used by the Zwier group can be seen in Figure 3.1^[4]. Similarities between the previous nozzle and the one located at EIU (Figure 2.5) include the use of insulators within the body of the nozzle as well as the two electrode design. In the Zwier group nozzle, the electrode closest to the body serves as the anode, containing the negative voltage with the electrode located at the opening of the nozzle serving as the cathode. In contrast, the EIU nozzle uses the opposite polarity with the positive charge nearest the nozzle body. While this may seem counterintuitive to the production of free radicals, opposite orientation of the

electrodes was found to produce a very unreliable discharge. In addition, unlike the Zwier group nozzle, the PDN at EIU uses a (+/-) 950 V discharge with a 7 mm spacer between both electrodes.

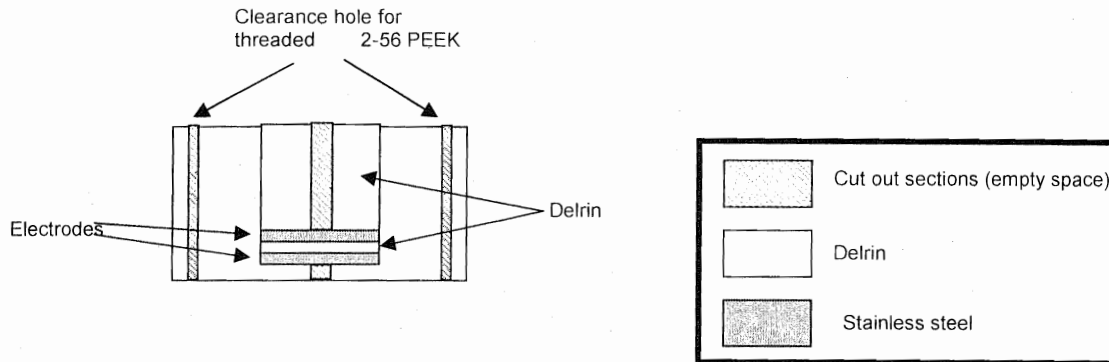


Figure 3.1^[4]: Diagram of the pulsed discharge nozzle used by the Zwier group, showing similarity to the EIU nozzle (Figure 2.5).

Justification for the disparities between the two nozzle designs came from adjustment of the settings to determine what would give the most intense discharge, judging by how bright the glow was within the chamber. The electrical potential between the electrodes was adjusted in 50 V increments from 500 – 950 V. As the voltage decreased, so did the visible intensity of the discharge. Likewise, the nozzle was run using a spacing of 1 mm between the electrodes, but when this was done, discharge seemed to occur inconsistently. When a discharge did occur, a large amount of sparking was seen within the chamber. This occurred when arcing took place from the nozzle to the walls of the chamber. Finally, the most efficient rate at which to run the nozzle was determined. The PDN was run at varying rates from 1 – 10 Hz, with the

discharge becoming more unstable the slower the rate. For the discharge experiments, a rate of 10 Hz was used as this was found to produce a steady discharge and intense signal.

3.2 Software development

Before emission spectra could be recorded, computer programs were needed to run the instrument as a whole as well as its individual parts. This was done using LabVIEW software^[2]. As stated in Chapter 2, LabVIEW software is a computer programming software for the scientific community. It simplifies computer programming by representing normal text-based code through a series of icons. The programs written using this software are referred to as VIs, or virtual instruments^[5]. The types of VIs that were written using this program include software that controls the emission spectrometer as well as data analysis programs that can be seen in Appendix C.

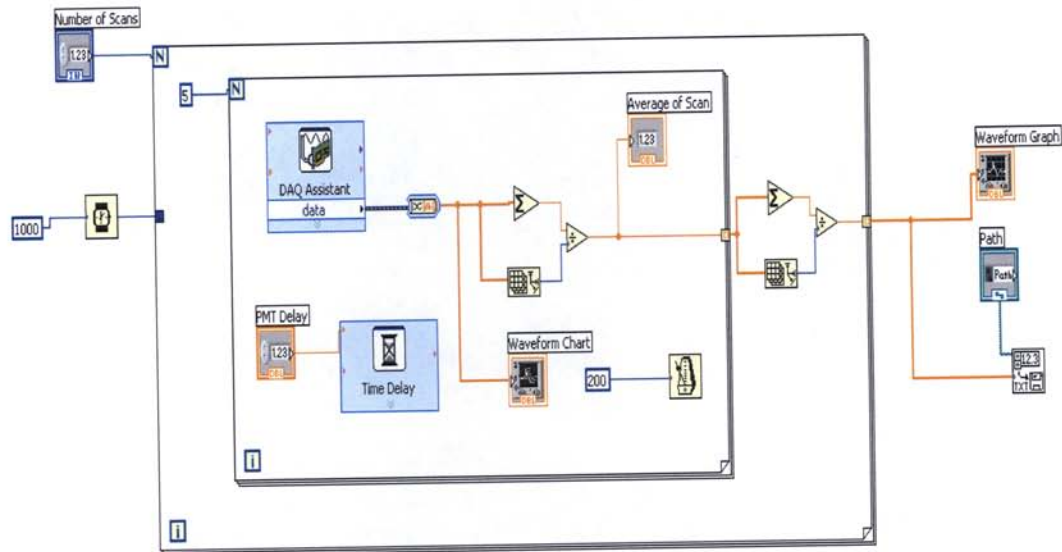
3.2.1: PMT and Nozzle Programs

The first step to controlling the instrument was to write a program that accumulated data from the PMT. This program needed to read an incoming signal from the appropriate input channel and plot the spectrum. These channels are located on the Data Acquisition Board or DAQ board, which is wired directly between the PMT and computer. In order to do this, the program needed to record a specified number of samples per monochromator step and average these samples together. The averaged sample then needed to be collected and

sent to a graph so that the final picture was a spectrum where each data point represented one monochromator step. Also, timing controls needed to be present in order to synchronize this VI with the nozzle and monochromator VIs discussed below. Finally, the averaged points needed to be saved to a file that could be named using a control on the front panel. Previously written VIs, such as PMTcontrol.vi, PMTchartrecorder.vi, and CRDSSamplefiredata.vi and CRDSSamplecollect.vi, were available as references^[6].

The resulting program was named PMTmeas.vi as seen in Figure 3.2. See Appendix B for a summary of LabVIEW functions, symbols and their meanings. Focusing on the block diagram (Figure 3.2(a)), the data is collected through the DAQ assistant sub VI, in which the number of samples to be collected and the rate are specified as input on the front panel. This PMT data is then converted into an array and averaged through array and math functions to give a single data point which is plotted in the Waveform Chart indicator so that the user can see the data as it is read. The outer *For* loop connected to the number of scans represents the number of steps the monochromator will be taking. The Waveform Graph is placed outside of the *For* loop so that after all of the data is averaged and indexed into a separate array, a spectrum is plotted. The *Write to Spreadsheet* function, connected to the *File Path* control is also located outside the *For* loop so that the only data that is saved is the averaged spectrum. The *Time Delay* sub VI, *Wait Until Next* and *Wait* functions and inner *For* loop are all present in order to synchronize the PMT with the other parts of the instrument.

a)



b)

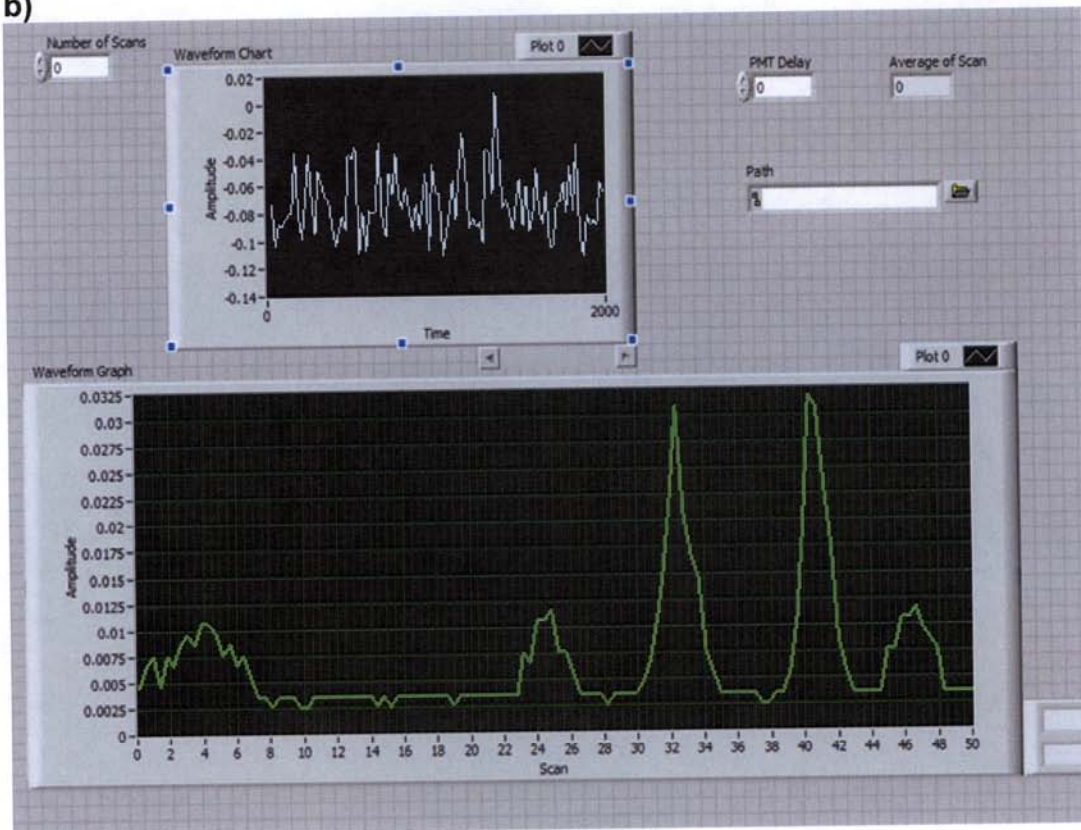


Figure 3.2: a) Block diagram and b) front panel of the `PMTmeas.vi` program. The waveform chart shows data being collected in real time and the waveform graph shows the final spectrum, in this case of argon. Also note the controls for Number of Scans, PMT Delay and Path.

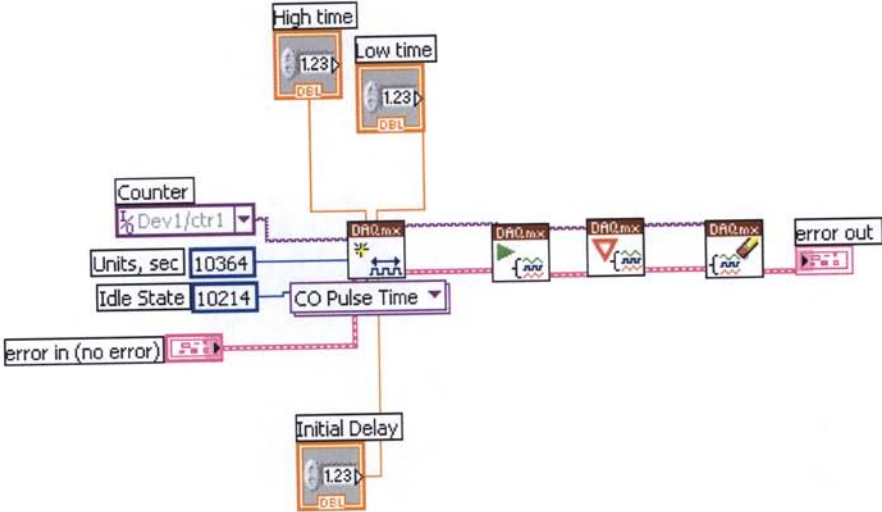
When PMTmeas.vi was complete, a way of controlling the detector from the computer was present. It was then time to move on to determining a way of controlling the instrument source; the pulsed discharge nozzle. The goal in controlling the nozzle was to produce a program that was able to communicate with the Iota One nozzle controller. Controls needed to be present that specified the open time of the nozzle as well as the closed time. These can be seen in the *High Time* function, representing the control for the time the nozzle would be open, in milliseconds. The *Low Time* function indicates the control for the time the nozzle is closed during one cycle. The last control is present as the *Initial Delay* function, which simply specifies any delay the user might want before the nozzle fires. Again, timing functions were necessary for synchronization. A program had been written formerly, labeled as lasersinglefire.vi^[6], which produced a single laser shot using identical parameters needed for the nozzle. This program was adapted and renamed NozzleFire.vi, shown in Figure 3.3, with the intention that surrounding this with a *While* loop would allow it to fire continuously until the *Stop* control was pushed.

3.2.2: Instrument Control and Optimization Programs

The monochromator being used for this instrument included its own utility VI responsible for controlling all necessary parameters. Rather than trying to break this program down into its individual aspects, it was determined that an easier, less time-consuming route would be to integrate PMTmeas.vi and NozzleFire.vi into this program and use it as the VI that would control the instrument as a whole, labeled MainControl2.vi, shown in Figures 3.4 and 3.5.

The controls present on the right side of the front panel correspond to a series of case structures within the block diagram, which are the parts added to the commercial monochromator VI.

a)



b)

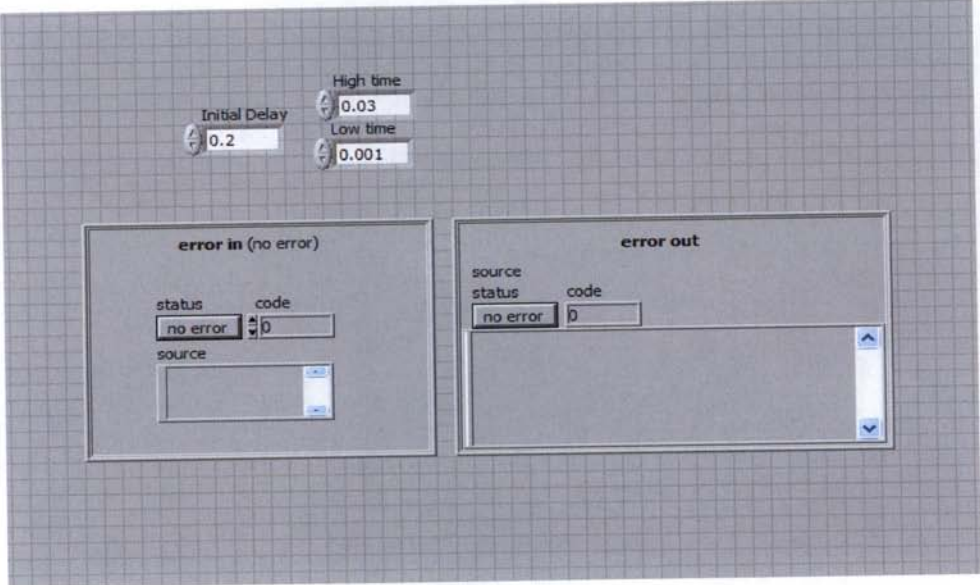


Figure 3.3: a) Block diagram and b) front panel of the NozzleFire.vi program. Note the controls for the High Time, Low Time and Initial Delay of the Nozzle

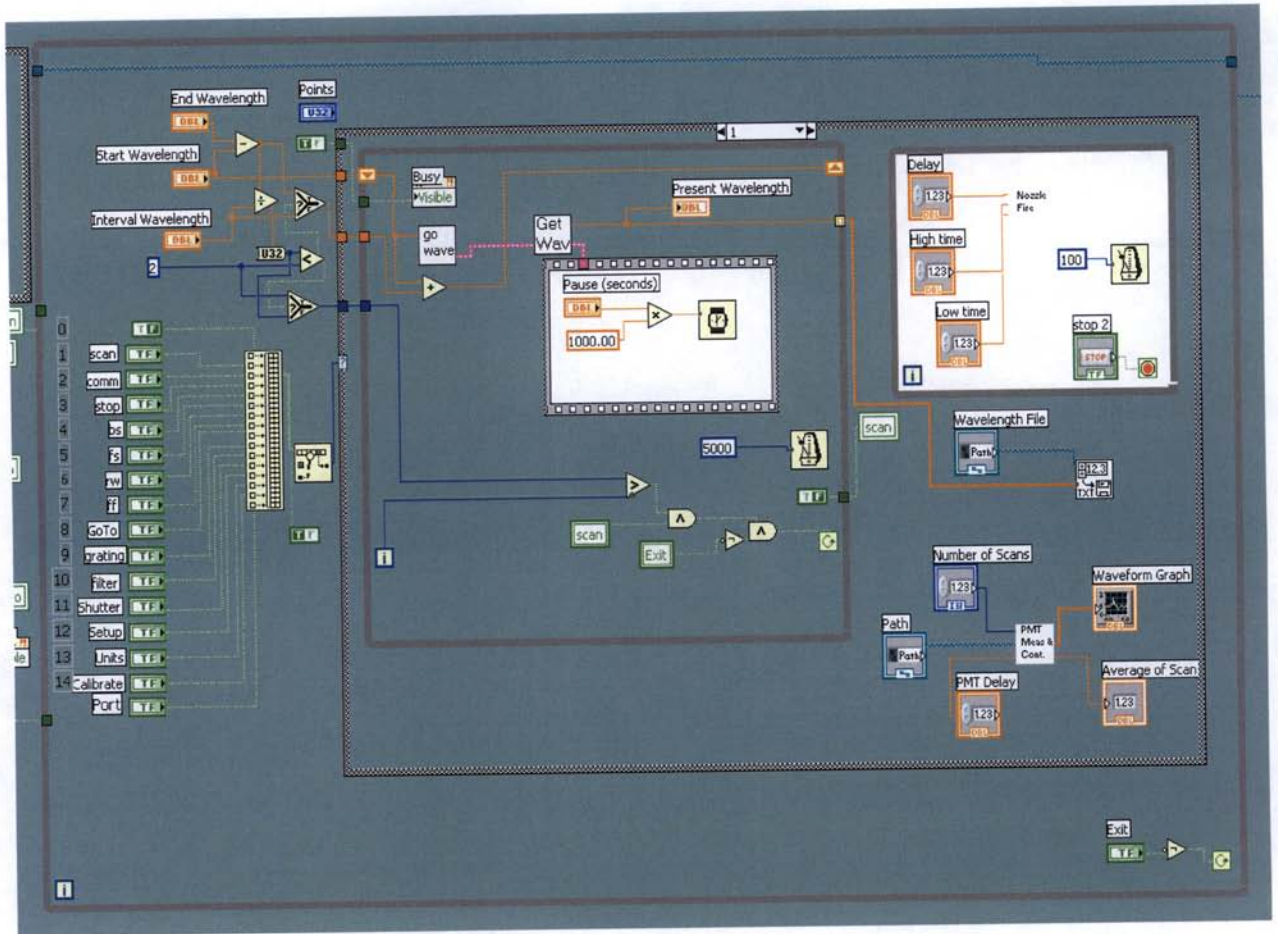


Figure 3.4: Block diagram of the MainControl2.vi program, showing where PMTmeas.vi and NozzleFire.vi (shown by their names on the diagram) have been integrated into a case structure.

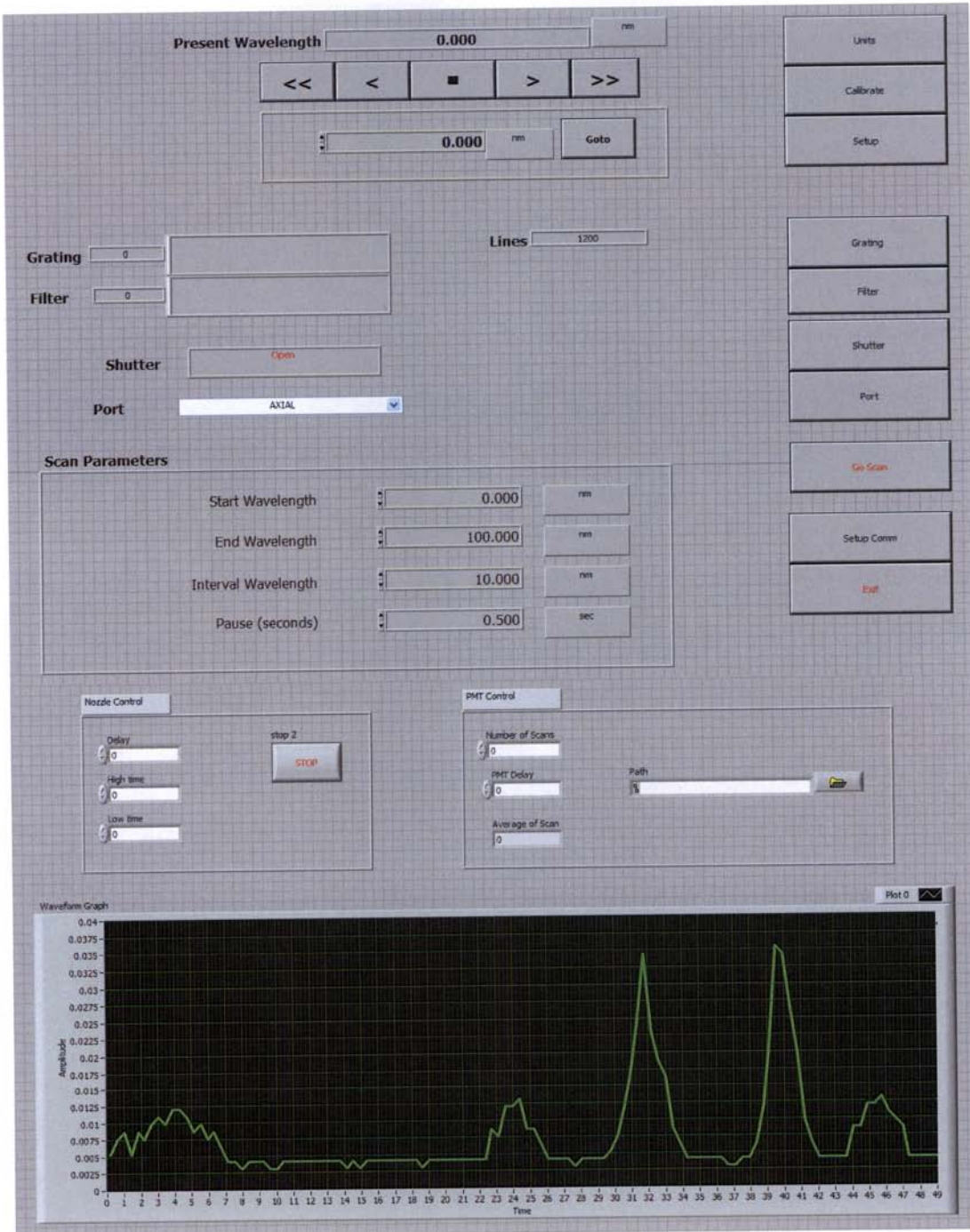


Figure 3.5: Front panel of the MainControl2.vi program. All controls and functions below the “Scan Parameters” section originate from the written VIs and were integrated into the provided monochromator VI. Note the regions corresponding to nozzle and PMT control with controls and indicators corresponding to Figure 3.3 and Figure 3.4.

Because the nozzle and PMT programs would only need to be called when the monochromator was scanning, these VIs, now being used as sub programs, were placed into the case structure used when the *Scan* button was selected in *MainControl2.vi*. A case structure encloses a sequence of code that is only executed in the event of a specific control being used, or other specific “either-or” type conditions being met. The nozzle firing program was placed inside a *While* loop with a *Wait Until Next* function in order to control how quickly the loop occurred. According to Figure 3.4, this means that the nozzle will fire once every 200 ms, or 5 shots per second. Nozzle and PMT control sections were added to the front panel so that the final result was one cohesive program to run the entire spectrometer.

Also, a program was needed that could help optimize instrument conditions to give the strongest signal possible. This program simply included a slight modification of *PMTmeas.vi*. A waveform chart was added into the inner *For* loop so that each data point can be viewed as its being collected. This program is run while the monochromator sits on a specific wavelength of a previously observed emission signal and the nozzle is being controlled by the Iota One controller. This allows the tester to view the effects of different nozzle settings as it is being fired. The block diagram for this program is not shown, since it appears essentially the same as *PMTmeas.vi*.

3.2.3: Early testing of the program

Once MainControl2.vi was finished, the program was tested using atomic discharge lamps placed in front of the monochromator at the entrance slit in order to acquire the spectrum. The hydrogen, mercury and helium spectra were measured, and with each spectrum improvements were observed in the quality of the data obtained.

The first test involved a hydrogen lamp using MainControl2.vi to run the instrument and acquire the spectrum. It should be noted that at this point, the discharge nozzle was being run by the program in order to try and determine if everything was synchronized by the program, but the power supply connected to the nozzle was not on and the source of the spectrum was only the hydrogen lamp. The result of this early test can be seen in Figure 3.6, which shows the 400 – 500 nm region of the hydrogen lamp. The spectrum that was produced was very poorly resolved yet reproducible. The poor resolution and high baseline were expected as the slit width of the monochromator was as wide as was possible. The reproducibility of the spectrum, however, gave early indication that the program was working as intended. A table of the peaks compared to literature data can be seen in Table 3.1^[7]. The peaks match fairly well, with the strongest line only differing by 1 nm. The additional lines seen in the hydrogen lamp can be attributed to the age of the lamp, resulting in contamination of the discharge. A new hydrogen lamp source was not obtained, however, as the goal of these early spectra were reproducibility in the measurements.

Table 3.1: Peaks from hydrogen spectrum compared to literature data. Uncertainties in experimental data are around +/- 1.0 nm

Hydrogen Lamp Data		Literature Data ^[7]	
Wavelength (nm)	Intensity	Wavelength (nm)	Rel. Int.
408	0.038	410.2	w
421	0.049	434.0	m
443	0.034		
446	0.036		
449	0.036		
458	0.045		
464	0.046		
487	0.054	486.1	s
494	0.046		

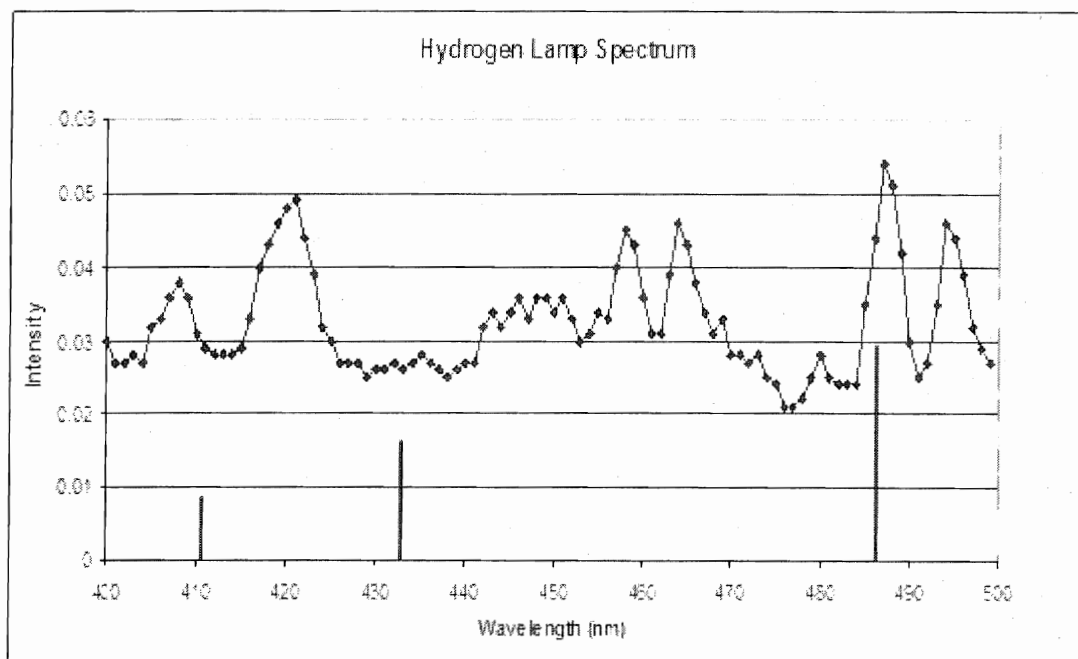


Figure 3.6: Hydrogen spectrum from the atomic discharge lamp source showing early results that the program was working as intended. The literature line spectrum is shown superimposed.

After making adjustments to the program and spectrometer settings, the program was then tested using a mercury discharge lamp using the same method used to acquire the hydrogen spectrum. The 400 – 500 nm region of this spectrum can be seen in Figure 3.7. This spectrum gave a much improved signal-to-noise ratio, indicating a possible optimization of the PMT settings. This spectrum shows an apparent two peaks located at roughly 425 and 430 nm. According to known data, the emission spectrum of mercury contains only one major line in this region^[7] (Table 3.2). This indicated that the intensity limit of the PMT controller had been reached and the signal had wrapped, causing the appearance of two separate peaks. The intensity limit was then increased for further experiments. There was some variation between experimental and literature data which can be attributed to the settings that were currently being used for the spectrometer. The slit width had not been optimized at this point and was left completely open. This decreased resolution greatly and could skew the peak wavelength. Some peak wavelengths appeared to be up to 15 nm from where their literature values indicated they would be.

Table 3.2: Peaks from the mercury spectrum compared to literature data. Uncertainties in experimental data are around +/- 1.0 nm

Mercury Lamp Data		Literature Data ^[7]	
Wavelength (nm)	Intensity	Wavelength (nm)	Rel. Int.
<400	0.024	404.0	w
425	0.094		
430	0.078	439.9	s
		466.1	m
482	0.006	482.6	m

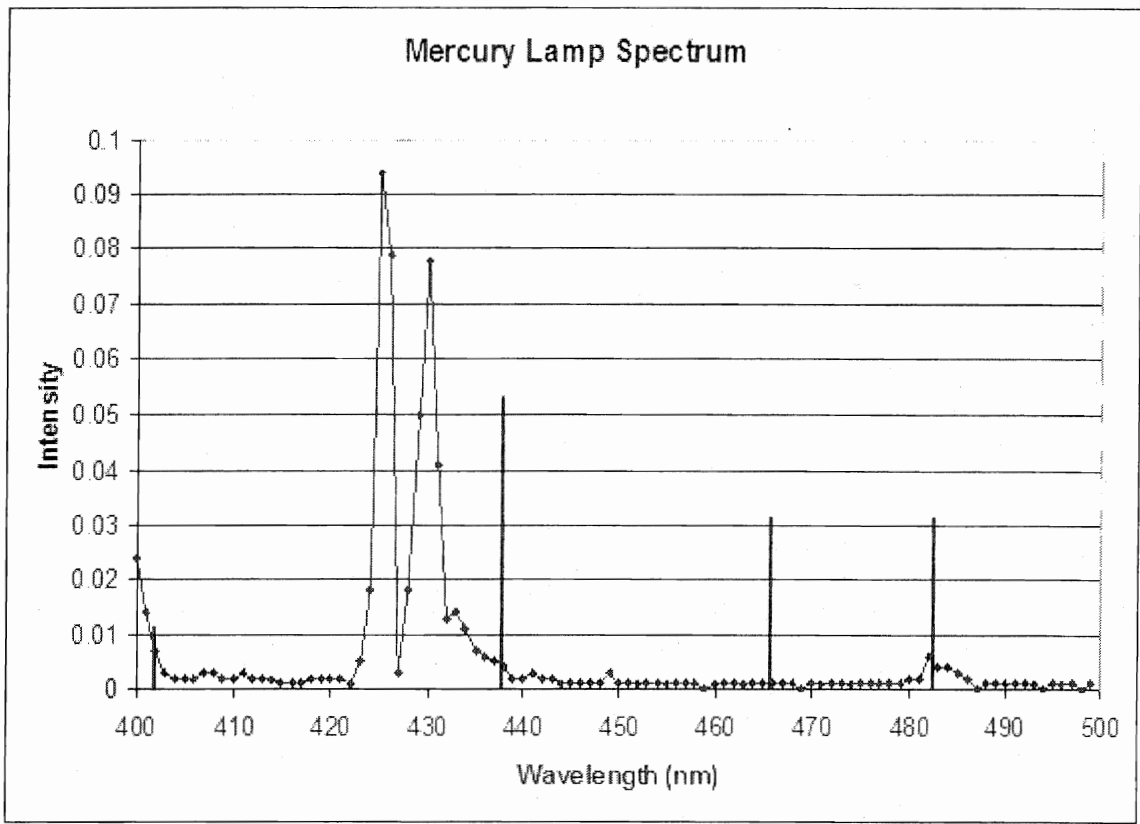


Figure 3.7: Emission spectrum of mercury using an atomic discharge lamp. This spectrum showed a need to adjust the intensity limit of the PMT as the strong two lines are actually one line split in the center. Literature line spectrum is shown superimposed.

After further adjustments to the central program, the accuracy was finally tested using a helium discharge lamp. The 400 – 750 nm region of this spectrum is shown in Figure 3.8. The table of helium peaks compared to literature data can be seen in Table 3.3. This spectrum again showed good S/N ratio with five separate peaks at intensities high enough to be detected. The strongest peak measured is located at 588 nm. This closely matches the strongest known peak of the helium spectrum which occurs at 586 nm^[7]. Other peaks also closely

match the literature data, indicating that wavelength calibration and program function are finally optimized. More specifically, using the H lamp, some peaks seemed to be off their literature value by around 15 nm. The results of the Hg discharge lamp were closer but still contained a peak around 10 nm from its literature value. The He spectrum contains the most accurate data of the three with the lines matching the literature data to within 1 – 2 nm. The reason for the choppy appearance of the helium spectrum in Figure 3.8 was determined to be an internal setting within the LabVIEW program determining how many decimal places to record from the PMT. This appearance was fixed by changing the number from three to six. Having shown that MainControl2.vi was working properly, the nozzle could now be tested along with the rest of the instrument.

Table 3.3: Helium emission peaks compared to literature data. Uncertainties in experimental data are around +/- 1.0 nm

Helium Lamp Data		Literature Data ^[7]	
Wavelength (nm)	Intensity	Wavelength (nm)	Rel. Int.
447	0.006	447.1	m
501	0.006	501.6	w
588	0.042	587.6	s
668	0.006	667.8	w
706	0.008	706.5	m

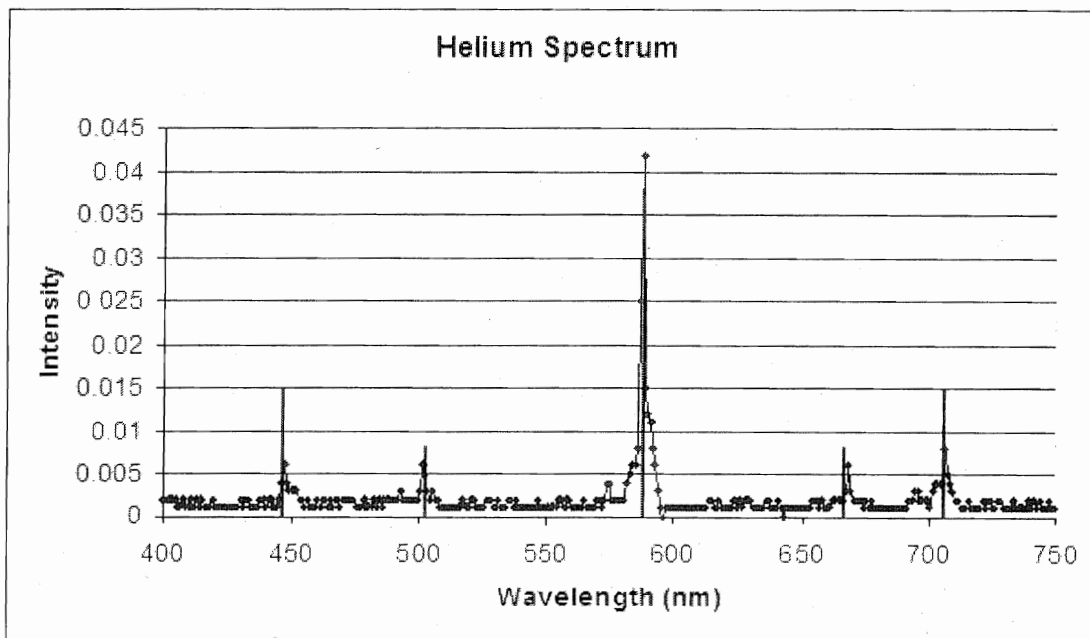


Figure 3.8: Emission spectrum of helium using an atomic discharge lamp. The accuracy of this spectrum indicated that the program was working properly and the PDN could be integrated. Literature line spectrum is shown superimposed.

3.2.4: Iodine

The next step in the characterization of the PDN as well as further confirmation of a working program included running the spectrometer with the nozzle acting as the source, rather than atomic discharge lamps. The first spectrum that was acquired this way was argon, which was being used as the carrier gas. This spectrum indicated that the nozzle could be used as the source of the emission spectrometer and give realistic results. The 700 – 800 nm region of this spectrum can be seen in Figure 3.9. This was the region of the spectrum that showed the highest amount of activity. The spectral lines that were produced in this spectrum matched known data for the visible spectrum of argon^[7]. An experimental comparison to literature data for this region of argon

can be seen in Table 3.4. At this point in the early recording of spectra, the accuracy of the results had improved to within 1 nm. This was a result of fine tuning the timing and scanning settings on the emission spectrometer.

Table 3.4: Argon emission peaks compared to literature data. Uncertainties in experimental data are around +/- 1.0 nm

Argon Carrier Gas Data		Literature Data ^[7]	
Wavelength (nm)	Intensity	Wavelength (nm)	Re. Int.
705	0.011	706.7	s
713	0.016	714.7	s
737	0.026	738.4	s
750	0.039	750.4	s
762	0.033	763.5	s
771	0.031	772.3	s

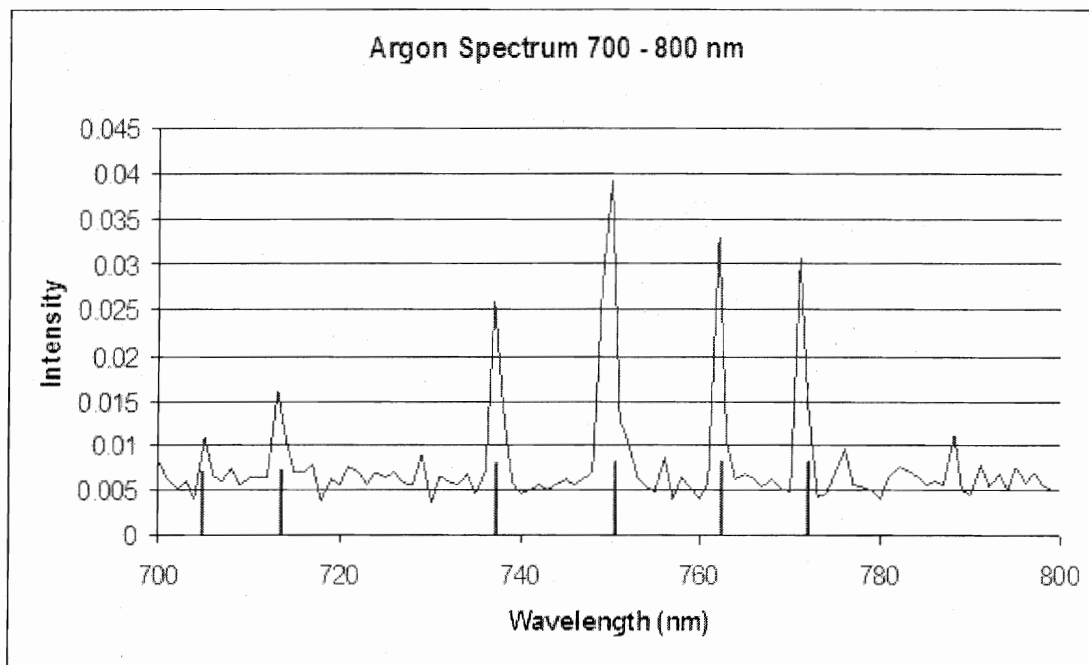


Figure 3.9: Emission spectrum of the argon carrier gas in the 700 – 800 nm region. Literature line spectrum is shown superimposed.

The final step in these early experiments was to put I_2 through the nozzle in order to verify that a molecule could be run through the spectrometer and would produce a visible emission spectrum. To record this spectrum a small crystal of I_2 was placed at the entrance of the U-tube with the carrier gas flowing over it. The 300 – 320 nm regions and 610 – 630 nm section of this spectrum can be seen in Figures 3.10 and 3.11, respectively (averages of three scans with 5 μ m slit width and 0.1 nm monochromator steps). These areas were the spectral regions that showed the highest amount of activity. The clump of lines that appear in the 610 – 630 nm area could possibly be part of the $v = 2$ excited state of I_2 which would be expected to appear in the 610 to 650 nm region^[8]. This is uncertain, however, because the intensity of the lines from 610 to around 617 nm should be much greater^[8]. Furthermore, the 300 – 320 nm section does appear to match known data of I_2 but again, the 300 – 306 nm regions should show some activity if this is the case^[7]. The experimental iodine peaks that were compared to literature data can be found in Table 3.5^{[7],[8]}. Despite the discrepancy in some of the results compared to known data from literature, the iodine measurements confirmed that the nozzle as well as the written software was working properly. Confirmation of a properly working nozzle came in a color change in the discharge. If only the argon carrier gas is coming through the nozzle the discharge will appear to be very pinkish purple. When iodine is discharging through the nozzle properly, the discharge changes color to a deep blue violet color.

Table 3.5: Iodine emission peaks compared to literature data. Uncertainties in experimental data are around +/- 0.1 nm

<u>Experimental</u> <u>Wavelength</u> (nm)	<u>Experimental</u> <u>Intensity</u>	<u>Literature</u> <u>Wavelength</u> ^{[7],[8]} (nm)	<u>Literature</u> <u>Rel.</u> <u>Int</u> ^{[7],[8]}
307.4	0.015		
308.6	0.024	307.9	w
309.5	0.026		
310.1	0.018		
310.3	0.018		
313	0.010		
314.9	0.010		
		316.1	s
		317.5	w
613.1	0.035	612.7	m
614	0.029		
614.4	0.023		
614.8	0.025		
616	0.048		
616.7	0.043		
617	0.018		
617.6	0.058		
618.4	0.050		
618.9	0.041		
619.5	0.055	619.2	m
620.2	0.055		
620.7	0.040	620.5	s
621.5	0.029	621.3	m
622.2	0.025		
623.3	0.020		
623.9	0.026		
624.8	0.027	624.5	w
625.9	0.027	625.7	w
626.4	0.023		
627.3	0.019		
627.8	0.020		
628.4	0.015		
628.9	0.019	629.4	w
629.9	0.019		

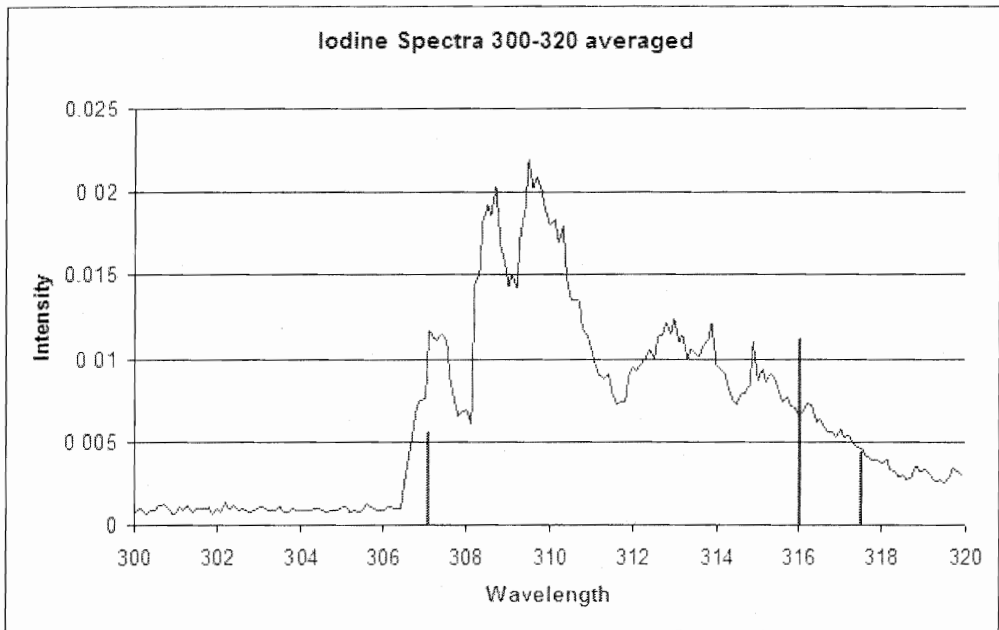


Figure 3.10: Emission spectrum of iodine in the 300 – 320 nm region indicating that the PDN was working properly. Literature line spectrum is shown superimposed.

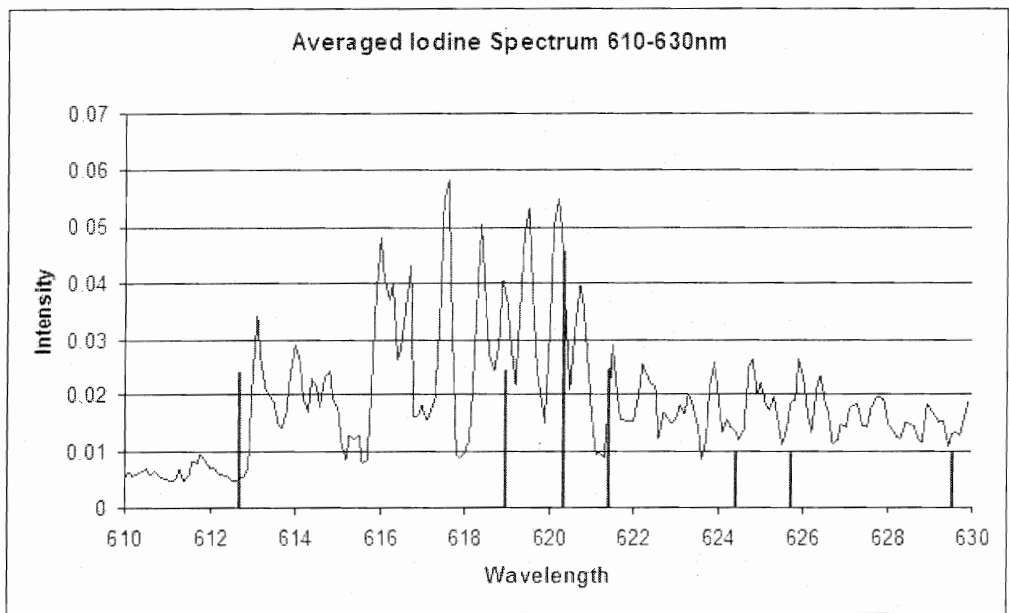


Figure 3.11: Emission spectrum of iodine in the 610 – 630 nm region indicating that the PDN was working properly. Literature line spectrum is shown superimposed.

3.3 Toluene

The confirmation that was received as a result of the iodine tests allowed the discharge studies to move forward to creation of free radicals. The first compound that was placed through the PDN was toluene, in an attempt to create the benzyl radical. This was chosen first due to the similarity in the compounds to the pentafluorobenzyl radical. Toluene is currently one of the most common VOC compounds present in the atmosphere. Since these compounds would be part of the focus of future studies, toluene seemed like a good molecule to begin with. Using the nozzle settings described above, as well as the experimental method described in Chapter 2, general scans of the molecule were recorded from 300 to 800 nm. Three main areas of activity were detected using this method. These were located from 400 – 500 nm, 600 – 700 and 700 – 800 nm regions.

The discharge that was produced by toluene was a blue-green color that brightened when the settings were optimized. The similarity in some areas of the 600 – 700 nm spectrum to that of iodine led to the conclusion that some contamination was taking place. Two areas that contained lines possibly due to iodine were the 600 – 610 nm and 670 to 680 nm regions which were rescanned to improve resolution. Furthermore, the 700 – 800 nm region was found to match with the 700 – 800 nm region of argon, indicating that it was the carrier gas which was coming through in this region. The true area of activity was, therefore, the 400 – 500 nm region. This was the region that was focused on to improve resolution by lowering the monochromator to 0.1 nm steps for the region from

400 – 450 nm. The 450 – 500 nm area showed very limited activity and was, therefore, not considered. The resulting improved 400 – 450 nm spectrum of toluene can be seen in Figure 3.12 which is an average of three scans taken of the region. The peak data for this region can also be seen in Table 3.6.

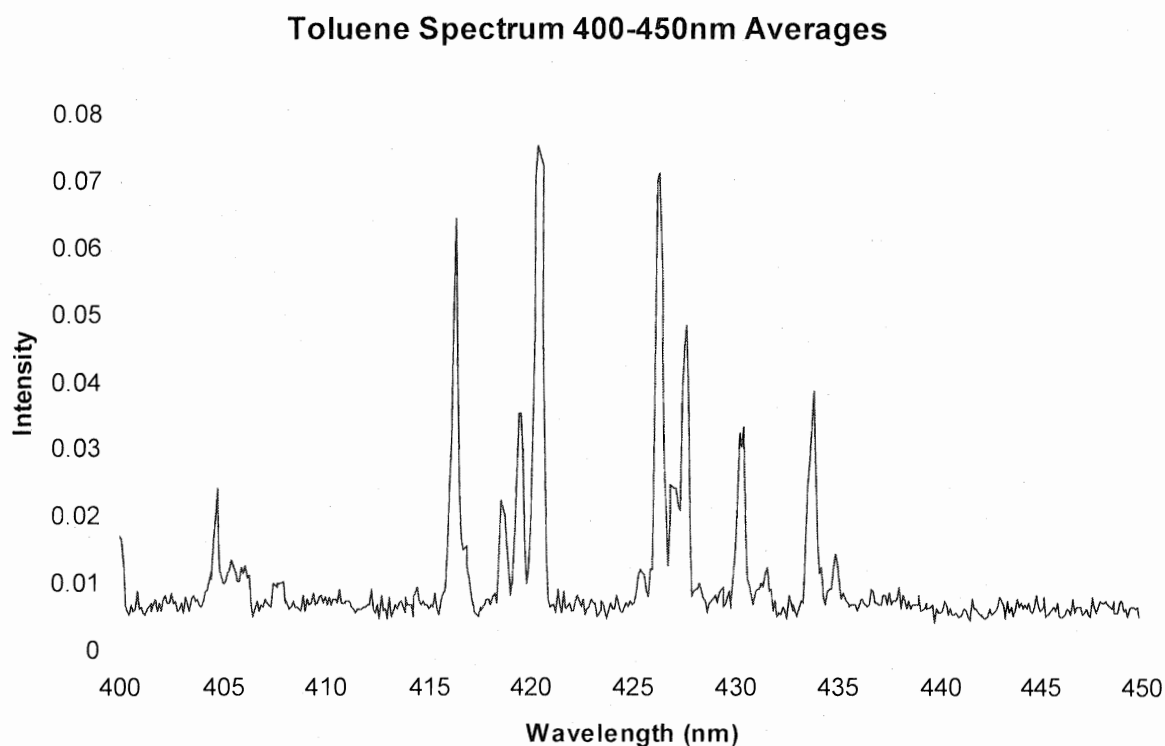


Figure 3.12: Emission spectrum of the discharge products of toluene in the 400 – 450 nm region.

These results were compared to literature information on the emission spectrum of benzyl radical recorded using similar methods^{[9],[10]}. The main spectral regions for the benzyl radical have been previously determined to be

from 450 – 500 nm and around 310 nm, indicating that the benzyl radical was not being produced at this time^[9]. Comparison was also done to previous data on the emission spectrum of toluene^[11]. This earlier study indicated that the main band of the spectrum occurs at 250 – 300 nm, an area that the monochromator at EIU will not measure reliably^[11]. Interestingly, this study showed that when studying these molecules by electron impact, electronically excited H and CH species will fragment from the parent compound. Also, these fragments will emit in the 400 – 450 nm region^[11], similar to what was seen in the toluene spectrum shown above. Other possibilities for this region include emission from C₂ or C₃ fragments which will be discussed later.

Table 3.6: Toluene and Xylene emission peaks compared to literature data^[11] on emission products from electron impact experiments. Uncertainty for wavelength measurements was around +/- 0.1 nm.

<u>Experimental</u> <u>Toluene</u> <u>Wavelength (nm)</u>	<u>Experimental</u> <u>Toluene</u> <u>Intensity</u>	<u>Experimental</u> <u>Xylene</u> <u>Wavelength (nm)</u>	<u>Experimental</u> <u>Xylene</u> <u>Intensity</u>	<u>Literature</u> <u>Toluene</u> <u>rel. nm.</u>	<u>Literature</u> <u>Xylene</u> <u>rel. nm.</u>
400.0	0.017				
404.7	0.024	404.8	0.013	410	410
416.3	0.064	416.6	0.037		
		417.0	0.010		
418.6	0.021				
419.5	0.035	419.7	0.021		
420.3	0.075	420.5	0.042		
426.3	0.071	426.5	0.029		
426.9	0.025			427	427
427.6	0.048	427.8	0.019		
430.4	0.033	430.6	0.020		
433.8	0.039	434.0	0.022		
				437	438

3.4 Xylene

After the emission spectrum of toluene had been recorded, xylene was put through the PDN to compare the results to that of toluene. Using the same experimental method, three main areas of activity were detected; these were the 300 – 400 nm, 400 – 500 nm and 600 – 700 nm areas. In this case all three areas of activity were focused on using 0.1 nm monochromator steps. The similarity to the spectrum of iodine again, in the 600 – 700 nm section indicated further contamination of iodine. The nozzle was taken apart and cleaned thoroughly with acetone, at which point, activity in the 600 – 700 nm spectral region was much weaker, confirming that these peaks were due to contamination. The 300 – 400 nm section was scanned repeatedly but was not found to be reproducible. Therefore, the true area of activity of xylene was again the 400 – 500 nm spectrum. This area can be seen in Figure 3.13 as an average of 3 scans. The peak values for xylene are also seen in Table 3.6.

Comparison was again done between these results and known literature data. The emission spectra of xylene from the same electron impact study looked very similar to that of toluene in Table 3.6 with 7 lines agreeing to within 1 nm. The main spectral activity of the parent compound occurred from 250 – 300 nm region with evidence of H and CH fragments occurring at 400 – 450 nm^[11]. The experimental spectrum from the 450 – 500 nm region of xylene does also show a small amount of activity. This is the same region where the main vibrational band has been assigned for the benzyl radical^[9]. It is likely that H fragments will be present within the discharge as well as CH from the methyl

groups from the ease with which these fragments can dissociate. It is also possible that C_2 and C_3 can be present as the molecule could be completely dissociated from the high voltages used. This will be discussed below.

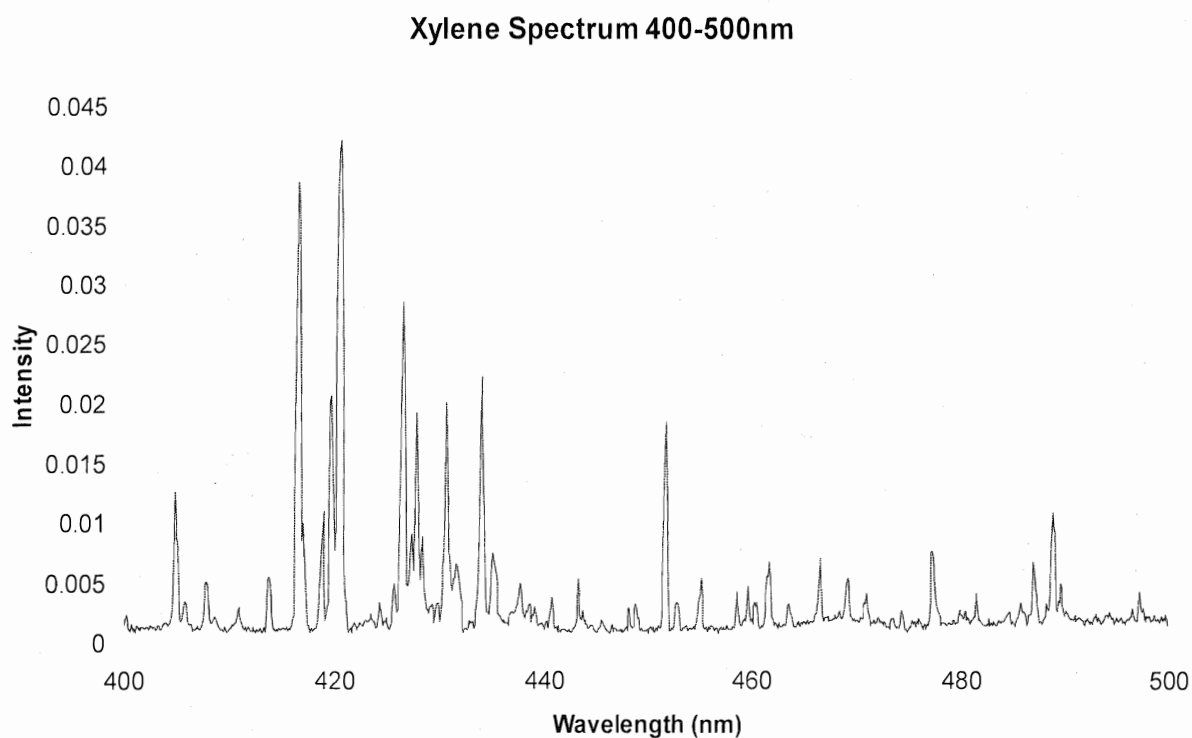


Figure 3.13: Emission spectrum of the discharge products of xylene in the 400 – 500 nm region.

3.5 Results and conclusions

The experimental spectra of both toluene and xylene had one main area of activity in the 400 – 500 nm region. In addition to having the most activity

occurring in the same region, this looked almost identical in both molecules. A table comparing the peaks from both compounds to the emission spectra from the electron impact experiment^[11] can be seen in Table 3.6. A picture of the toluene spectrum from electron impact can be seen in Figure 3.14. A comparison of this region between both of these molecules can be seen in Figure 3.15.

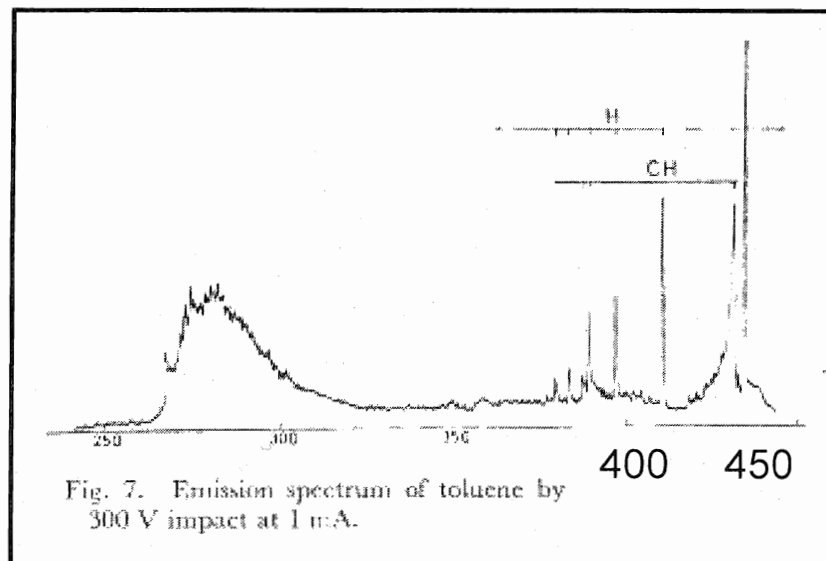


Figure 3.14: Toluene emission data by controlled electron impact^[11]. Wavelength data is displayed in nm. H and CH fragments in the 400 – 450 nm region seem to match toluene and xylene PDN data.

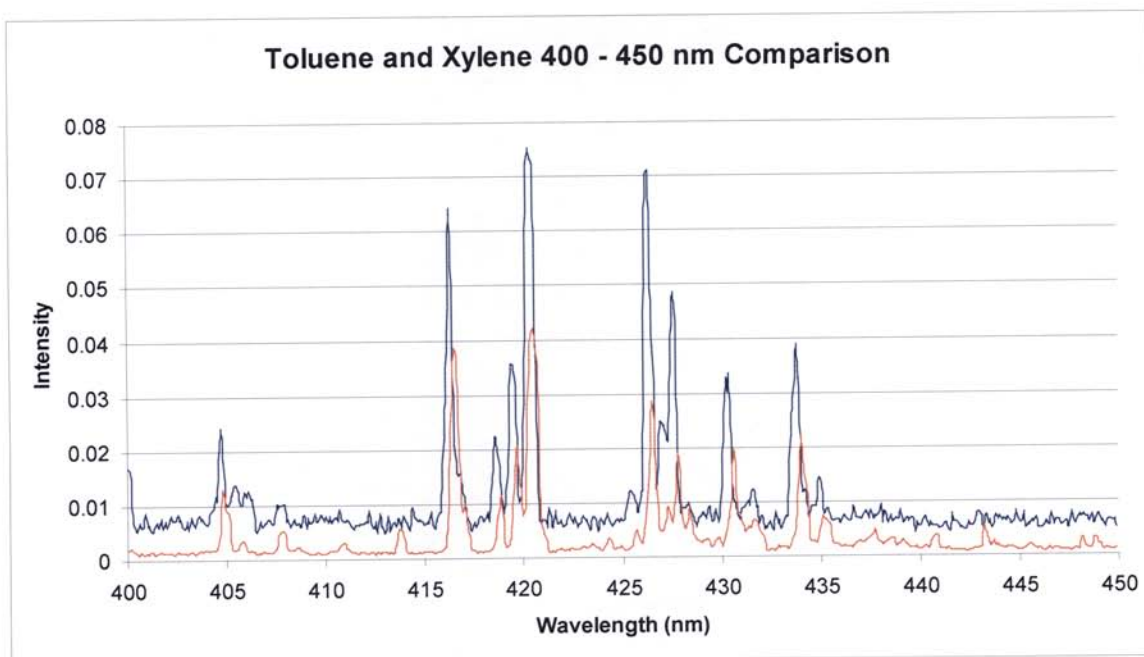


Figure 3.15: Comparison of the 400 – 450 nm region of the discharge products of toluene and xylene. The blue line represents toluene data with the red line indicating xylene data. Both compounds have a similar pattern in this region indicating that the discharge products for both compounds are similar.

The similarity of the peak wavelengths in the 400 – 450 nm region between the two molecules along with the comparison of this region to the emission spectra of H and CH indicated that radicals were probably being produced. There does seem to be a systematic error between toluene and xylene in this region but this is likely due to instrumental effects that are not yet completely understood. When referring back to Table 3.6 and Figure 3.16, the emission line around 427 nm seems to be from the CH radical with the lines around 415 and 437 nm resulting from the H spectrum. Also, it can be confirmed that the compounds that are being formed through the PDN do not include the parent compounds. Despite the majority of the emission spectra of both toluene

and xylene being earlier than the 300 nm region, there should be some measurable activity occurring in the 300 to 350 nm region^[11]. However, this was not observed.

Flame tests were done to further rule out the possibility of electronic excited states of the parent compounds. These tests, however, were inconclusive. During these tests, a nichrome wire was looped and dipped into a liquid sample to be placed into the flame of a Bunsen burner. The resulting emission of the sample in the flame was detected using a photodiode array spectrometer. Between the samples, the wire was cleaned by dipping it into HCl and heated until glowing red. For all of the samples during this procedure, there was an initial burst of yellow color in the flame followed by only a brief emission line at around 580 nm on the spectrometer. This matches emission data from sodium, leading to the conclusion that this emission line was due to contamination.

A second study has given other possibilities for what is causing the weak emission lines in the 450 – 500 nm region of xylene. This study observed the emission spectrum of CH and C₂ in an oxyacetylene flame^[12]. Results of this study indicated that some spectral emission bands from the C₂ molecule occurred in the 465 – 475 nm region. These lines can be seen in Figure 3.16. The presence of C₂ fragments could, therefore, be the reason for some of the lines that can be seen in the spectrum of xylene above. The lines in this region that were obtained for xylene experimentally were very weak, but with this type of experiment more than one product at different concentrations usually forms

within the discharge. It is likely that the products include the H and CH radical as well as possibly C_2 and C_3 fragments at different concentrations. C_3 fragments are reported in another experiment reported in the literature which found emission lines from C_3 in the 380 – 420 nm region^[13]. This could be the reason for some faint emission lines seen in the 380 – 400 nm region as well as the 400 – 420 nm region.

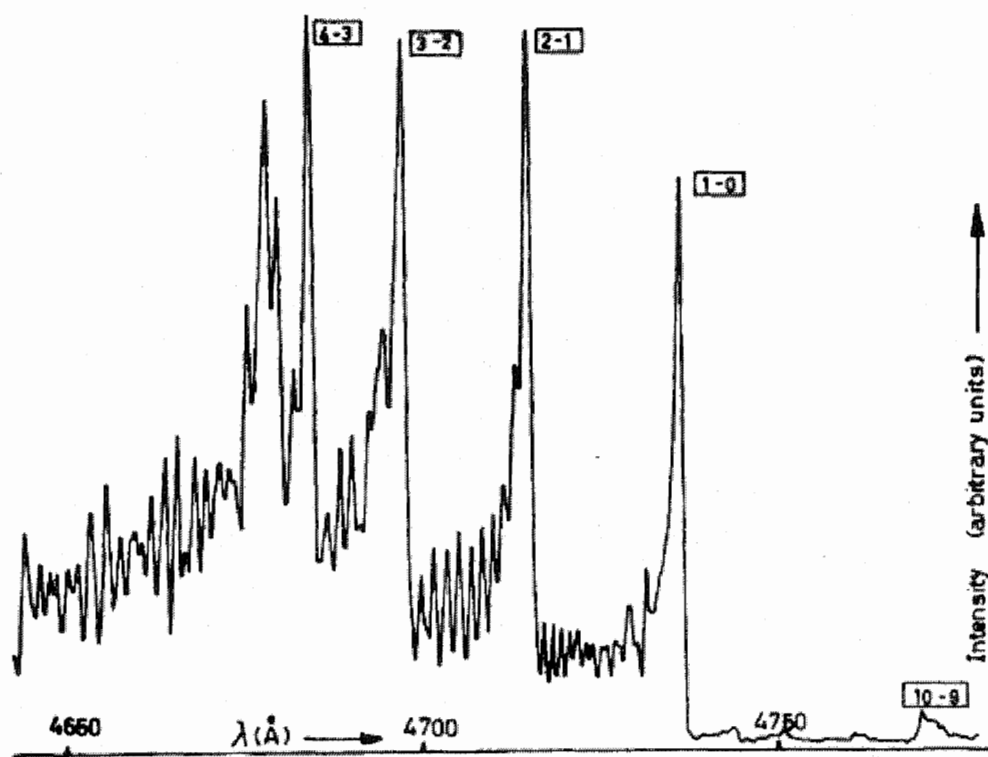


Figure 3.16^[12]: Emission spectrum of C_2 in the 465 – 475 nm region. Wavelengths are displayed in angstroms, (Å). This pattern appears to match weak transitions in the xylene spectrum around 470 nm.

In conclusion, these discharge studies allowed for the optimization of discharge nozzle conditions and confirmation of working computer software. The

programs that were written using LabVIEW^[2] software were written specifically for this instrument. The discharge emission studies gave confirmation that the programs were working as intended. This confirmation came through the simple recording of spectra, of H, Hg, He, Ar and I₂ and allowed for tweaking of the internal settings of the programs including significant figures, number of acquisitions per monochromator step and instrument synchronization. When optimizing nozzle conditions, the early discharge experiments indicated that the settings described in Chapter 2 give the best discharge from the PDN, with the highest intensity during spectral acquisition as well as the strongest glow from the discharge inside the chamber. The spectra of toluene and xylene discharge products confirm that free radicals (possibly H, CH, C₂ and/or C₃) are being formed in the PDN; however, further work is needed to confirm the production of the benzyl radical product that was desired from toluene and xylene. If production of benzyl radicals is confirmed, studies can then move on to recreation of the pentafluorobenzyl radical spectrum^[1] and finally, creation of the midinfrared spectrometer.

References: Chapter 3

- [1] Lee, S.K.; Baek, D.Y. *Chem. Phys. Lett.* **1999**, 311, 36 – 40.
- [2] LabView 7.1, National Instruments Inc., 2004.
- [3] Stearns, J. The fate of electronically excited molecules: Photochemical reactivity and excitonic interaction. Ph.D. Thesis, Purdue University, West Lafayette, IN, 2005.
- [4] Newby, J.J. Purdue University. Private communication, 2009.
- [5] Beyon, J. In *LabVIEW; Programming, Data Acquisition and Analysis*. Prentice Hall PTR: New Jersey 2001.
- [6] Roden, J. *LabVIEW 7.1 Update and Cavity Ringdown System Programs*. Semester Report, Eastern Illinois University. Spring 2006.
- [7] Ralchenko, Y.; Kramida, A.E.; Reader, J., and NIST ASD Team (2008). *NIST Atomic Spectra Database* (version 3.1.5), [Online]. Available: <http://physics.nist.gov/asd3> [2009, September 1]. National Institute of Standards and Technology, Gaithersburg, MD.
- [8] Capelle, G.A.; Broida, H.P. *J. Chem. Phys.* **1973** 58(10).
- [9] Ono, Y.; Ikeshoji, T.; Mizuno, T. *Chem. Phys. Lett.* **1975**, 34(3), 451 – 454.
- [10] Selco, J. I.; Carrick, P.G. *J. Mol. Spec.* **1989**, 137, 13 – 23.
- [11] Ogawa, T.; Tsuji, M.; Toyoda, M.; Ishibashi, N. *Bull. Chem. Soc. Japan*. **1973**, 46, 2637 – 2642.
- [12] Bleekrode, R.; Nieuwpoort, W.C. *J. Chem. Phys.*, **1965**, 43(10).
- [13] Rosen, B. *Astronomical Journal*, **1961**, 66(8).

Chapter 4: Microwave Spectroscopy of Pentafluorotoluene

4.1 Introduction

Free radical compounds are one of the most important types of species in the study of atmospheric chemistry due to their high degree of reactivity and relatively high concentration within the stratosphere. Volatile organic compounds, or VOCs, and their radical species are of high concern in the study of atmospheric chemistry. While PFTOL and the pentafluorobenzyl radical are not atmospheric species themselves, they should react similarly to common VOCs due to their similar properties. As the pentafluorobenzyl radical was the one that would be studied first using the pulsed discharge nozzle, some information was desired on the structure and reactivity of its parent compound, pentafluorotoluene. Since the rotational spectrum of PFTOL had not yet been assigned, a project to study it using microwave spectroscopy was started. Studying the microwave spectrum of the parent species, using the process described in Chapter 2, allowed for the determination of the molecular structure as well as the dipole moment via Stark effect measurements.

Also of interest during this study was the effect of fluorine substituents on the aromatic ring. The main type of compound that will be studied once the infrared spectrometer is properly constructed are hydrochlorofluorocarbon species, or HCFCs. The rotational spectrum of toluene has already been well-

determined. Studying PFTOL in order to compare the results with toluene can give some indication of how the fluorine atom changes the structure of the molecule. One possible effect these atoms could have on the molecule overall is causing a difference in the energy barrier to internal rotation of the methyl group.

4.1.1: Stark Effect Measurements

In order for a molecule to be measured using microwave spectroscopy, it requires a permanent dipole moment, indicated by μ . This requirement also means that measuring the dipole moment experimentally is possible using a microwave spectrometer. As mentioned in Chapter 2, the total angular momentum of the molecule is represented by the quantum number J . The value of J will increase with each rotational energy level. The M_J quantum number is used to represent the projection of the angular momentum along an electric field axis. In the absence of an electric field these M_J components are degenerate. Once a field is applied, however, each J level will split into $(2J + 1)$ components so that the absolute value of $M_J = 0, 1, 2, \dots, J$. The splitting that occurs in the presence of an electric field is known as the Stark effect^[1].

During Stark effect measurements, an electric field is applied to the sample as it is being excited by microwave radiation. The magnitude of the splitting that occurs is proportional to the strength of the field, E , as well as M_J and the dipole moment. The relationship of the splitting to these values is given approximately (using second order perturbation theory) by Equation (4.1). This equation calculates the difference in frequency from the original line, $\Delta\nu$, using the Stark coefficients, A and B , the dipole moment, μ , projection of the angular

momentum, M_J , and electric field, E . Measuring the splitting that occurs within a transition, while varying the electric field, can then be used to measure the dipole moment. After observing the magnitude of the splitting that occurs, the Stark coefficient is calculated for each M_J observed by plotting $\Delta\nu$ vs. E^2 and determining the slope. These coefficients are then used to calculate the dipole moment through a least squares fit using the program DIPOLE^[2].

$$\Delta\nu = (A + BM^2)\mu^2E^2 \quad (4.1)$$

4.1.2: Internal Rotation

In addition to the molecular rotation of pentafluorotoluene, there will be internal rotation of the C-CH₃ bond. This internal rotation effect will cause the spectrum to split into A and E states at a magnitude dependent on the energy barrier to internal rotation of the molecule, V_3 . These two states are differentiated in the microwave spectra due to "tunneling" between the three potential minima of the states^[3]. Any molecule containing a methyl group may see evidence of the rotation of this bond within the rotational spectrum of the molecule. Commonly, high energy barriers to internal rotation cause splittings of around tens of kilohertz^[4]. In contrast, in the case of a low energy barrier, torsionally excited states are observed, commonly displaying large spacings between the transitions (tens or hundreds of megahertz) and exhibiting fast first order Stark effects. A first order Stark effect occurs when there is a linear relationship between the applied electric field, E , and the magnitude of the

splitting, $\Delta\nu$, as opposed to the quadratic relationship seen in Equation (4.1).

Evidence of this internal rotation was seen in the rotational spectrum of PFTOL and is discussed below.

When this type of splitting is apparent in a rotational spectrum, the energy barrier to internal rotation can be determined in multiple ways. One of these ways includes estimating the barrier from the planar moment, P_{cc} , of the molecule. P_{cc} is a measure of the planarity of the molecule and can be calculated using Equations (4.2) or (4.3). In the first equation, the planar moment, P_{cc} , is calculated using the three moments of inertia, I_a , I_b and I_c . The second equation determines P_{cc} by summing the mass of an individual atom, m_i , multiplied by the c -coordinate of the atom squared, c_i^2 . Internal rotation effects will cause a molecule to appear more planar, lowering the P_{cc} value from its predicted *ab initio* and structurally logical value. This type of estimation was done on pentafluorotoluene and is described along with the spectroscopic results below^[4].

$$P_{cc} = \frac{1}{2} (I_a + I_b - I_c) \quad (4.2)$$

$$P_{cc} = \sum m_i c_i^2 \quad (4.3)$$

4.2 Measurement observations

An initial observation that was made in the acquisition of the PFTOL rotational spectrum at EIU was that it contained many lines at very high intensity. Additionally, these lines often displayed a common pattern of transitions that

were grouped together. An example of this pattern can be found in Figure 4.1. These transitions reached high J transitions while still retaining good intensity and signal to noise ratio. The splitting seen in the figure is due to the Doppler effect, characteristic of an axial nozzle configuration. In addition to these groups of transitions, a Q-branch was measured and can be seen in Figure 4.2. A Q-branch refers to a series of transitions where $\Delta J = 0$. This particular Q-branch was able to be tracked up to the $J = 23$ transition. The measurement of transitions at high energy levels seen in these two observations is very uncommon using the FTMW spectrometer at EIU.

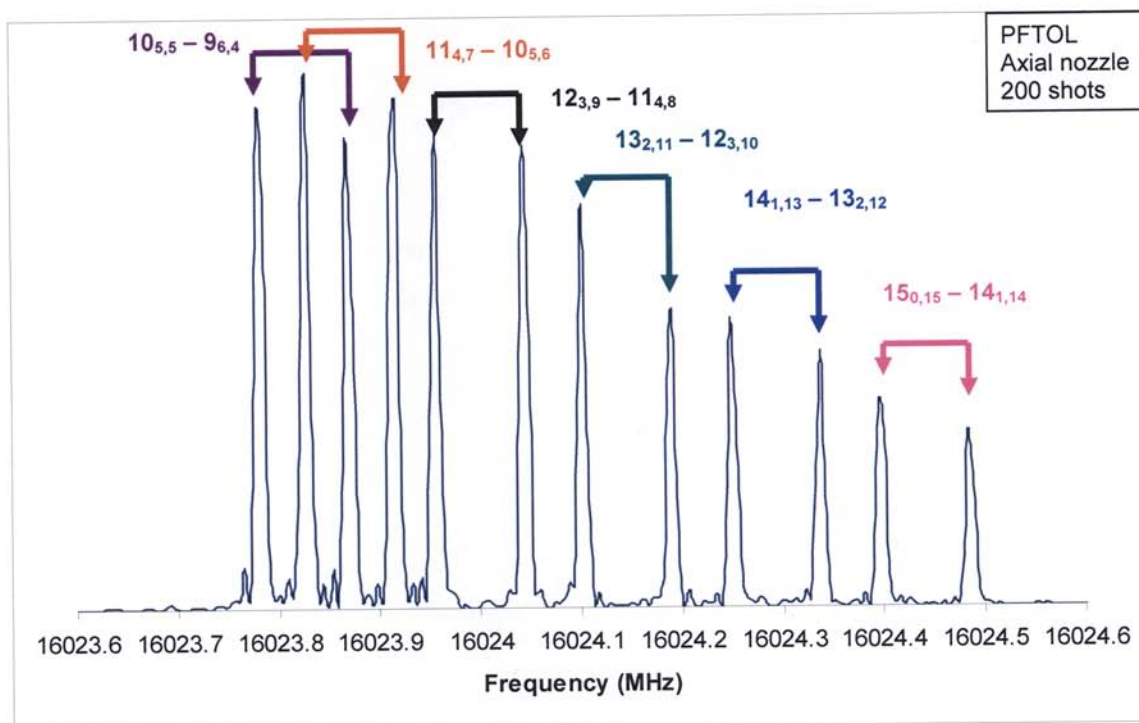


Figure 4.1: An example of transition grouping found in the rotational spectrum of pentafluorotoluene. Within this series, each ΔJ value is equal to +1. This pattern is indicative of an oblate molecule.

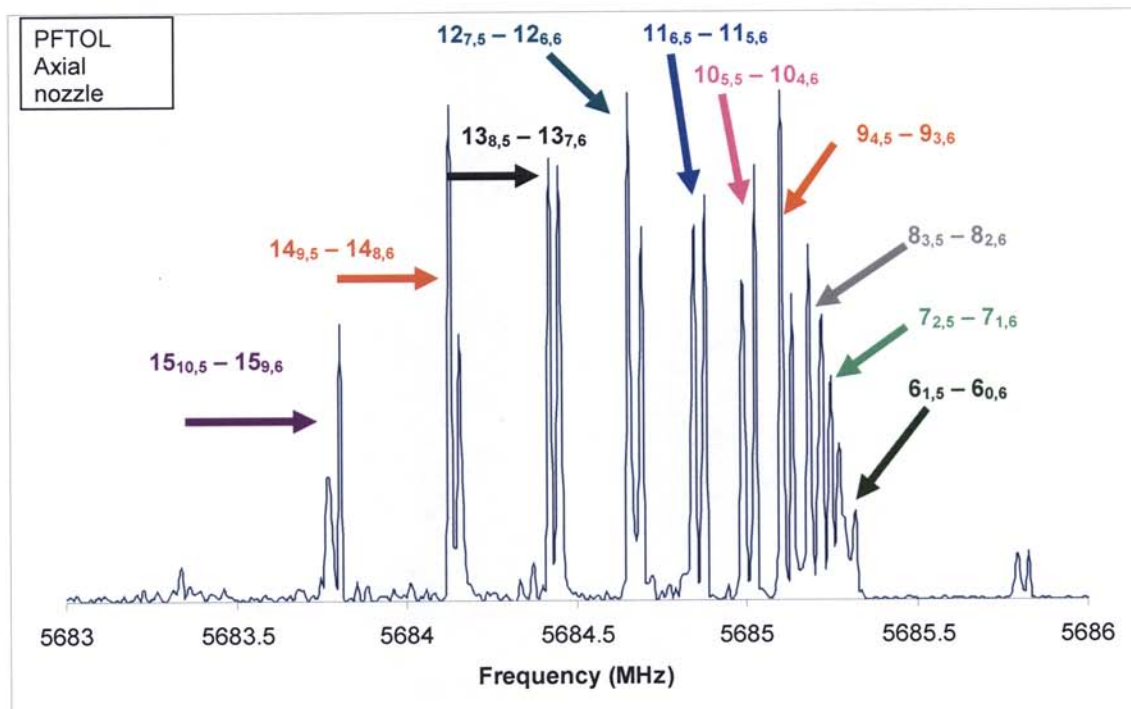
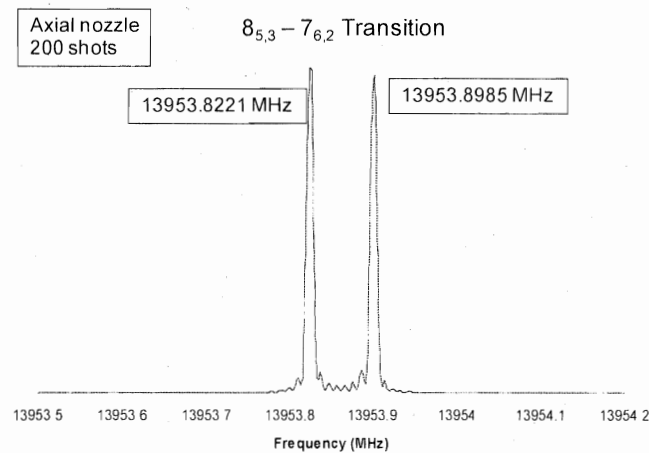


Figure 4.2: One portion of the Q-branch found in the rotational spectrum of pentafluorotoluene. Only once this branch was assigned were the distortion constants able to be determined.

Another observation that was made during the measurement of the rotational spectrum was evidence of internal rotation that was present in small splittings seen throughout the spectrum. An example of this splitting can be seen in Figure 4.3. The transition that is shown displays typical Doppler splitting in addition to the small splittings that were seen consistently throughout the spectrum. These small splittings were all present with a frequency difference of around 16 kHz. Further evidence of internal rotation was also seen through torsionally excited state transitions seen throughout the broadband spectrum. These can be seen in Figure 4.4. These all exhibited fast first-order Stark effects. This type of Stark effect is seen when the transition splits very rapidly

with only a small electric field applied. When typical second-order Stark effects are measured in dipole moment determinations, the voltage that was applied varied up to (+/-) 5000 V. The lines in the broadband spectrum split fast enough that they were unable to be measured with an applied voltage of only (+/-) 20 V. Also, while there are only four lines that displayed this type of Stark effect in Figure 4.4, these lines occurred consistently throughout the entire 11 GHz range.

(a)



(b)

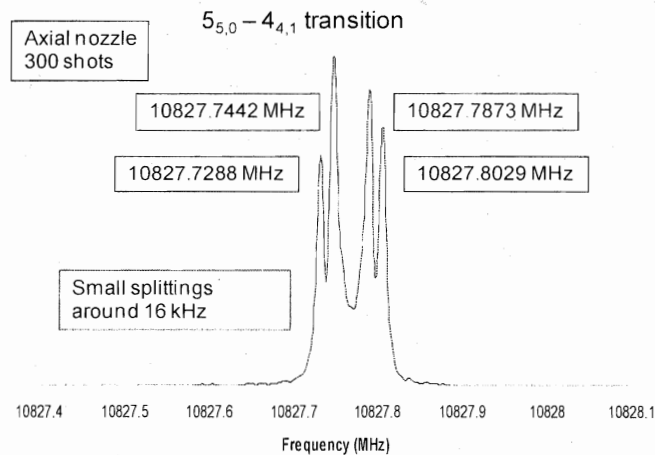


Figure 4.3: Example of transition splitting occurring throughout the spectrum. Transition (a) shows Doppler splitting characteristic of axial nozzle configuration. Transition (b) shows same splitting with additional small splitting of around 16 kHz due to internal rotation.

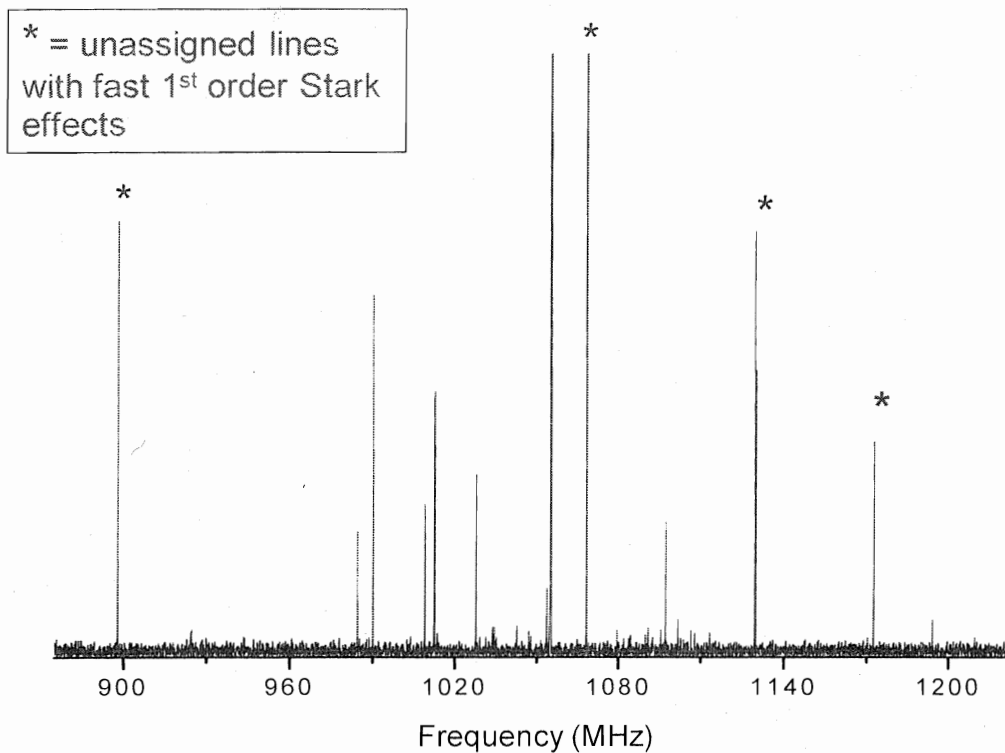


Figure 4.4: A portion of the broadband spectrum of PFTOL with torsionally excited states indicated. Frequency scale represents the frequency offset from the center frequency of 9800 MHz.

4.3 Results

The rotational spectrum for pentafluorotoluene was found to be a *b*-type spectrum. Results also indicated that pentafluorotoluene is an oblate-top near-symmetric rotor. The transitions that were measured using both the FTMW and broadband spectrometers can be seen in Table 4.1. These transitions were used in SPFIT^[5] in order to assign the spectrum as described in Chapter 2. The spectroscopic constants that were determined from this can be seen in Table 4.2.

Table 4.1: Measured transitions of the normal species of pentafluorotoluene

J'	K_a'	K_c'	J''	K_a''	K_c''	Exp. Freq. (MHz)	Calc. Freq. (MHz)	Error (MHz)
4	1	3	3	2	2	5685.8099	5685.8067	0.0032
5	0	5	4	1	4	5686.0541	5686.0551	-0.0010
3	3	1	2	2	0	5702.8038	5702.7952	0.0086
4	2	2	3	3	1	6701.9342	6701.9321	0.0021
3	3	0	2	2	1	6711.2382	6711.2340	0.0043
5	1	4	4	2	3	6719.7526	6719.7523	0.0003
6	0	6	5	1	5	6719.8955	6719.8958	-0.0003
4	3	2	3	2	1	6736.6672	6736.6606	0.0066
5	2	3	4	3	2	7753.1579	7753.1567	0.0012
6	1	5	5	2	4	7753.5883	7753.5903	-0.0020
7	0	7	6	1	6	7753.7340	7753.7362	-0.0022
5	3	3	4	2	2	7753.8655	7753.8633	0.0022
4	4	1	3	3	0	7781.5892	7781.5942	-0.0050
5	3	2	4	4	1	8757.2157	8757.2169	-0.0012
4	4	0	3	3	1	8770.7285	8770.7143	0.0142
6	3	4	5	2	3	8787.3004	8787.3065	-0.0061
7	1	6	6	2	5	8787.4333	8787.4287	0.0046
8	0	8	7	1	7	8787.5774	8787.5763	0.0011
5	4	2	4	3	1	8815.5567	8815.5624	-0.0057
4	3	1	3	2	2	9792.5479	9792.5332	0.0147
6	3	3	5	4	2	9820.3402	9820.3377	0.0025
7	2	5	6	3	4	9821.1305	9821.1303	0.0002
8	1	7	7	2	6	9821.2672	9821.2672	0.0001
9	0	9	8	1	8	9821.4122	9821.4159	-0.0037
6	4	3	5	3	2	9821.9917	9821.9902	0.0015
4	4	1	3	1	2	9849.4878	9849.4796	0.0082
5	5	1	4	4	0	9863.0615	9863.0573	0.0042
6	4	2	5	5	1	10808.9665	10808.9647	0.0019
5	5	0	4	4	1	10827.7659	10827.7605	0.0055
7	3	4	6	4	3	10854.8631	10854.8642	-0.0011
7	4	4	6	3	3	10854.8857	10854.8846	0.0011
8	2	6	7	3	5	10854.9645	10854.9638	0.0007
9	2	8	8	1	7	10855.1062	10855.1052	0.0010
10	0	10	9	1	9	10855.2520	10855.2550	-0.0030
6	5	2	5	4	1	10897.2913	10897.2926	-0.0013
7	4	3	6	5	2	11887.2708	11887.2714	-0.0006
8	3	5	7	4	4	11888.6779	11888.6798	-0.0019
9	2	7	8	3	6	11888.8015	11888.7988	0.0027
10	1	9	9	2	8	11888.9462	11888.9428	0.0034
11	0	11	10	1	10	11889.0923	11889.0936	-0.0013
7	5	3	6	4	2	11890.5808	11890.5842	-0.0034
5	5	1	4	2	2	11931.8446	11931.8395	0.0051
6	6	1	5	5	0	11947.0565	11947.0541	0.0024
7	5	2	6	6	1	12856.8902	12856.8901	0.0001
6	6	0	5	5	1	12882.5578	12882.5583	-0.0005

J'	K_a'	K_c'	J''	K_a''	K_c''	Exp. Freq. (MHz)	Calc. Freq. (MHz)	Error (MHz)
5	3	2	4	2	3	12920.6600	12920.6548	0.0052
5	4	2	4	1	3	12922.3000	12922.2889	0.0111
8	4	4	7	5	3	12922.4512	12922.4547	-0.0035
9	3	6	8	4	5	12922.5047	12922.5037	0.0010
10	3	8	9	3	7	12922.6370	12922.6340	0.0030
11	1	10	10	2	9	12922.7828	12922.7797	0.0031
12	0	12	11	1	11	12922.9294	12922.9317	-0.0023
7	6	2	6	5	1	12981.8300	12981.8368	-0.0068
8	5	3	7	6	2	13953.8603	13953.8633	-0.0030
9	4	5	8	5	4	13956.2422	13956.2449	-0.0027
10	3	7	9	4	6	13956.3342	13956.3329	0.0013
11	2	9	10	3	8	13956.4728	13956.4689	0.0039
12	1	11	11	2	10	13956.6192	13956.6159	0.0033
13	0	13	12	1	12	13956.7660	13956.7691	-0.0031
8	6	3	7	5	2	13959.8311	13959.8399	-0.0088
7	7	1	6	6	0	14033.4148	14033.4187	-0.0039
7	7	0	6	6	1	14935.3290	14935.3275	0.0015
10	4	6	9	5	5	14990.0481	14990.0519	-0.0038
9	5	4	8	6	3	14990.0716	14990.0801	-0.0085
11	3	8	10	4	7	14990.1656	14990.1638	0.0018
9	6	4	8	5	3	14990.1876	14990.1923	-0.0047
12	2	10	11	3	9	14990.3084	14990.3031	0.0053
13	1	12	12	2	11	14990.4558	14990.4514	0.0044
14	0	14	13	1	13	14990.6028	14990.6059	-0.0031
7	6	1	6	5	2	15944.9957	15944.9989	-0.0032
10	5	5	9	6	4	16023.8210	16023.8326	-0.0116
11	4	7	10	5	6	16023.8674	16023.8715	-0.0041
12	3	9	11	4	8	16023.9928	16023.9949	-0.0021
13	2	11	12	3	10	16024.1485	16024.1365	0.0120
14	1	13	13	2	12	16024.2898	16024.2861	0.0037
15	0	15	14	1	14	16024.4376	16024.4419	-0.0043
8	8	0	7	7	1	16986.3066	16986.3195	-0.0129
11	5	6	10	6	5	17057.6191	17057.6122	0.0069
12	4	8	11	5	7	17057.6929	17057.6959	-0.0030
13	3	10	12	4	9	17057.8292	17057.8257	0.0035
10	7	4	9	6	3	17057.9767	17057.9734	0.0033
15	1	14	14	2	13	17058.1237	17058.1199	0.0038
16	0	16	15	1	15	17058.2725	17058.2772	-0.0047
8	7	1	7	6	2	17990.4600	17990.4594	0.0006

Table 4.2: Spectroscopic constants of pentafluorotoluene. See Figure 4.5 for atom numbering

Parameter	Normal	¹³ C ₁	¹³ C ₂	¹³ C ₃	¹³ C ₆	¹³ C ₇	MP2
A (MHz)	1036.61221(15)	1036.0730(6)	1035.9359(6)	1032.0932(3)	1032.7466(3)	1030.9420(5)	1035.2031
B (MHz)	1030.94086(16)	1027.6045(6)	1027.6092(6)	1030.9721(3)	1030.9778(5)	1018.2450(2)	1021.4101
C (MHz)	516.92066(11)	515.94741(13)	515.91572(11)	515.80248(10)	515.96732(10)	512.31292(9)	515.7608
<i>I</i> _a (μ * Å ²)	487.5295(7)	487.7833(3)	487.8478(3)	489.66416(14)	489.3536(14)	490.2109(2)	---
<i>I</i> _b (μ * Å ²)	490.21149(8)	491.8031(3)	491.8008(3)	490.19663(14)	490.1939(2)	496.32363(10)	---
<i>I</i> _c (μ * Å ²)	977.6723(2)	979.5166(3)	979.5767(2)	979.79182(19)	979.47880(19)	986.46556(17)	---
<i>D</i> _J (Hz) ^a	19.9(16)	19.9	19.9	19.9	19.9	19.9	---
<i>D</i> _{JK} (Hz) ^a	-30.5(41)	-30.5	-30.5	-30.5	-30.5	-30.5	---
<i>D</i> _K (Hz) ^a	12.4(27)	12.4	12.4	12.4	12.4	12.4	---
<i>P</i> _{aa} (μ * Å ²) ^b	490.1772	491.7682	491.7649	490.1621	490.1592	496.2891	---
<i>P</i> _{bb} (μ * Å ²) ^b	487.4952	487.7484	487.8119	489.6297	489.3196	490.1764	---
<i>P</i> _{cc} (μ * Å ²) ^b	0.0343	0.0305	0.0359	0.0345	0.0347	0.0345	---
<i>N</i> ^c	84	13	16	16	16	17	---
Δv_{rms} (kHz) ^d	3.70	0.96	1.80	1.39	5.15	2.67	---
κ ^e	0.9782	0.9674	0.9680	0.9957	0.9932	0.9510	---

^a Centrifugal distortion constants for isotopologue species were fixed to the experimental values from the normal species.

^b For *P*_{aa}, *P*_{bb} and *P*_{cc} definitions, see text.

^c *N* is the number of transitions fitted.

^d $\Delta v_{rms} = [\sum (v_{obs} - v_{calc})^2 / N]^{1/2}$.

^e For κ definition, see text.

Determination of the rotational spectrum as a *b*-type spectrum can be seen in the transitions that have been measured. It is seen in Table 4.1 that ΔJ , ΔK_a and ΔK_c all equal 1, indicating a molecule whose dipole moment lies along the *b* axis. Indication of an oblate-top molecule can be seen from the rotational constants. From the results received from SPFIT, the *A* and *B* rotational constants are very similar. This along with κ values close to +1 and the groups of transitions that were seen in Figure 4.1, are all evidence of an oblate molecule. κ represents the asymmetry parameter of the molecule and is defined by Equation (4.3). These values can range from -1 for a prolate rotor to +1 for an oblate rotor,

with 0 indicating an asymmetric molecule^[4]. Due to this indication that the molecule was very near an oblate top, the spectra were fit using an S-reduction (for a symmetric rotor) in the III^L representation, rather than the I^R representation normally used for near-prolate tops. The centrifugal distortion constants were only determined for the normal species. When assigning the isotopologue spectra, these constants were fixed to the value for the normal species, or the non-substituted species. The high degree of uncertainty in the constants is due to the rigid nature of the aromatic ring. Any distortion of the structure that might be caused by centrifugal force on the molecule is very small because of strength of the bonds within the aromatic ring. Finally, the results in Table 4.2 show that all but one of the isotopologue spectra were determined with rms values at fewer than 5 kHz and the rotational constants are at better than 0.93% difference from *ab initio* predictions.

$$\kappa = (2B - A - C) / (A - C) \quad (4.3)$$

Once the spectrum was assigned and the spectroscopic constants were determined, work on determination of the molecular structure began. Two separate structures were determined using Kraitchman's equations^[6] and StrfitQ^[7] and compared to *ab initio* values. Kraitchman's programs KRA and EVAL were used to determine the r_s , or substitution, structure of the molecule^[8]. These programs use the differences in the moments of inertia between the normal species and an isotopically substituted species to determine the principal

axis coordinates of the substituted atom. StrfitQ was used to determine the r_0 , or inertial fit, structure of the molecule. This is determined by a least-squares routine where the various structural parameters are varied until the observed moments of inertia of all the measured isotopologues are reproduced. The principal axis coordinates that were determined using Kraitchman's equations^[6] can be found in Table 4.3. Both the r_s and r_0 structures are summarized in Table 4.4 with the atom numbering system present in Figure 4.5.

Two r_0 structures were determined for both PFTOL and CPF B. It was found that with these input structures difficulty arose in closing the aromatic ring during the fitting procedure. The effect was first observed in PFTOL but was believed, at the time, to be due to the structure of the molecule. When this effect was observed in CPF B as well, it was thought that the effect was due to the StrfitQ program rather than the molecule itself. A second r_0 structure was then obtained using an input structure with a flipped atom definition, meaning that the structural information was input in the program in the reverse order that was used for the first determination. The two atom orderings used for StrfitQ for CPF B are shown in Figure 4.6. It was found that the aromatic ring was again difficult to close using this second structure. Obtaining both r_0 structures gives an overall determination of the structure of both PFTOL and CPF B as the rest of the distances and angles agree well. Only the structure of the carbon atom framework was determined due to the inability of the fluorine atoms to be isotopically substituted, since they do not have an isotopic species which is

present in natural abundance. The results of these determinations will be discussed further in Chapter 6.

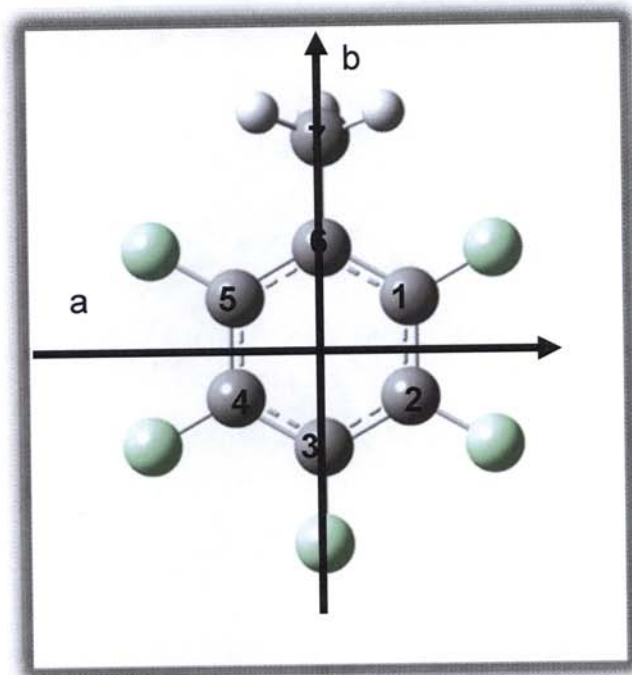


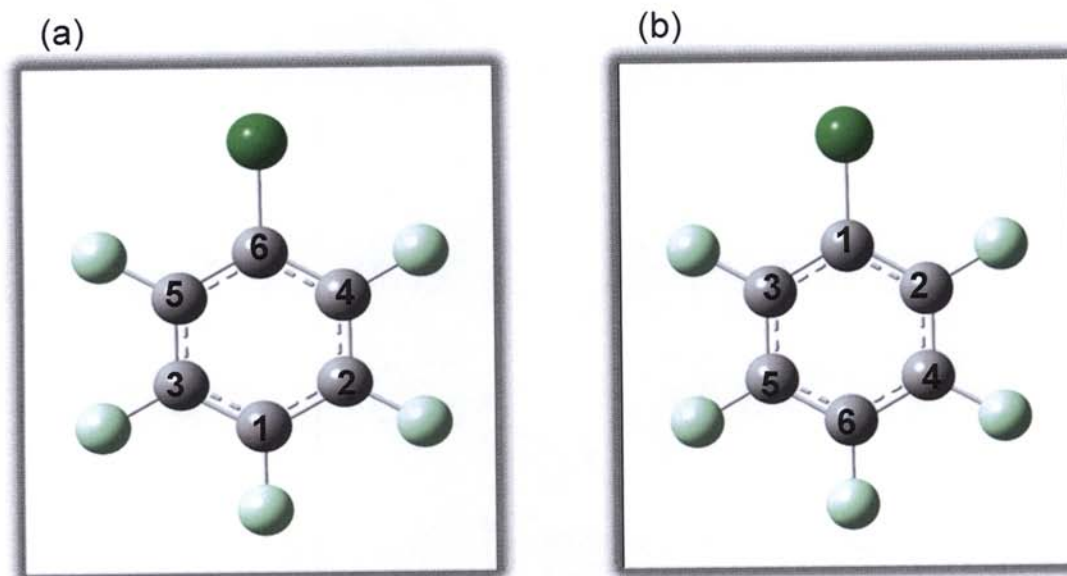
Figure 4.5: Structure of pentafluorotoluene

Table 4.3: Pentafluorotoluene principal axis coordinates (Å) of the carbon atom framework. See figure 4.5 for atom numbers.

^{13}C	a	(<i>ab initio</i>)	b	(<i>ab initio</i>)	c	(<i>ab initio</i>)
$^{13}\text{C}_1$	1.20166(11)	1.2024	0.6357(3)	0.6561	0.026(5)	0
$^{13}\text{C}_2$	1.18474(11)	1.1841	0.7118(3)	0.7333	0.029(4)	0
$^{13}\text{C}_3$	0.0555(3)	0	1.45840(7)	1.4651	0.017(5)	0
$^{13}\text{C}_6$	0.0759(4)	0	1.34759(9)	1.3537	0.02(6)	0
$^{13}\text{C}_7$	0.040(6)	0	2.96823(11)	2.9674	0.02(9)	0

Table 4.4: Bond distances and angles of pentafluorotoluene

Bond	1 st Inertial fit Distance (Å)	2 nd Inertial fit Distance (Å)	Kraitchman's fit Distance (Å)	ab initio Distance (Å)
C ₆ -C ₅	1.396(14)	1.395(13)	1.4004(19)	1.3901
C ₅ -C ₄	1.372(17)	1.354(12)	1.347(3)	1.3896
C ₄ -C ₃	1.406(17)	1.449(13)	1.3967(17)	1.3920
C ₇ -C ₆	1.504(12)	1.504(10)	1.5098(12)	1.5023
Angle	1 st Inertial fit Angle (°)	2 nd Inertial fit Angle (°)	Kraitchman's fit Angle (°)	ab initio Angle (°)
C ₁ -C ₂ -C ₃	120.2(12)	119.9(10)	119.9(3)	119.4
C ₆ -C ₁ -C ₂	122.6(12)	122.6(10)	122.9(4)	122.5
C ₇ -C ₆ -C ₁	---	122.1(4)	122.2(2)	121.7
C ₄ -C ₃ -C ₂	119.0(8)	---	118.7(2)	119.8
C ₅ -C ₆ -C ₁	---	115.8(8)	115.6(2)	119.8

**Figure 4.6:** StrfitQ input structures for CPFB. The first input structure is seen in (a) with the second input structure represented in (b). Both structures were needed due to complications with the program in closing the aromatic rings.

Additionally, Stark effect measurements were done on pentafluorotoluene to determine the dipole moment. The measurements on this molecule proved difficult to accomplish due to the varying speed at which the lines split. Most transitions that were measured split either too slowly or too quickly to determine accurately. Only two transitions were able to be measured with a reasonable error. From Table 4.5, it can be observed that the determined dipole moment values vary greatly, depending on which of the measured transitions are included in the fitting process. The fit that closely matches the *ab initio* value of 2.17 Debye is the fit from the entire $4_{4,0} - 3_{3,1}$ transition at 2.161(13) Debye. The current dipole moment determination, however, is 1.976(11) Debye from the fit which included every transition. The *ab initio* value is generally an overestimation, so 1.976 D is a reasonable value. The reason this is determined as the experimental dipole moment, is no current evidence is present which indicates one transition being more reliable than another. Future work needs to be done on this subject to try to determine the cause of the varying dipole moment values.

Finally the energy barrier to internal rotation, V_3 , was estimated using the measured P_{cc} value of PFTOL. The method that was used is described previously by work done by Herschbach^[9]. The *ab initio* predictions for both toluene and PFTOL of P_{cc} are around $1.5 \mu * \text{\AA}^2$, while the experimental observations of this value were close to zero. The lowering of the P_{cc} value for PFTOL as well as the large magnitude of the splitting in the lines showing first order Stark effects indicated that the energy barrier to internal rotation was most

likely small. The estimation took place by first determining the rigid-rotor rotational constants according to Equations (4.4) – (4.6) as described in reference [3].

Table 4.5: Dipole moment determinations of pentafluorotoluene. $J' - J''$ and M_J columns represent different combinations of transitions that were used to fit μ .

$J' - J''$	M_J	$\mu_{tot.}$ (Debye)
3 _{3,1} - 2 _{2,0}	0	2.00(3)
	1	1.99(4)
	0,1	1.99(2)
4 _{4,0} - 3 _{3,1}	0	2.199(12)
	1	2.132(6)
	2	2.07(2)
	0,1	2.161(13)
4 _{4,0} - 3 _{3,1}	0,1; 0,1	2.07(2)
3 _{3,1} - 2 _{2,0}		
	0,1,2; 0	1.976(11)

$$A_{00} = A_r + W_{00}^2 F \rho_a^2 \quad (4.4)$$

$$B_{00} = B_r + W_{00}^2 F \rho_b^2 \quad (4.5)$$

$$C_{00} = C_r \quad (4.6)$$

In these equations, A_{00} , B_{00} and C_{00} are experimental rotational constants with F being the reduced rotational constant of the methyl top and ρ being a direction cosine. Once the perturbation coefficient, W_{00}^2 is calculated using

these equations it can be used to find the reduced energy barrier, s , according to Appendix C of the work done by Herschbach^[9]. To find the particular s value that was needed, extrapolation past the values included in the appendix was done (Figure 4.7) which adds some uncertainty to the estimation. This reduced barrier is then used to determine V_3 according to Equation (4.7).

$$s = 4V_3 / 9F \quad (4.7)$$

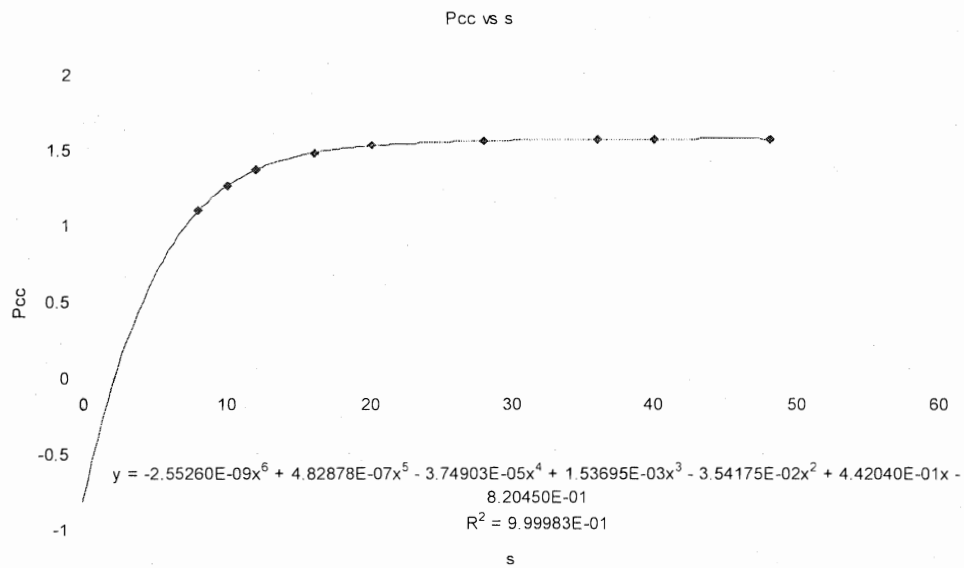


Figure 4.7^[9]: Plot used to extrapolate the reduced energy barrier, s , based on Appendix C of Herschbach. P_{cc} present in units of $(\mu * \text{\AA}^2)$.

A spreadsheet entitled Internal Rotation.xls was used to perform these calculations according to Equations (4.4) – (4.7). Calculations using the experimental P_{cc} value of PFTOL gave an energy barrier of $V_3 = 0.055$ kJ/mol. Assuming a reasonable uncertainty gives a rounded value of $V_3 = 0.1(2)$ kJ/mol. More on these results compared to literature values of similar molecules can be seen in Chapter 6.

Chapter 4: References

- [¹]Hollas, M.J. *Modern Spectroscopy*, 3rd ed. John Wiley & Sons: New York, NY 1996.
- [²]Program DIPOLE, Kuczkowski group, University of Michigan.
- [³]Serafin, M. M.; Peebles, S. A. *J. Chem. Phys. A*. **2008**, *112*, 12616 – 12621.
- [⁴]Serafin, M. M.; Peebles, S. A. *J. Chem. Phys. A*. **2008**, *112*, 1473 – 1479.
- [⁵]Pickett, H. M. *J. Mol. Spectrosc.* **1991**, *148*, 371.
- [⁶]Kraitchman, J. *Am. J. Phys.* **1953**, *21*, 17.
- [⁷]Schwendeman, R. H. In *Critical Evaluation of Chemical and Physical Structural Information*; Lide, D. R., Paul, M. A., Eds.; National Academy of Sciences: Washington, DC, 1974. The STRFITQ program used in this work is the University of Michigan modified version of Schwendeman's original code.
- [⁸]Kraitchman coordinates and propagated errors in parameters calculated using the KRA and EVAL code, Kisiel, Z. PROSPE–Programs for Rotational Spectroscopy; <http://info.ifpan.edu.pl/~kisiel/prospe.htm>, accessed July 2006.
- [⁹]Herschbach, D. R. *J. Chem. Phys.* **1959**, *31(1)*, 91 – 108.

Chapter 5: Microwave Spectroscopy of

Chloropentafluorobenzene

5.1 Introduction

After studying the rotational spectrum of PFTOL, there were still some observations that were unexplained. One of the most significant of these observations was structural distortion possibly caused by the presence of a methyl group or the large number of fluorine atoms around the ring. Substituting a methyl group with a chlorine atom should get rid of any internal rotation effects present as rotation around the C–Cl bond will not have any effect on the geometry of the molecule. For this reason, an experiment characterizing chloropentafluorobenzene, or CPFB, using microwave spectroscopy began. Another reason for the study of this molecule is structural comparisons between it and PFTOL. Characterization of the effect of the fluorine atoms was a main reason in the study of pentafluorotoluene. Comparison of this molecule to one with two different electronegative atoms, chlorine as well as fluorine, can possibly give a better understanding of the substituent effects.

While the rotational spectrum of CPFB will not have any effects from internal rotation, nuclear quadrupole coupling will occur. This type of effect is seen only in molecules that contain an atom with a quadrupolar nucleus. This type of atom is defined as having a nuclear spin quantum number of $I \geq 1$ with chlorine's spin quantum number equal to $3/2$ ^[1]. The angular momentum of the

nuclear spin will couple with the total angular momentum, J , to give the quantum number F . This coupling will cause the transition to split into hyperfine components, having values of $F = I+J, I+J-1, \dots, |I-J|$. The components with the highest intensities were commonly the $\Delta F = +1$ transitions. Measurement of these hyperfine components can be used to determine the nuclear quadrupole coupling constants χ_{aa} , χ_{bb} , and χ_{cc} . These constants can be used to determine the asymmetry parameter, η , which gives a measure of whether the electric field gradient is cylindrical around the C–Cl bond. Calculation of this parameter can be seen in Equation (5.1)^[1].

$$\eta = (\chi_{bb} - \chi_{cc}) / \chi_{aa} \quad (5.1)$$

Assignment of the chloropentafluorobenzene spectrum was done using the same process as pentafluorotoluene. The main difference in the measurement of this spectrum is that the majority of the assigned lines were found using the broadband spectrum collected at UVa. The transitions measured using the FTMW at EIU were done to support the initial assignment. Stark effect measurements were also done on this molecule using the FTMW spectrometer at EIU. Past measurements done on other molecules containing a quadrupolar chlorine atom were complicated by interactions of the nuclear quadrupole hyperfine structure with the Stark splittings^[2]. Chloropentafluorobenzene also proved to be a molecule for which Stark effect measurements were difficult. A detailed discussion of these difficulties can be found in section 5.3.

5.2 Measurement observations

Primarily broadband spectra were used to assign CPF. The acquisition of this spectrum was discussed in Chapter 2 and included two different acquisition procedures, one using a bandpass filter to improve the signal-to-noise ratio. A comparison of these two methods can be seen in Figure 5.1. This figure represents the same transition $6_{3,3} - 5_{3,2}$ from both measurements. The advantage of this bandpass filter can be seen by the decrease in the noise that is present. This improvement in the S/N ratio allowed for the observation of the ^{13}C spectra in natural abundance. This same transition from the $^{13}\text{C}_1$ spectrum can be seen by the inset in Figure 5.1.

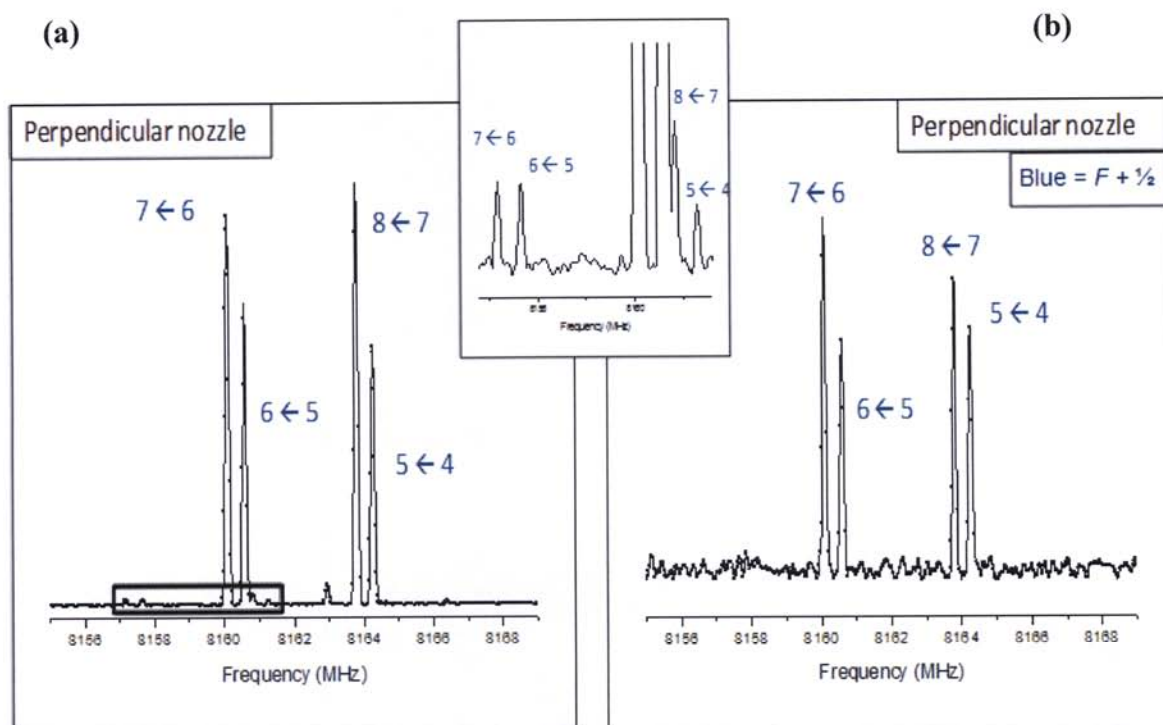


Figure 5.1: Comparison of broadband spectrum between (b) initial acquisition and (a) second acquisition with bandpass filter added. ^{13}C isotopologue lines are shown in the center inset and good measurement of these lines was a result of the improved S/N ratio.

The changes to the acquisition method in the narrower spectrum make a significant difference in the quality of the measurements. The microwave frequency chirp was lowered to 6.8 – 9 GHz before the filter was added (7 – 9 GHz with the filter). Also, three different nozzles were used in the acquisition of both spectra, but with the second acquisition, 8.4 million averages were taken rather than 320,000 averages used in the first spectrum. This increased the acquisition time to two days; however, the additional time was worthwhile since it is apparent that the adjustments in the second acquisition greatly increased the signal to noise ratio. The overall result of these changes can be seen in the improved spectrum in (b) of Figure 5.1.

Also seen in Figure 5.1 is evidence of the hyperfine structure due to the nuclear quadrupole moment of the chlorine atom. The $6_{3,3} - 5_{3,2}$ transition seen in the figure is fully resolved and was easily measured. Unfortunately, much of the hyperfine structure seen in this spectrum was unresolved. An example of these unresolved splittings can be seen in Figure 5.2. In this figure, only two of the hyperfine components were able to be assigned in the first transition as the other two were unresolved. Furthermore the second group of lines contains four components for each of two transitions which are overlapping. None of the components for either of these transitions were able to be assigned because of this overlap. Despite the many unresolved splittings, the spectrum for the normal species as well as the ^{37}Cl and all ^{13}C species were assigned as discussed below.

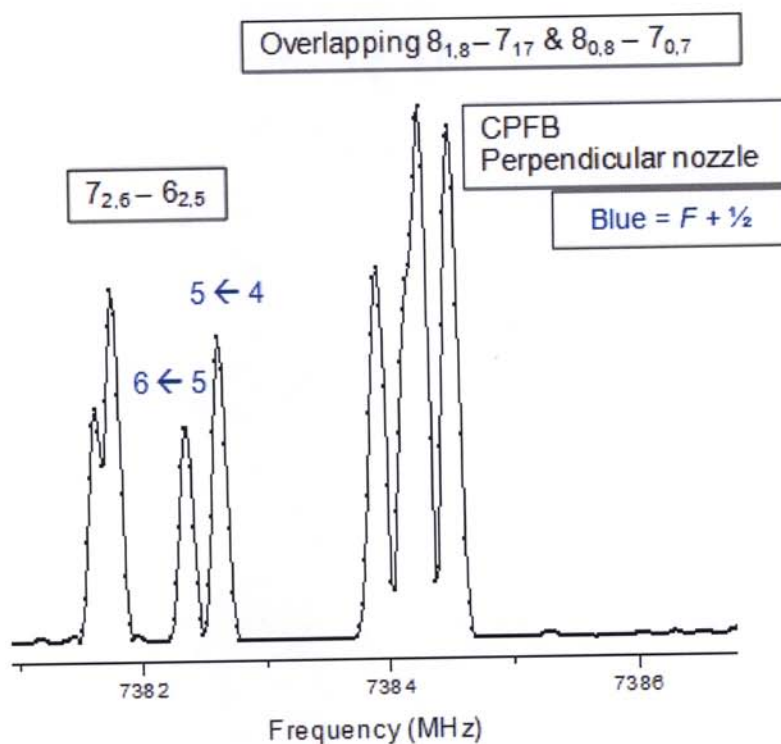


Figure 5.2: Unresolved hyperfine components due to nuclear quadrupole coupling in chloropentafluorobenzene.

5.3 Results

The spectrum for chloropentafluorobenzene was measured and included 217 components for the normal species. This was found to be an *a*-type spectrum with the most intense hyperfine components being those with $\Delta F = +1$. The measured transitions for this spectrum can be seen in Table 5.1. SPFIT^[3] was again used to assign the spectrum, and the resulting spectroscopic constants for CPF along with its isotopologues can be seen in Table 5.2.

Table 5.1: Measured transitions of the normal species of CPFb.

J'	K_a'	K_c'	$F + \frac{1}{2}'$	J''	K_a''	K_c''	$F + \frac{1}{2}''$	Exp. Freq. (MHz)	Calc. Freq (MHz)	Error (MHz)
5	2	3	5	4	2	2	4	6614.9712	6614.9726	-0.0014
5	2	3	6	4	2	2	5	6615.5061	6615.5054	0.0007
5	2	3	4	4	2	2	3	6615.9010	6615.8926	0.0084
5	2	3	7	4	2	2	6	6616.4494	6616.4467	0.0027
5	2	3	5	4	2	2	5	6619.0644	6619.0663	-0.0019
3	3	0	5	2	1	1	4	6696.7644	6696.7724	-0.0080
5	3	2	6	4	3	1	5	6747.7223	6747.7172	0.0051
5	3	2	5	4	3	1	4	6750.6433	6750.6382	0.0051
5	3	2	7	4	3	1	6	6757.6230	6757.6178	0.0052
5	3	2	4	4	3	1	3	6760.4601	6760.4562	0.0039
6	3	4	7	5	3	3	6	7200.1190	7200.1176	0.0014
6	3	4	6	5	3	3	5	7200.9274	7200.9250	0.0024
6	3	4	6	5	3	3	6	7201.7006	7201.7082	-0.0076
6	3	4	8	5	3	3	7	7204.0640	7204.0622	0.0018
6	3	4	5	5	3	3	4	7204.8485	7204.8483	0.0002
6	3	4	5	5	3	3	5	7207.8966	7207.8975	-0.0009
9	1	8	8	9	1	9	8	7325.2748	7325.2809	-0.0061
9	2	8	8	9	0	9	8	7325.5145	7325.5181	-0.0036
9	1	8	11	9	1	9	11	7325.7886	7325.7859	0.0027
9	2	8	11	9	0	9	11	7326.0285	7326.0242	0.0044
9	1	8	9	9	1	9	9	7328.4997	7328.4946	0.0052
9	2	8	9	9	0	9	9	7328.7262	7328.7359	-0.0097
9	1	8	10	9	1	9	10	7329.0414	7329.0430	-0.0016
9	2	8	10	9	0	9	10	7329.2815	7329.2846	-0.0031
7	2	6	8	6	2	5	8	7370.8175	7370.8188	-0.0013
7	2	6	6	6	2	5	5	7382.3594	7382.3570	0.0024
7	2	6	9	6	2	5	8	7382.6322	7382.6313	0.0009
7	1	6	8	6	1	5	8	7385.2935	7385.2982	-0.0047
7	1	6	7	6	1	5	6	7396.4230	7396.4213	0.0017
7	1	6	8	6	1	5	7	7396.6970	7396.6959	0.0011
7	1	6	6	6	1	5	5	7396.9029	7396.9029	0.0000
7	1	6	9	6	1	5	8	7397.1890	7397.1867	0.0023
7	1	6	7	6	1	5	7	7399.0970	7399.1030	-0.0060
7	1	6	6	6	1	5	6	7408.4272	7408.4219	0.0053
6	4	3	6	5	4	2	6	7532.0521	7532.0557	-0.0036
6	4	3	7	5	4	2	6	7532.2234	7532.2229	0.0005
6	4	3	5	5	4	2	5	7534.4526	7534.4523	0.0003
6	4	3	6	5	4	2	5	7534.8698	7534.8719	-0.0021
6	5	2	7	5	5	1	6	7540.1439	7540.1495	-0.0056
6	4	3	8	5	4	2	7	7541.4695	7541.4711	-0.0016
6	4	3	5	5	4	2	4	7544.0823	7544.0843	-0.0020
6	5	2	6	5	5	1	5	7545.1141	7545.1200	-0.0059
6	5	2	8	5	5	1	7	7555.6540	7555.6572	-0.0032
6	5	2	5	5	5	1	4	7560.6858	7560.6915	-0.0057
6	2	4	7	5	2	3	7	7567.1815	7567.1822	-0.0007
6	2	4	5	5	2	3	4	7577.5799	7577.5807	-0.0008

J'	K_a'	K_c'	$F + \frac{1}{2}'$	J''	K_a''	K_c''	$F + \frac{1}{2}''$	Exp. Freq. (MHz)	Calc. Freq. (MHz)	Error (MHz)
6	2	4	8	5	2	3	7	7578.4677	7578.4676	0.0001
6	2	4	6	5	2	3	5	7578.8892	7578.8890	0.0002
6	2	4	7	5	2	3	6	7579.7856	7579.7850	0.0006
6	5	1	7	5	5	0	6	7580.9797	7580.9865	-0.0068
6	2	4	6	5	2	3	6	7582.4484	7582.4498	-0.0014
6	5	1	6	5	5	0	5	7586.0775	7586.0848	-0.0073
6	2	4	5	5	2	3	5	7590.2508	7590.2525	-0.0017
3	3	1	5	2	1	2	4	7591.4178	7591.4191	-0.0013
6	5	1	8	5	5	0	7	7597.0375	7597.0442	-0.0067
6	5	1	5	5	5	0	4	7602.1952	7602.2025	-0.0073
3	3	1	3	2	1	2	2	7606.5746	7606.5721	0.0025
3	3	1	4	2	1	2	3	7624.3079	7624.3124	-0.0045
6	4	2	7	5	4	1	6	7918.8641	7918.8666	-0.0025
6	4	2	6	5	4	1	6	7919.7042	7919.7079	-0.0037
6	4	2	6	5	4	1	5	7922.0308	7922.0333	-0.0025
6	4	2	5	5	4	1	5	7925.7189	7925.7198	-0.0009
6	4	2	7	5	4	1	7	7926.8110	7926.8148	-0.0038
6	4	2	8	5	4	1	7	7930.4198	7930.4207	-0.0009
6	4	2	5	5	4	1	4	7933.4222	7933.4236	-0.0014
4	3	1	3	3	1	2	2	8034.2210	8034.2238	-0.0028
4	3	1	6	3	1	2	5	8041.0060	8041.0053	0.0007
4	3	1	5	3	1	2	5	8042.4809	8042.4834	-0.0025
4	3	1	3	3	1	2	3	8047.8079	8047.8055	0.0024
4	3	1	4	3	1	2	3	8049.0973	8049.1008	-0.0035
4	3	1	4	3	1	2	4	8055.4367	8055.4408	-0.0041
4	3	1	5	3	1	2	4	8055.9947	8055.9981	-0.0034
11	2	9	11	11	2	10	11	8127.9232	8127.9290	-0.0058
11	2	9	12	11	2	10	12	8128.2195	8128.2283	-0.0088
11	3	9	11	11	1	10	11	8128.4124	8128.4080	0.0044
6	3	3	7	5	3	2	6	8160.0844	8160.0842	0.0002
6	3	3	6	5	3	2	5	8160.5875	8160.5871	0.0004
6	3	3	6	5	3	2	6	8162.9526	8162.9508	0.0018
6	3	3	8	5	3	2	7	8163.7899	8163.7900	-0.0001
6	3	3	5	5	3	2	4	8164.2553	8164.2557	-0.0004
6	3	3	5	5	3	2	5	8172.7729	8172.7784	-0.0055
7	3	5	8	6	3	4	8	8180.1386	8180.1384	0.0002
8	2	7	9	7	2	6	9	8242.3471	8242.3446	0.0025
8	2	7	8	7	2	6	7	8253.9606	8253.9622	-0.0016
8	2	7	9	7	2	6	8	8254.1563	8254.1572	-0.0009
8	2	7	7	7	2	6	6	8254.5621	8254.5640	-0.0019
8	2	7	10	7	2	6	9	8254.7411	8254.7411	0.0000
8	2	7	8	7	2	6	8	8256.3609	8256.3631	-0.0022
8	1	7	8	7	1	6	7	8257.6784	8257.6786	-0.0002
8	1	7	9	7	1	6	8	8257.8773	8257.8780	-0.0007
8	1	7	7	7	1	6	6	8258.1914	8258.1943	-0.0029
8	1	7	10	7	1	6	9	8258.4016	8258.4028	-0.0012
8	1	7	8	7	1	6	8	8260.0825	8260.0856	-0.0031
8	2	7	7	7	2	6	7	8266.4558	8266.4578	-0.0020

J'	K_a'	K_c'	$F + \frac{1}{2}'$	J''	K_a''	K_c''	$F + \frac{1}{2}''$	Exp. Freq. (MHz)	Calc. Freq. (MHz)	Error (MHz)
8	1	7	7	7	1	6	7	8270.1928	8270.1948	-0.0020
7	2	5	8	6	2	4	8	8372.9537	8372.9562	-0.0025
7	2	5	6	6	2	4	5	8382.6402	8382.6415	-0.0013
7	2	5	9	6	2	4	8	8383.2172	8383.2180	-0.0008
7	2	5	7	6	2	4	6	8383.6549	8383.6559	-0.0010
7	2	5	8	6	2	4	7	8384.2413	8384.2416	-0.0003
7	2	5	7	6	2	4	7	8386.3185	8386.3207	-0.0022
7	2	5	6	6	2	4	6	8394.0037	8394.0049	-0.0012
4	2	2	3	3	0	3	2	8426.2599	8426.2640	-0.0041
4	2	2	5	3	0	3	4	8432.0147	8432.0190	-0.0043
7	4	4	8	6	4	3	7	8721.6704	8721.6731	-0.0027
7	4	4	8	6	4	3	8	8722.2256	8722.2273	-0.0017
7	4	4	7	6	4	3	6	8722.7206	8722.7235	-0.0029
7	4	4	9	6	4	3	8	8726.6936	8726.6961	-0.0025
7	4	4	6	6	4	3	6	8727.2977	8727.3045	-0.0068
7	4	4	6	6	4	3	5	8727.7204	8727.7241	-0.0037
7	6	2	8	6	6	1	7	8794.2145	8794.2237	-0.0092
7	6	2	7	6	6	1	6	8798.0532	8798.0633	-0.0101
7	6	1	8	6	6	0	7	8806.7314	8806.7446	-0.0132
7	6	2	9	6	6	1	8	8808.2547	8808.2644	-0.0097
7	6	1	7	6	6	0	6	8810.6003	8810.6177	-0.0174
7	6	2	6	6	6	1	5	8812.1504	8812.1595	-0.0091
7	6	1	9	6	6	0	8	8820.9393	8820.9507	-0.0114
7	6	1	6	6	6	0	5	8824.8645	8824.8786	-0.0141
7	5	3	7	6	5	2	7	8861.1618	8861.1724	-0.0106
7	5	3	8	6	5	2	7	8861.9890	8861.9956	-0.0066
7	5	3	7	6	5	2	6	8864.3839	8864.3905	-0.0066
7	5	3	9	6	5	2	8	8871.5465	8871.5506	-0.0041
7	5	3	6	6	5	2	5	8873.9194	8873.9266	-0.0072
7	5	2	8	6	5	1	7	9044.3144	9044.3117	0.0027
7	5	2	7	6	5	1	6	9047.0024	9046.9932	0.0092
7	5	2	9	6	5	1	8	9055.3703	9055.3624	0.0080
7	5	2	6	6	5	1	5	9058.0179	9058.0183	-0.0004
9	2	8	9	8	2	7	8	9123.0750	9123.0728	0.0022
9	2	8	10	8	2	7	9	9123.2374	9123.2353	0.0021
9	2	8	8	8	2	7	7	9123.5548	9123.5515	0.0033
9	2	8	11	8	2	7	10	9123.7251	9123.7188	0.0063
9	1	8	9	8	1	7	8	9123.9333	9123.9348	-0.0015
9	1	8	10	8	1	7	9	9124.1004	9124.0987	0.0017
9	1	8	8	8	1	7	7	9124.3913	9124.3969	-0.0056
9	1	8	11	8	1	7	10	9124.5718	9124.5688	0.0030
8	2	6	7	7	2	5	6	9181.3472	9181.3579	-0.0107
8	2	6	8	7	2	5	7	9181.4795	9181.4602	0.0193
8	2	6	10	7	2	5	9	9181.6272	9181.6325	-0.0053
8	2	6	9	7	2	5	8	9181.7526	9181.7345	0.0182
7	3	4	7	6	3	3	6	9345.1262	9345.1236	0.0026
7	3	4	6	6	3	3	5	9345.3183	9345.3129	0.0054
7	3	4	8	6	3	3	7	9345.4878	9345.4800	0.0078

J'	K_a'	K_c'	$F + \frac{1}{2}'$	J''	K_a''	K_c''	$F + \frac{1}{2}''$	Exp. Freq. (MHz)	Calc. Freq. (MHz)	Error (MHz)
7	3	4	9	6	3	3	8	9345.6848	9345.6779	0.0069
7	4	3	8	6	4	2	7	9494.3670	9494.3623	0.0047
7	4	3	7	6	4	2	6	9495.5623	9495.5484	0.0139
7	4	3	9	6	4	2	8	9500.7541	9500.7455	0.0086
7	4	3	6	6	4	2	5	9501.9249	9501.9155	0.0094
8	4	5	9	7	4	4	8	9810.0781	9810.0722	0.0059
8	4	5	8	7	4	4	7	9810.4477	9810.4389	0.0088
8	4	5	10	7	4	4	9	9812.7006	9812.6977	0.0029
8	4	5	7	7	4	4	6	9813.0517	9813.0439	0.0078
5	3	2	4	4	1	3	3	9904.3470	9904.3473	-0.0003
5	3	2	7	4	1	3	6	9906.2871	9906.2920	-0.0049
5	3	2	5	4	1	3	4	9908.1771	9908.1782	-0.0011
5	3	2	6	4	1	3	5	9910.1305	9910.1233	0.0072
8	7	2	10	7	7	1	9	10053.7538	10053.7583	-0.0045
8	6	3	9	7	6	2	8	10139.6933	10139.6992	-0.0059
8	6	3	8	7	6	2	7	10141.8018	10141.7981	0.0037
8	5	4	9	7	5	3	8	10143.1317	10143.1329	-0.0012
8	6	3	7	7	6	2	6	10151.2172	10151.2225	-0.0053
8	6	2	9	7	6	1	8	10209.6335	10209.6465	-0.0130
8	6	2	8	7	6	1	7	10211.8632	10211.8566	0.0066
8	6	2	10	7	6	1	9	10219.7329	10219.7216	0.0113
8	6	2	7	7	6	1	6	10221.9272	10221.9220	0.0052
8	3	5	7	7	3	4	6	10267.8829	10267.8744	0.0085
8	3	5	10	7	3	4	9	10268.4220	10268.4279	-0.0059
8	3	5	8	7	3	4	7	10269.2706	10269.2655	0.0051
8	3	5	9	7	3	4	8	10269.8147	10269.8251	-0.0104
5	4	1	4	4	2	2	3	10448.0267	10448.0196	0.0071
5	4	1	7	4	2	2	6	10454.2841	10454.2847	-0.0006
5	4	1	5	4	2	2	4	10467.4698	10467.4753	-0.0055
5	4	1	6	4	2	2	5	10473.8861	10473.8943	-0.0082
8	5	3	8	7	5	2	7	10645.0533	10645.0381	0.0152
8	5	3	10	7	5	2	9	10651.5128	10651.5112	0.0017
8	5	3	7	7	5	2	6	10652.9726	10652.9621	0.0105
8	4	4	9	7	4	3	8	10917.7501	10917.7529	-0.0028
8	4	4	8	7	4	3	7	10917.9689	10917.9493	0.0196
8	4	4	10	7	4	3	9	10920.1959	10920.1941	0.0018
8	4	4	7	7	4	3	6	10920.3855	10920.3724	0.0131
9	3	6	8	8	3	5	7	11039.5030	11039.5064	-0.0034
9	3	6	11	8	3	5	10	11039.8976	11039.8884	0.0092
9	3	6	9	8	3	5	8	11040.5863	11040.5789	0.0074
9	3	6	10	8	3	5	9	11040.9677	11040.9664	0.0013
9	5	5	10	8	5	4	9	11341.1455	11341.1560	-0.0105
9	5	5	9	8	5	4	8	11341.6970	11341.6784	0.0186
9	5	5	11	8	5	4	10	11344.6236	11344.6206	0.0030
9	5	5	8	8	5	4	7	11345.1374	11345.1224	0.0150
9	7	3	10	8	7	2	9	11391.8052	11391.8232	-0.0180
9	7	3	11	8	7	2	10	11400.9083	11400.8908	0.0175
9	7	2	11	8	7	1	10	11424.5964	11424.6137	-0.0173

J'	K_a'	K_c'	$F + \frac{1}{2}'$	J''	K_a''	K_c''	$F + \frac{1}{2}''$	Exp. Freq. (MHz)	Calc. Freq (MHz)	Error (MHz)
9	6	4	10	8	6	3	9	11479.5387	11479.5436	-0.0049
9	6	4	9	8	6	3	8	11480.7069	11480.7082	-0.0013
9	6	4	11	8	6	3	10	11485.9640	11485.9573	0.0067
9	6	4	8	8	6	3	7	11487.1132	11487.1126	0.0006
9	6	3	10	8	6	2	9	11731.8234	11731.8123	0.0111
9	6	3	11	8	6	2	10	11739.7343	11739.7256	0.0087
5	4	2	7	4	2	3	6	11758.9678	11758.9515	0.0163
6	4	2	5	5	2	3	4	11765.5575	11765.5506	0.0069
6	4	2	8	5	2	3	7	11768.2736	11768.2586	0.0150
6	4	2	6	5	2	3	5	11774.5348	11774.5359	-0.0011
6	4	2	7	5	2	3	6	11777.2714	11777.2555	0.0159
9	5	4	10	8	5	3	9	12256.2398	12256.2361	0.0037
9	5	4	9	8	5	3	8	12256.8951	12256.8933	0.0018
10	6	5	11	9	6	4	10	12771.6176	12771.6218	-0.0042
10	6	5	10	9	6	4	9	12772.2427	12772.2486	-0.0059
10	6	5	9	9	6	4	8	12776.4623	12776.4482	0.0141
10	4	6	9	9	4	5	8	12959.6770	12959.6788	-0.0018
10	4	6	12	9	4	5	11	12960.0669	12960.0748	-0.0079
10	4	6	10	9	4	5	9	12961.1075	12961.1140	-0.0065
10	4	6	11	9	4	5	10	12961.5172	12961.5149	0.0023
10	6	4	11	9	6	3	10	13387.7324	13387.7354	-0.0030
10	6	4	10	9	6	3	9	13388.6014	13388.6046	-0.0032
10	6	4	12	9	6	3	11	13393.8782	13393.8694	0.0088
11	4	7	10	10	4	6	9	13698.9562	13698.9616	-0.0054
11	4	7	13	10	4	6	12	13699.2410	13699.2429	-0.0019
11	4	7	12	10	4	6	11	13700.3387	13700.3426	-0.0039
11	6	6	12	10	6	5	11	13974.2768	13974.2905	-0.0137
11	6	6	13	10	6	5	12	13976.8646	13976.8656	-0.0010
12	4	8	14	11	4	7	13	14457.3226	14457.3177	0.0049
11	5	6	13	10	5	5	12	14812.2368	14812.2381	-0.0013
11	5	6	11	10	5	5	10	14812.4919	14812.4953	-0.0034
11	5	6	12	10	5	5	11	14812.7101	14812.7208	-0.0107

Table 5.2: Spectroscopic constants determined for chloropentafluorobenzene. See Figure 5.3 for atom numbering

Parameter	Normal	³⁷ Cl	¹³ C ₁	¹³ C ₂	¹³ C ₃	¹³ C ₆	MP2
A (MHz)	1028.5412(2)	1028.5439(7)	1025.5716(19)	1025.5627(19)	1028.5783(19)	1028.568(2)	1025.3533
B (MHz)	751.82072(17)	734.47954(18)	751.6505(4)	750.7696(4)	748.7217(4)	750.4372(4)	748.288383
C (MHz)	434.3531(3)	428.5081(2)	433.7654(4)	433.4701(4)	433.3233(4)	433.8980(5)	432.590173
D _J (Hz) ^a	3.8(10)	3.8	3.8	3.8	3.8	3.8	3.8
D _K (Hz) ^a	3.4(9)	3.4	3.4	3.4	3.4	3.4	3.4
3/2χ _{aa} (MHz)	-119.278(16)	-94.00(3)	-119.17(8)	-119.15(8)	-119.26(10)	-119.5(8)	-112.9410
1/4χ _{bb-cc} (MHz)	1.918(5)	1.53(2)	1.92(3)	1.94(3)	1.92(3)	1.91(3)	1.9430
χ _{aa} (MHz)	-79.52(2)	-62.67(2)	-79.45(5)	-79.43(5)	-79.51(7)	-79.7(5)	-75.2940
χ _{bb} (MHz)	43.6(1)	34.39(1)	43.56(3)	43.60(3)	43.59(3)	43.7(2)	41.5331
χ _{cc} (MHz)	35.92(2)	28.27(4)	35.89(9)	35.84(9)	35.91(9)	36.0(3)	33.7609
I _a (μ * Å ²)	491.35520(11)	491.3539(3)	492.7779(9)	492.7822(9)	491.3375(9)	491.3425(11)	--
I _b (μ * Å ²)	672.20686(16)	688.07778(17)	672.3591(4)	673.1480(4)	674.9892(4)	673.4462(4)	--
I _c (μ * Å ²)	1163.5213(8)	1179.3921(6)	1165.0977(11)	1165.8914(11)	1166.2864(11)	1164.7416(13)	--
P _{aa} (μ * Å ³) ^b	672.1865	688.0580	672.3394	673.1286	674.9690	673.4226	--
P _{bb} (μ * Å ³) ^b	491.3348	491.3341	492.7582	492.7628	491.3173	491.3190	--
P _{cc} (μ * Å ³) ^b	0.0204	0.0198	0.0197	0.0194	0.0202	0.0235	--
κ ^c	0.0686	0.0198	0.0743	0.0718	0.0597	0.0646	--
η (MHz) ^d	-0.0966	-0.0976	-0.0965	-0.0977	-0.0966	-0.0966	0.1032
N ^e	217	87	45	36	33	31	--
Δv _{rms} (kHz) ^f	6.1	5.5	4.9	4.1	5	4.8	--

^a Centrifugal distortion constants for isotopologue species were fixed to the experimental values from the normal species.

^b For P_{aa}, P_{bb} and P_{cc} definitions, see Chapter 4.

^c For κ definition, see Chapter 4.

^d For η definition, see text.

^e N is the number of transitions fitted.

^f Δv_{rms} = [Σ(v_{obs} - v_{calc})² / N]^{1/2}.

The *a*-type spectrum characteristic becomes apparent when looking at the transitions in Table 5.1. It can be seen that all of these transitions show a ΔK_a value of zero, indicating that the dipole moment of the molecule lies along the *a*-axis. According to the determined spectroscopic constants, CPF₅B appears to be a very asymmetric top. This is evident from the *A*, *B* and *C* rotational constants all displaying very different values as well as the κ value of around zero. Despite

the asymmetric top nature of CPF_B, the spectrum was assigned using an S-reduction in the I' representation, with the S standing for symmetric reduction. Both A- (asymmetric) and S-reductions were attempted with no significant difference observed in the rotational constants. The S-reduction remained in order to maintain as many similarities between the assignments for CPF_B and PFTOL as possible.

Of the isotopologue spectra, one noticeable difference is the number of transitions that were able to be measured. All of the ¹³C spectra were assigned, but this was done using only between 31 and 45 measured transitions. The ³⁷Cl spectrum, however, contains 87 transitions that were at a high enough intensity that they were able to be measured. This is due to the ³⁷Cl isotopologue being present in 25% natural abundance whereas the ¹³C isotopologue is present at 1% natural abundance. It can be seen in Table 5.2 that the rotational and nuclear quadrupole coupling constants were determined with low uncertainty and agree with the MP2 predictions to within 0.41%. Only the centrifugal distortion constants were determined with a high degree of uncertainty. Due to the rigid nature of the molecule, these were only able to be determined for the normal species, for which a much larger data set was available. When assigning the isotopologue spectra these constants were fixed to the same value that was determined for the normal species.

Once the spectra were successfully assigned, again the structure was determined using Kisiel's KRA and EVAL programs^[4] for the r_s structure and StrfitQ^[5] for the r_0 structure. Also, there are again, two separate r_0 structures for

the molecule, due to difficulty in using StrfitQ for both this molecule as well as PFTOL, as explained in Chapter 4. The atom numbering used in the data tables can be seen in Figure 5.3. The principal axis coordinates that were determined from CPFEB can be seen in Table 5.3. The distances and angles that were determined for the carbon atom framework and chlorine atom of CPFEB can be found in Table 5.4.

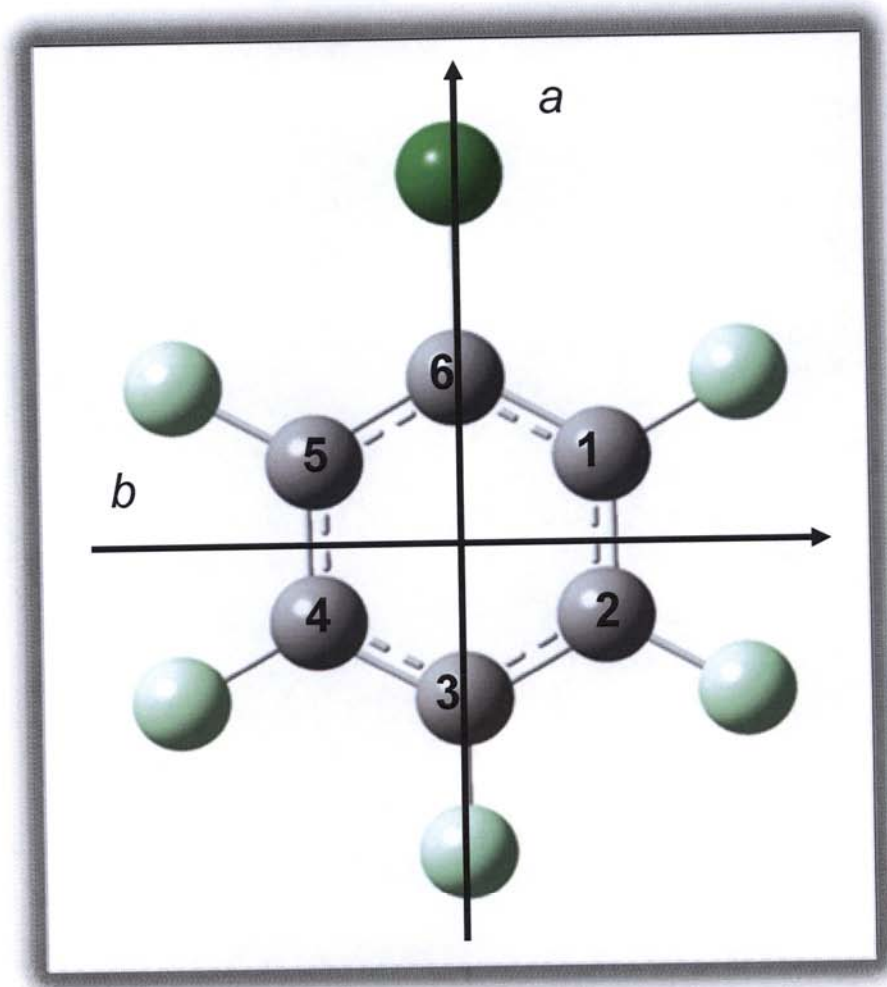


Figure 5.3: Structure and axes of chloropentafluorobenzene.

Table 5.3: Principal axis coordinates (Å) for the carbon atom framework of CPF₆. (italic values represent *ab initio* calculations)

¹³ C	<i>a</i>	<i>b</i>	<i>c</i>
¹³ C ₁	0.390(4), (-0.04127)	1.1945(13), (-1.1985)	0.027i(57), (0)
¹³ C ₂	0.9676(16), (-0.9769)	1.1991(13), (-1.2033)	0.0321i(49), (0)
¹³ C ₃	1.6695(9), (1.6732)	0.133i(12), (0)	0.017i(94), (0)
¹³ C ₆	1.1128(14), (-1.1234)	0.126i(13), (0)	0.056(28), (0)
³⁷ Cl	2.8331(5), (-2.8440)	0.020i(77), (0)	0.018i(86), (0)

Table 5.4: Bond distances and angles determined for CPF₆.

Bond	1st Inertial fit Distance (Å)	2nd Inertial fit Distance (Å)	Kraitichman fit Distance (Å)	<i>ab initio</i> Distance (Å)
C ₂ -C ₃	1.392(5)	1.392(5)	1.3894(15)	1.3903
C ₁ -C ₂	1.383(5)	1.383(4)	1.357(4)	1.3896
C ₆ -C ₁	1.391(8)	1.389(3)	1.397(3)	1.3934
Cl-C ₆	--	1.716(5)	1.7212(18)	1.7206
Angle	1st Inertial fit Angle (°)	2nd Inertial fit Angle (°)	Kraitichman fit Angle (°)	<i>ab initio</i> Angle (°)
C ₂ -C ₃ -F ₁	120.20(15)	--	120.2(4)	120.0579
C ₂ -C ₃ -C ₄	119.0(4)	--	119.3(2)	119.9
C ₁ -C ₂ -C ₃	119.8(3)	120.1(3)	120.2(4)	119.9
C ₆ -C ₅ -C ₄	121.0(3)	120.7(3)	121.3(4)	120.9
C ₅ -C ₆ -C ₁	--	116.6(3)	117.5(3)	119.9
Cl-C ₆ -C ₁	--	120.5(2)	121.0(3)	120.665

Finally, dipole moment determinations were attempted using Stark effect measurements for CPF₆ in the same method as PFTOL. Difficulties arose when measuring Stark effects for CPF₆ similar to the ones that arose when determining the dipole for PFTOL. The transitions for this molecule were already weak when measured using the FTMW at EIU. Stark effect measurements on CPF₆ made these transitions even less intense, complicating dipole moment

determinations. The transitions that were intense enough for Stark effect measurements seemed to either move slowly or too rapidly for accurate determination. Currently, one CPF_B transition has been measured at a rate that was easy to determine. The $4_{2,2} - 3_{2,1}; M_J = 0$ transition has been fit using the QStark program^[6] and gives a dipole moment of 0.401(15) Debye, within agreement of the predicted MP2 value of 0.415 Debye. Some future work needs to be done to further determine the dipole moment of this molecule. The results presented above were used to compare the structures of PFTOL and CPF_B to those of chlorobenzene, pentafluorobenzene and toluene. The experimental results of PFTOL can be seen in Chapter 4, whereas comparison of these results to literature values of similar molecules can be seen in Chapter 6.

References: Chapter 5

- [1] Peebles, S. A.; Peebles, R. A. *J. Mol. Struc.* **2003**, 657, 107 – 116.
- [2] Peebles, S. A.; Peebles, R. A. *J. Mol. Struc.* **2002**, 607, 19 – 29.
- [3] Pickett, H. M. *J. Mol. Spectrosc.* **1991**, 148, 371.
- [4] Kraitchman coordinates and propagated errors in parameters calculated using the KRA and EVAL code, Kisiel, Z. PROSPE–Programs for Rotational Spectroscopy; <http://info.ifpan.edu.pl/~kisiel/prospe.htm>, accessed July 2006.
- [5] Schwendeman, R. H. In *Critical Evaluation of Chemical and Physical Structural Information*; Lide, D. R., Paul, M. A., Eds.; National Academy of Sciences: Washington, DC, 1974. The STRFITQ program used in this work is the University of Michigan modified version of Schwendeman's original code.
- [6] Kisiel, Z.; Kosarzewski, J.; Pietrewicz, B. A.; Pyszczółkowski, L. *Chem. Phys. Lett.* **2000**, 325, 523.

Chapter 6: Discussion and Conclusions

6.1 Discussion of structural results

The microwave spectroscopy studies were started to determine the structure of pentafluorotoluene, the precursor to the pentafluorobenzyl radical. Observing this radical is the goal of the emission spectrometer that has been built to optimize the pulsed discharge nozzle, which will ultimately be used for IR spectroscopy as discussed in Chapter 3. The characterization of PFTOL led to a second microwave study on chloropentafluorobenzene in order to compare the two molecules, which would lead to a better understanding of some of the internal rotation effects that were seen in PFTOL. These two molecules were also compared to similar molecules that had already been characterized: chlorobenzene^[1] and toluene^[2]. Before comparisons were made, *ab initio* structure optimizations were done using Gaussian 03^[3] at the MP2 level with a 6-311++G(2d,2p) basis set. These calculations were done on PFTOL and CPFB as well as chlorobenzene, pentafluorobenzene, toluene and xylene. Evaluations were first done on the experimental and *ab initio* results of PFTOL and CPFB which can be seen in Figure 6.1.

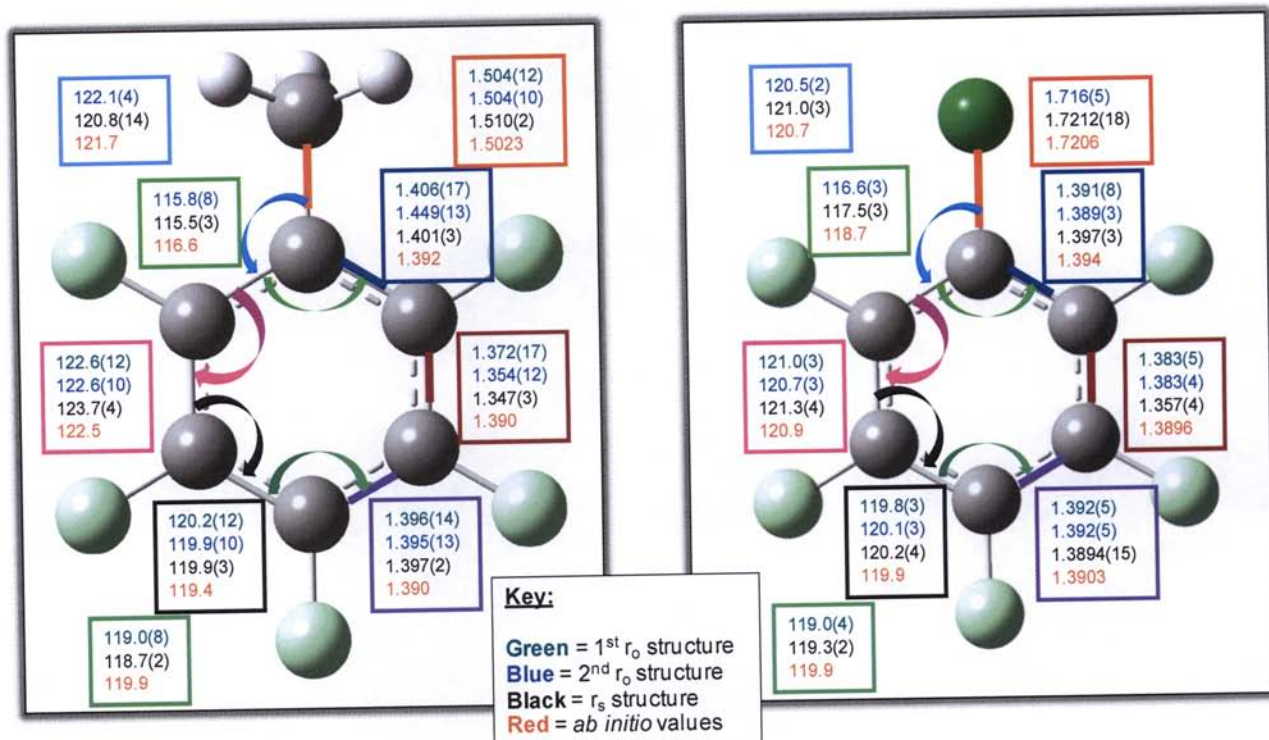


Figure 6.1: Comparison of pentaffluorotoluene vs chloropentafluorobenzene. The main structural observation obtained from this analysis was angle distortion located at the $\langle C_5-C_6-C_1$ angle.

First the bond length from the aromatic ring to either the methyl group (1.504(12) Å) or chlorine atom (1.716(5) Å) was observed and compared to their *ab initio* values (1.5023 and 1.7206 Å, respectively). The similarity between the experimental value and the predicted value serve to confirm that the calculations were reasonable. One unusual result that was first observed with pentaffluorotoluene was the angle of the aromatic ring at the carbon atom attached to the methyl group. The angles within this type of ring are typically around 120°. The experimental angle was found to be around 116° which agreed with *ab initio* values at this position. This angle was compared to that of

CPFB at the same position. It was found that this angle was also distorted at around 117°. These results lead to the conclusion that this angle distortion could be a result of the electron withdrawing fluorine atoms located around the ring. In order to determine if this was the case these results were compared to literature values for toluene which can be seen in Table 6.1 along with the structure of toluene seen in Figure 6.2.

Table 6.1: Comparison of PFTOL, CPFB and toluene^[2] values. Previous angle distortion in PFTOL and CPFB is not seen in the toluene structure

	<u>Pentafluorotoluene</u>	<u>Chloropentafluorobenzene</u>	<u>Toluene</u> ^[2]
A (MHz)	1036.61221(15)	1028.5412(2)	5729.3(2)
B (MHz)	1030.94086(16)	751.82072(17)	2517.4(9)
C (MHz)	516.92066(11)	434.3531(3)	1748.9(2)
μ (Debye)	1.976(11)	0.415	0.36
$\angle(\text{C}_5\text{-C}_6\text{-C}_1)^\circ$	115.5(3)	117.5(3)	119.0
I_a ($\text{u} \cdot \text{\AA}^2$)	487.5295(7)	491.35520(11)	294.9613(10)
I_b ($\text{u} \cdot \text{\AA}^2$)	490.21149(8)	672.20686(16)	200.7494(6)
I_c ($\text{u} \cdot \text{\AA}^2$)	977.6723(2)	1163.5213(8)	88.209(3)
P_{aa} ($\text{u} \cdot \text{\AA}^2$)	490.1772	672.1865	-3.00145
P_{bb} ($\text{u} \cdot \text{\AA}^2$)	487.4952	491.3348	91.21045
P_{cc} ($\text{u} \cdot \text{\AA}^2$)	0.0343	0.0204	0.029
κ	0.9782	0.0686	-0.6268

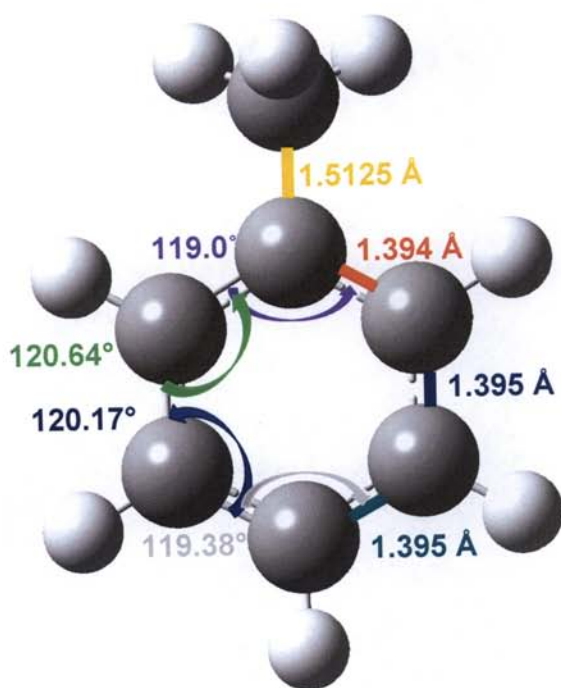


Figure 6.2: Experimental structure of toluene^[2]. Notice that the purple angle, corresponding to the distorted angle in PFTOL and CPFEB is closer to the predicted 120°.

When looking at the angle that was distorted in PFTOL and CPFEB, it is seen that for toluene this angle is very close to the predicted 120° at 119°. These results further supported the theory that angle distortion was being caused by the fluorine atoms. A final observation that was made from these results was odd behavior in the P_{cc} values. The P_{cc} value of CPFEB is close to zero, as expected, due to the fact that CPFEB is a planar molecule. The P_{cc} values for PFTOL and toluene, however are also close to zero. This is in contrast to *ab initio* values which predict the value to be around $1.5 \text{ u} \cdot \text{Å}^2$. This parameter is a measure of the extension of the methyl group out of the plane of the molecule, so the *ab initio* prediction should be reasonably close to the experimental value.

The lowering of P_{cc} can be explained by internal rotation effects. This outcome of the methyl rotation for both molecules will cause contamination of the moment of inertia around the methyl-top axis, skewing the experimental I_b value and lowering the value of P_{cc} ^[4]. If this value lowers to close to zero, it is indicative of a low energy barrier to internal rotation. This effect is the basis for estimation of the energy barrier from the P_{cc} value of the molecule as discussed in Chapter 4. It is notable that toluene, which has been thoroughly characterized previously, has a P_{cc} value that is very similar to PFTOL, and its barrier to Me group rotation is 0.34 kJ/mole^[5]. This suggests that our order of magnitude estimate from Chapter 4 of 0.1(2) kJ/mole for PFTOL is reasonable.

Further comparisons were done between the experimental results and similar molecules. Pentafluorotoluene was compared to pentafluorobenzene and chloropentafluorobenzene was compared to chlorobenzene. These results can be seen in Tables 6.2 and 6.3, respectively. Since the structure of pentafluorobenzene has not been determined experimentally, information for this molecule comes from the *ab initio* calculation that was performed. For this reason, only the *ab initio* values of PFTOL are used to compare the two molecules. Comparison of the aromatic ring angle in pentafluorobenzene shows that this angle is predicted at 119.2°, close to the expected value 120°. This contrasts the theory that electronegative substituents were the cause of the angle distortion, possibly because pentafluorobenzene is the only molecule in the series without a bulky substituent attached to first carbon of the ring.

Table 6.2: Comparison of *ab initio* values of PFTOL to pentafluorobenzene.

	Pentafluorotoluene	Pentafluorobenzene ^[3]
A (MHz)	1035.2031	1476.3234
B (MHz)	1021.4101	1026.3894
C (MHz)	515.7608	605.4561
μ (Debye)	2.522	1.716
$\angle(\text{C}_5\text{-C}_6\text{-C}_1)/^\circ$	116.6	119.2

Table 6.3: Comparison of CPFB to chlorobenzene.

	Chloropentafluorobenzene		Chlorobenzene ^[1]	
	³⁵ Cl	³⁷ Cl	³⁵ Cl	³⁷ Cl
χ_{aa} (MHz)	-79.521(11)	-62.68(2)	-71.25	-56.1
χ_{bb} (MHz)	43.598(4)	34.39(3)	36.88	29.03
χ_{cc} (MHz)	35.923(15)	28.29(6)	34.37	27.07
P_{aa} ($\text{u} \cdot \text{\AA}^2$)	672.1866	688.0581	320.5345	329.7352
P_{bb} ($\text{u} \cdot \text{\AA}^2$)	491.3349	491.3342	89.1187	89.119
P_{cc} ($\text{u} \cdot \text{\AA}^2$)	0.0209	0.0201	0.0453	0.0464
η (MHz)	-0.0965	-0.0973	-0.0352	-0.0349
$Q(^{35}\text{Cl})/Q(^{37}\text{Cl})$	1.2698		1.2697	
μ (Debye)	0.415		1.641	
$R(\text{C}_6\text{-Cl})/\text{\AA}$	1.716(5)		1.739	
$\angle(\text{C}_5\text{-C}_6\text{-C}_1)/^\circ$	117.5(3)		121.7	

The data obtained for chlorobenzene comes from a previously published microwave experiment^[1]. Initial comparison of the bond distance between the aromatic ring and chlorine atom shows similar values for both CPFB and chlorobenzene. This, again, confirms the accuracy of the experimental results for CPFB. When comparing the angle of the aromatic ring that is distorted in CPFB at 117.5(3) $^\circ$ as seen in Figure 6.1, it is seen in chlorobenzene that the

angle is very slightly distorted in the opposite direction, at 121.7° . This evidence further confirms the suspected effect of electronegative atoms attached to the ring since these atoms are not part of chlorobenzene. In addition, the lack of an effect in pentafluorobenzene leads us to believe that the presence of a second bulky substituent at the non-fluorinated ring position may also be necessary for the angle distortion. Finally, for CPFEB and chlorobenzene, the asymmetry parameter, η , was observed. The electric field gradient around the C–Cl bond seems to be similar in both molecules, with CPFEB being slightly more distorted. This is, again, likely due to the effects of the fluorine substituents in CPFEB.

In order to further observe the effects of the electronegative substituents, electrostatic potential (ESP) maps were done on both PFTOL and CPFEB as well as the similar molecules toluene, xylene, chlorobenzene and pentafluorobenzene. These maps can be seen in Figure 6.3. From these calculations it can be seen that the presence of the fluorine atoms attached to the benzene ring has a significant effect on the molecule. The ring current normally present in aromatic species is interrupted by the electron-withdrawing fluorine atoms causing a much more positive electrostatic potential near the center of the ring. This effect is likely the cause of the angle distortion that is seen in both PFTOL and CPFEB, although the lack of a similar effect in pentafluorobenzene is still surprising, considering its apparent electrostatic similarity to PFTOL and CPFEB. As mentioned above, the effect is probably more complicated and may also depend on substituent size and other factors.

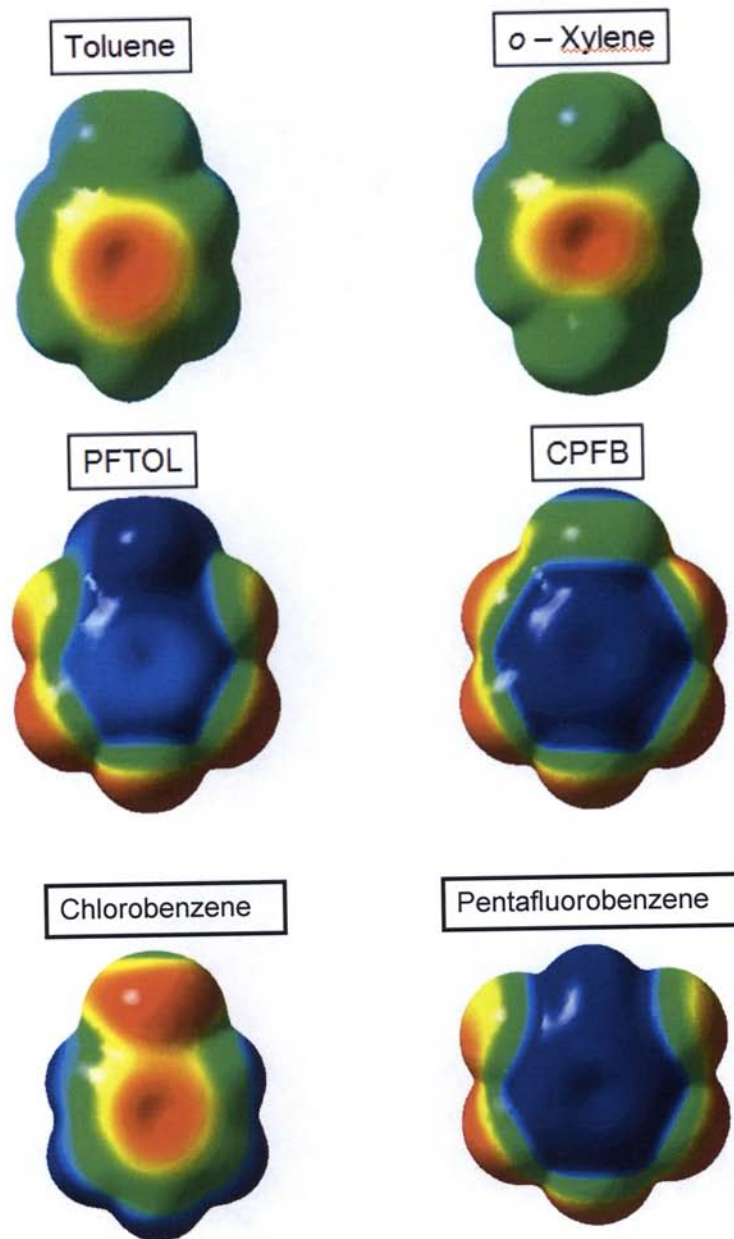


Figure 6.3: Electrostatic potential maps calculated to observe electronegative substituent effects. Colors range from blue, which indicates a positive electrostatic potential, to red, indicating a negative electrostatic potential.

6.2 Future work

Additional work is needed to finalize the visible emission studies discussed in Chapter 3. The products formed from the discharge nozzle still need to be fully characterized. Numerous literature searches indicate that radicals are forming in the discharge. The radicals are likely H, CH, C₂ and/or C₃, but further characterization needs to be done to confirm this. One way of further characterizing these products is to continue emission spectra acquisition from molecules similar to toluene and xylene. The next logical step in these experiments is to run benzene through the spectrometer and observe the emission spectrum that results to see if similarities occur in the 400 – 500 nm region. Smaller fragments such as C₂ or C₃ have indicated lines present in the 450 – 500 nm region. If the fragments that are forming are small, the results from benzene would also be expected to agree with the results for toluene and xylene discussed in Chapter 3. This will be followed by pentafluorobenzene and finally pentafluorotoluene; however, these experiments cannot currently be performed, since the PMT has stopped working.

Future work will also be done on the results of the microwave studies of chloropentafluorobenzene and pentafluorotoluene. Dipole moment determinations need to be improved for both molecules and, to finish up the microwave study of PFTOL, the internal rotation of the methyl group needs to be fully characterized. Estimation of the energy barrier was done using the P_{cc} value of the molecule, but this value is very uncertain since it was necessary to extrapolate to much lower barriers than were included in the tables used for the

estimate (see Chapter 4). Future work can be done by determining the energy barrier to internal rotation using a computer program such as Xiam^[6] to fit the observed torsionally excited state transitions (identified by first order Stark effects) to determine an experimental barrier. The estimated barrier to rotation should help accurately assign torsional state lines, making the determination much easier. Finally, it would be interesting to determine the structure of pentafluorobenzene using microwave spectroscopy in order to perform a more accurate comparison with the PFTOL structure.

6.3 Conclusions

The studies described in this work were in preparation for the construction of a rapid scan midinfrared spectrometer for the study of free radicals and weakly-bound complexes of atmospheric species. A series of visible emission spectroscopy experiments were done in order to characterize a pulsed discharge nozzle. Computer programs were first written in order to control the visible emission spectrometer. The goal of these experiments was then to determine the products that the PDN was forming and attempt to optimize the conditions for free radical formation. We found that when toluene and xylene emission spectra were measured the 400 – 450 nm region was similar for both molecules and indicated the H and CH radical were forming.

Since the radical that would eventually be studied in this way was the pentafluorobenzyl radical, information was needed about the radical's precursor,

pentafluorotoluene. As no literature information was available on the structure of this molecule, a microwave spectroscopy study was initiated. The rotational spectra of the normal and five ^{13}C species of PFTOL have been assigned and the structure has been determined. After this was done a second microwave spectroscopy experiment was done studying chloropentafluorobenzene in order to compare it to PFTOL. The rotational spectrum of the normal and five isotopologue species of CPFEB have also been assigned and the structure determined. In both species, it was found that the $\angle\text{C}_5\text{-C}_6\text{-C}_1$ angle was distorted due to the presence of the fluorine atoms.

As described above, some future work still needs to be done to complete these studies. Once this is done work can move on to completion of the rapid scan midinfrared spectrometer in order to recreate an experiment studying the $\text{CO}_2\text{-SO}_2$ weakly-bound complex. Completion of this experiment will confirm a working midinfrared spectrometer that can then be used to study various environmental species such as free radical and weakly bound complexes of common pollutants such as HCFCs.

References: Chapter 6

- [¹] Oh, J.J.; Park, I.; Wilson, R.J.; Peebles, S.A.; Kuczkowski, R.L.; Kraka, E.; Cremer, D. *J. Chem. Phys.* **2000**, *113*(22).
- [²] Amir-Ebrahimi, V.; Choplin, A. *J. Mol. Spec.* **1981**, *89*, 42.
- [³] Gaussian 03, Revision C.02, M. J. Frisch, G. W. Trucks, H. B. Schlegel, G. E. Scuseria, M. A. Robb, J. R. Cheeseman, J. A. Montgomery, Jr., T. Vreven, K. N. Kudin, J. C. Burant, J. M. Millam, S. S. Iyengar, J. Tomasi, V. Barone, B. Mennucci, M. Cossi, G. Scalmani, N. Rega, G. A. Petersson, H. Nakatsuji, M. Hada, M. Ehara, K. Toyota, R. Fukuda, J. Hasegawa, M. Ishida, T. Nakajima, Y. Honda, O. Kitao, H. Nakai, M. Klene, X. Li, J. E. Knox, H. P. Hratchian, J. B. Cross, V. Bakken, C. Adamo, J. Jaramillo, R. Gomperts, R. E. Stratmann, O. Yazyev, A. J. Austin, R. Cammi, C. Pomelli, J. W. Ochterski, P. Y. Ayala, K. Morokuma, G. A. Voth, P. Salvador, J. J. Dannenberg, V. G. Zakrzewski, S. Dapprich, A. D. Daniels, M. C. Strain, O. Farkas, D. K. Malick, A. D. Rabuck, K. Raghavachari, J. B. Foresman, J. V. Ortiz, Q. Cui, A. G. Baboul, S. Clifford, J. Cioslowski, B. B. Stefanov, G. Liu, A. Liashenko, P. Piskorz, I. Komaromi, R. L. Martin, D. J. Fox, T. Keith, M. A. Al-Laham, C. Y. Peng, A. Nanayakkara, M. Challacombe, P. M. W. Gill, B. Johnson, W. Chen, M. W. Wong, C. Gonzalez, and J. A. Pople, Gaussian, Inc., Wallingford CT, 2004.
- [⁴] Serafin, M.M.; Peebles, S.A. *J. Phys. Chem. A* **2008**, *112*, 1473-1479.
- [⁵] Kreiner, W.A.; Rudolph, H.D.; Tan, B.T. *J. Mol. Spec.* **1973**, *48*, 86 – 99.
- [⁶] H. Hartwig, H.; Dreizler, Z.; *Naturforsch, A Phys. Sci.* **1996**, *51*, 923–932.






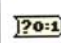

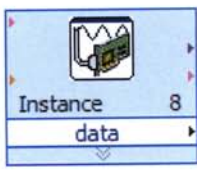

Appendix A – Constants and Variables






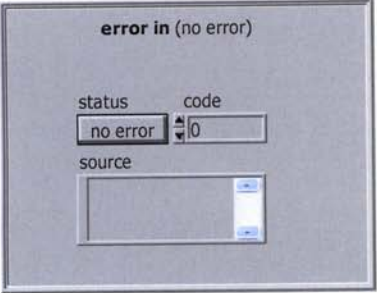
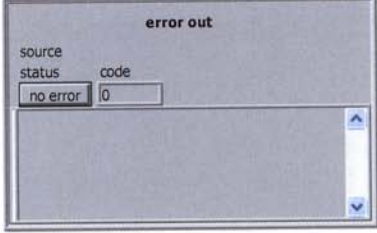

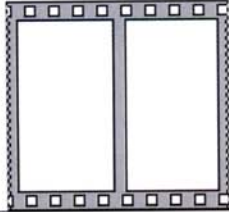
<u>Variable</u>	<u>First Location</u>	<u>Definition</u>
E_v	Chapter 1	Energy of a particular vibrational transition
h	Chapter 1	Planck's constant
ν	Chapter 1	Frequency
v	Chapter 1	Vibrational quantum number
π	Chapter 1	pi
k	Chapter 1	Force constant
μ	Chapter 1	Reduced mass
$G(v_i)$	Chapter 1	Vibrational term value
ω_i	Chapter 1	Classical vibration wavenumber
I_a	Chapter 2	Moment of inertia around the a -axis
I_b	Chapter 2	Moment of inertia around the b -axis
I_c	Chapter 2	Moment of inertia around the c -axis
m_i	Chapter 2	Mass of a particular atom within a molecule
r_i	Chapter 2	Distance of a particular atom within a molecule from the center of mass
J	Chapter 2	Quantum number representing the total angular momentum

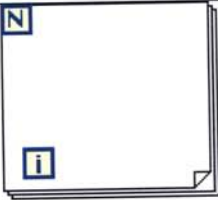


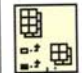





A, B, C	Chapter 2	Rotational constants corresponding to their particular principal axes
K_a, K_c	Chapter 2	Quantum number representing the projection of the angular momentum along the molecule's top axis
a	Chapter 2	a -axis coordinate
b	Chapter 2	b -axis coordinate
c	Chapter 2	c -axis coordinate
D_J, D_{JK}, D_K	Chapter 2	Centrifugal distortion constants
E_r	Chapter 2	Energy of a particular rotational transition
M	Chapter 4	Quantum number representing the projection of the angular momentum along an electrical field axis
E	Chapter 4	Strength of an electrical field
μ	Chapter 4	Dipole moment of the molecule
A, B	Chapter 4	Stark coefficients
P_{aa}, P_{bb}, P_{cc}	Chapter 4	Planar moments – measure of the planarity of the molecule along the corresponding axis

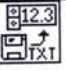



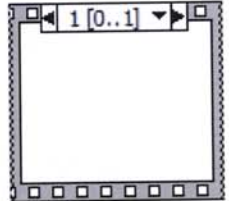


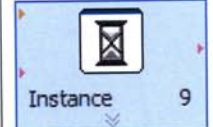
K	Chapter 4	Asymmetry parameter – measure of the amount of asymmetry of a molecule. The closer to 0 the value is, the more asymmetric the molecule appears
V_3	Chapter 4	Energy barrier to internal rotation
A_{00}, B_{00}, C_{00}	Chapter 4	Experimental rotational constants
A_r, B_r, C_r	Chapter 4	Rigid-rotor rotational constants
W^2_{00}	Chapter 4	Perturbation coefficient
F	Chapter 4	Reduced rotational constant of the methyl top
s	Chapter 4	Reduced energy barrier to internal rotation
F	Chapter 5	Quantum number representing the total angular momentum of a molecule when its rotational angular momentum couples with nuclear spin from a quadrupolar nucleus
$\chi_{aa}, \chi_{bb}, \chi_{cc}$	Chapter 5	Quadrupole coupling constants
η	Chapter 5	Nuclear asymmetry parameter – measure of the electric field gradient around a quadrupolar nucleus

Appendix B – LabVIEW Controls, Indicators and Functions

<u>Icon</u>	<u>Name & Type</u>	<u>Use</u>
	Absolute value – Function	Returns the absolute value of the input
	Add – Function	Calculates the sum of the two inputs
	Add Array Elements – Function	Calculates the sum of all the elements in a one-dimensional array.
	And – Function	Decides whether two Boolean inputs are both True, if yes, output is True, if not, a False output is returned
	Array Size – Function	Calculates the number of elements in each dimension of an input array
	Boolean to (0,1) - Function	Converts False/True value to a numeric 0 or 1, respectively
	Build Array – Function	Concentrates multiple elements or arrays into an n-dimensional array
	DAQ Assistant – Function	Express VI built into the LabVIEW software that helps with data collection from the DAQ board
	DAQmx Clear Task – Function	Stops the task if this has not already been done and clears it

	DAQmx Control Channel – Function	Creates a channel to generate digital pulses according to various controls wired to the function
	DAQmx Start Task – Function	Transitions the task into the running state to begin measurement
	DAQmx Wait Until Done – Function	Waits for data measurement to finish
	Delete From Array – Function	Deletes a specified value from the input array
	Divide – Function	Divides the two input values and returns the result
	Error In – Indicator	Displays any error that may be present at the beginning of VI execution
	Error Out – Indicator	Displays any error that occurs during execution of the program
	File Path – Control	Specifies the file name for the output file and the location for it to be saved
	Flat Sequence Structure – Function	Executes the code within one or more frames sequentially

	For Loop – Function	Repeats all code within the loop N times.
	Greater or Equal? – Function	Determines whether x is greater than or equal to y
	In Range and Coerce – Function	Determines whether a value falls between the upper and lower limits wired to the function. Returns either a numeric value that has been coerced or a boolean T/F value specifying whether or not the value is in range
	Index Array – Function	Returns either an element or sub-array of an n-dimensional array
	Interleave 1D Array – Function	Interleaves corresponding values, such as (x,y) coordinates into a single array
	Less? – Function	Determines whether x is less than y
	Multiply – Function	Calculates the value from multiplying two inputs
	Numeric Control – Control	Specifies any numeric conditions the user might want to control
	Or Array Elements – Function	Boolean function that returns a False value if all the values in a Boolean array are False, otherwise returns True

	<p>Read From Spreadsheet – Function</p>	<p>Reads the values from a spreadsheet file often provided through a File Path control and sends the data into the program</p>
	<p>Search 1D Array – Function</p>	<p>Searches a 1D array for a specified value and returns the location of that value</p>
	<p>Select – Function</p>	<p>Returns the value wired to the T option if the boolean input is T. Returns the value wired to the F option otherwise.</p>
	<p>Square Waveform</p>	<p>Generates a waveform containing a square wave with values of either 0 or 1.</p>
	<p>Stacked Sequence Structure – Function</p>	<p>Executes the code within one or more frames sequentially</p>
<p>stop</p> 	<p>Stop Button – Control</p>	<p>Boolean control that can be wired to any function that may stop a continuous action. This is often wired to the conditional terminal of a While Loop.</p>
	<p>Subtract – Function</p>	<p>Calculates the difference between the two inputs</p>
	<p>Time Delay – Function</p>	<p>Express VI built into the LabVIEW software that adds any time delay necessary</p>



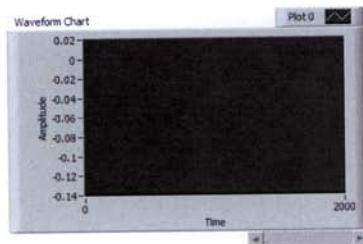
Wait (ms) – Function

Waits a specified number of milliseconds before continuing to the next function



Wait Until Next ms Multiple – Function

Waits until the next specified millisecond multiple to continue. Often used within loops to control timing of loop execution (ex: For Loop executes every 200 ms.)



Waveform Chart – Indicator

Shows data plotted as a scrolling waveform chart. Displays data as it's being recorded.



Waveform Graph – Indicator

Displays data as a waveform graph. Data is plotted as the final step in the program after all the data has been recorded



While Loop – Function

Repeats the code within the loop until the conditional terminal at the bottom right receives a particular value



Write to Spreadsheet File – Function

Writes acquired data to the spreadsheet file specified by the File Path indicator

Appendix C – LabVIEW Programs

Appendix C covers the data analysis programs written using the LabVIEW programming software. Data analysis programs cover VIs that analyze broadband spectra from the chirped-pulse broadband spectrometer constructed at EIU. These VIs are entitled BroadbandSpectrum.vi and BroadbandSpectrumLineList.vi. Further data analysis VIs are discussed that eliminate monomer lines from a spectrum (MonomerEliminator.vi) as well as a program that gives a preliminary line list from comparing experimental data to SPCAT (SPCAT v. Origin comparison.vi). Relevant information about each program is contained in the figure captions.

Figure C.1: Front panel and block diagram of AnalogNozzleFire.vi. This program runs using the same theory as the Nozzlefire.vi in Chapter 3, with exception to the type of control being used to fire the nozzle. Nozzlefire.vi uses a digital counter attached to the DAQ board in the computer. AnalogNozzleFire.vi attempts to fire the nozzle using one of the analog channels present on the DAQ board.

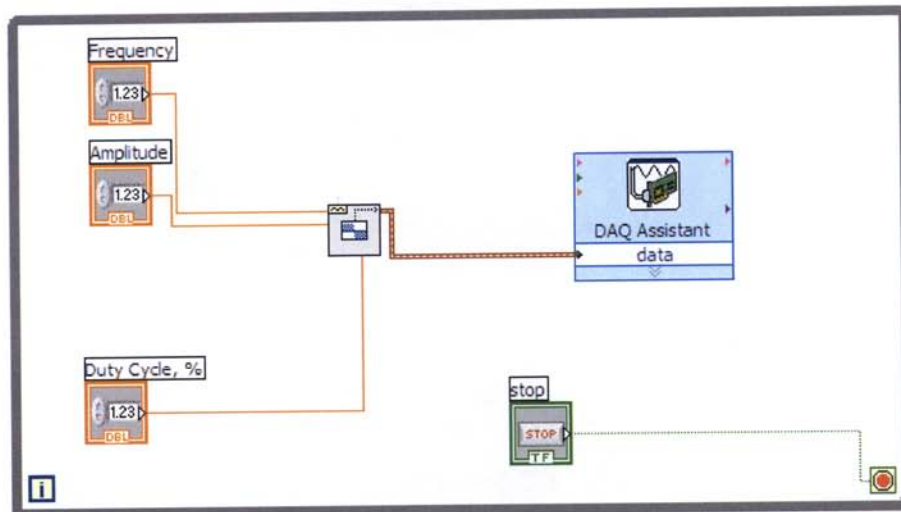
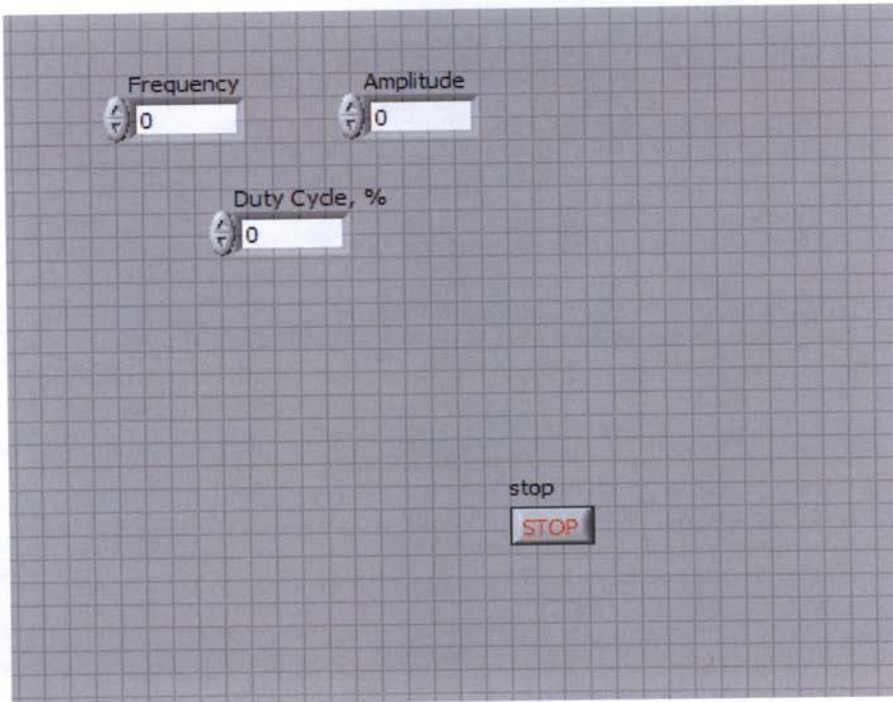
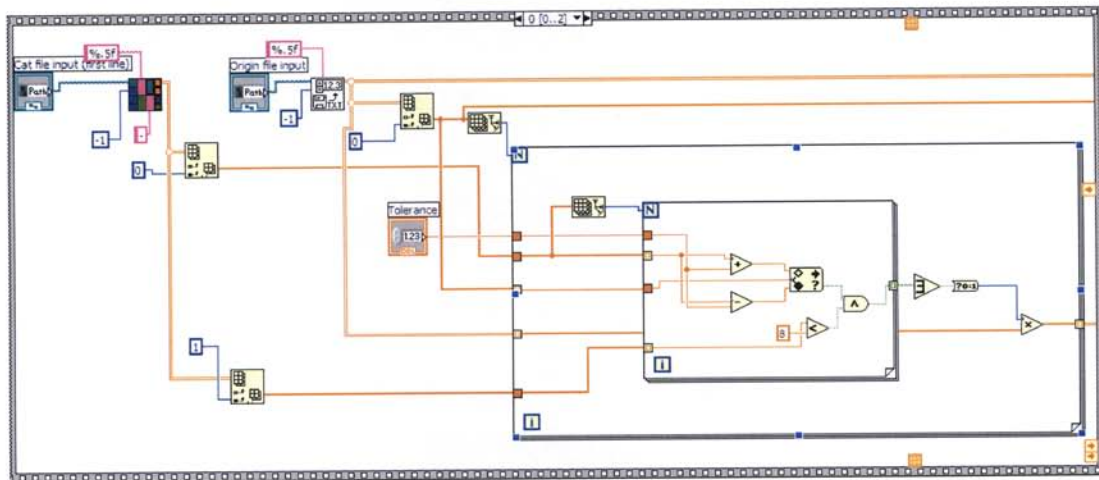
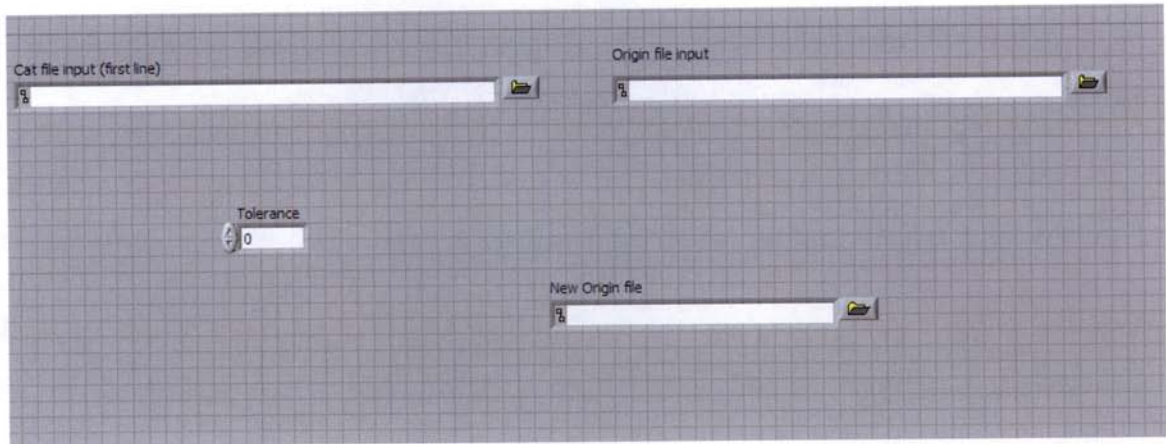


Figure C.2: Front Panel and Block Diagram of MonomerEliminator.vi. This program takes a spectrum file, such as an Origin file and compares it to the predicted spectrum in the form of a .cat file from SPCAT to obtain a preliminary line list. It then takes the Origin data from the line list and compares the various Y values to a threshold intensity controlled by the user on the front panel through the Tolerance control. Any lines above this intensity are separated out of the array and zeroed-out. This results in a spectrum with the lines that were present above the Tolerance threshold to now be zeroed out.



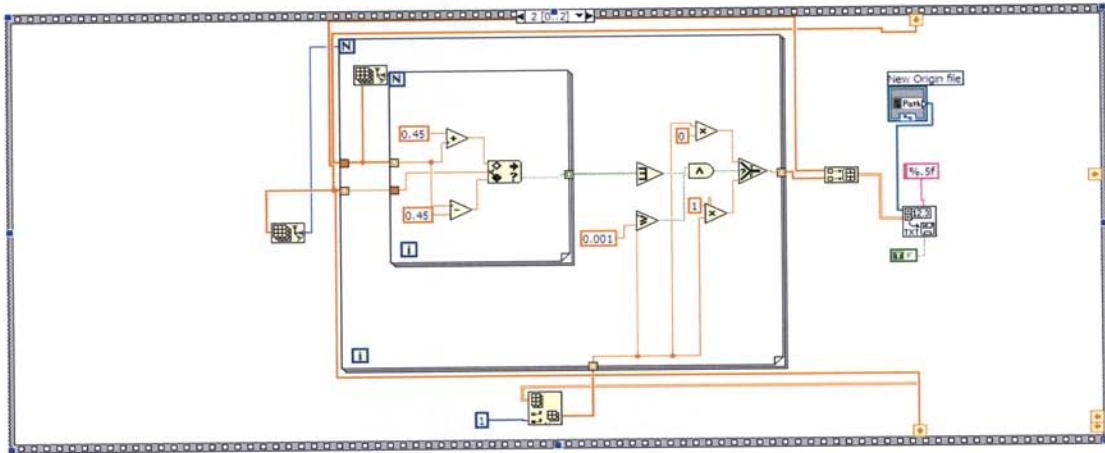
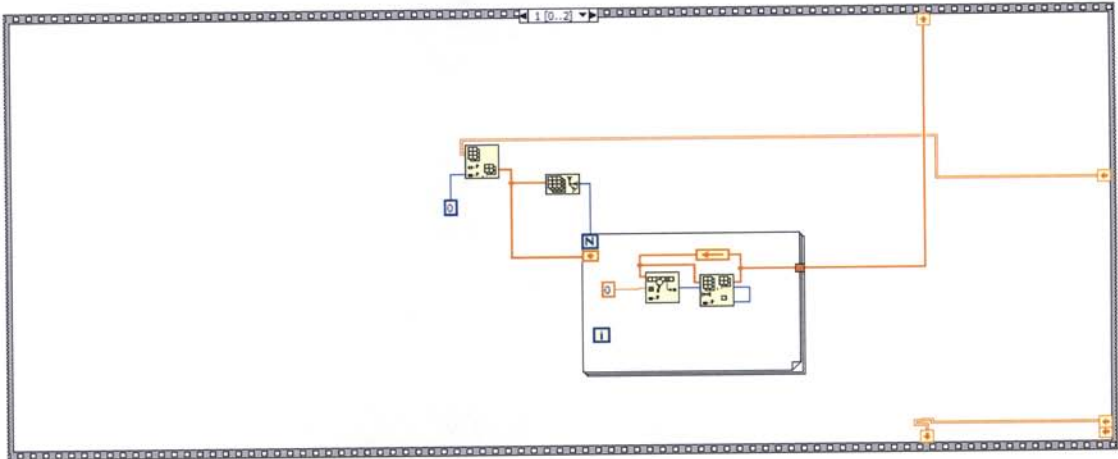
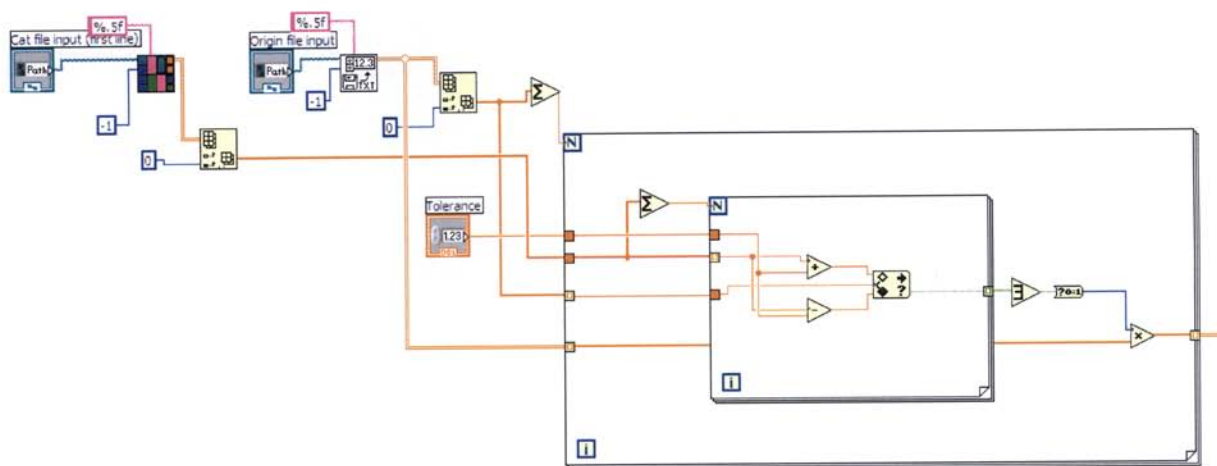
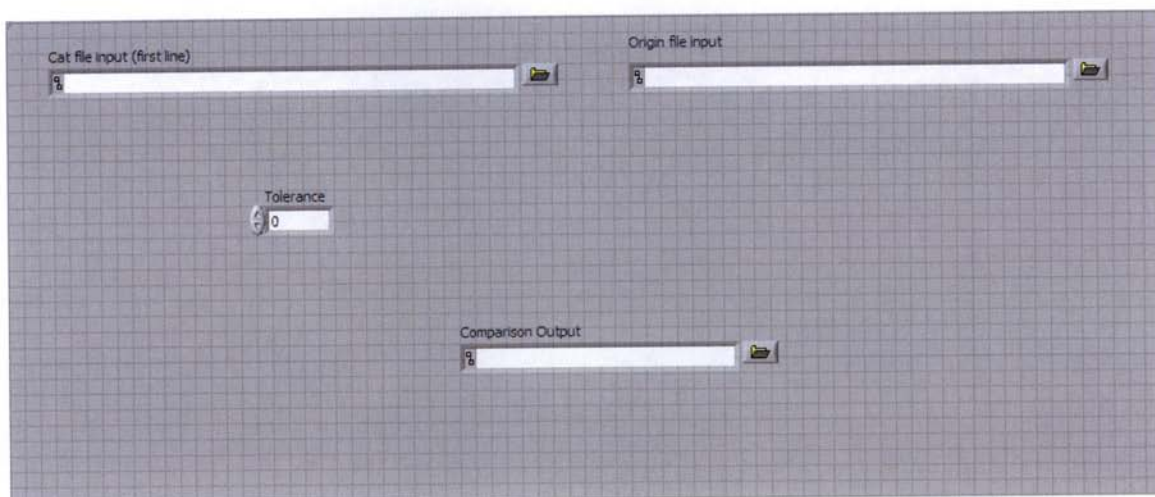


Figure C.3: Front Panel and Block Diagram of SPCAT v. Origin comparison.vi. This program uses two input files, a .cat file produced by SPCAT and an Origin file containing spectrum data. These files are put into the program through the front panel, where the VI then compares the frequency data of both input files to see if there's a match within an uncertainty also specified on the front panel through the Tolerance control. If there is a match, the program saves the data into an array, producing a preliminary line list that can be used to begin an assignment. This program is also the basic beginning of MonomerEliminator.vi, where this preliminary line list is then subtracted from the experimental data in order to zero out monomer lines.



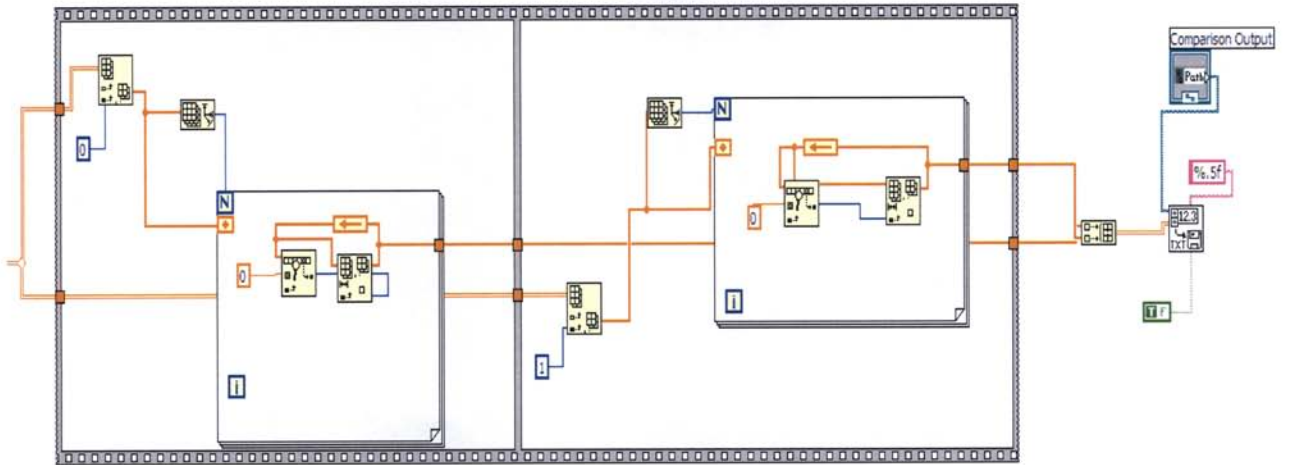
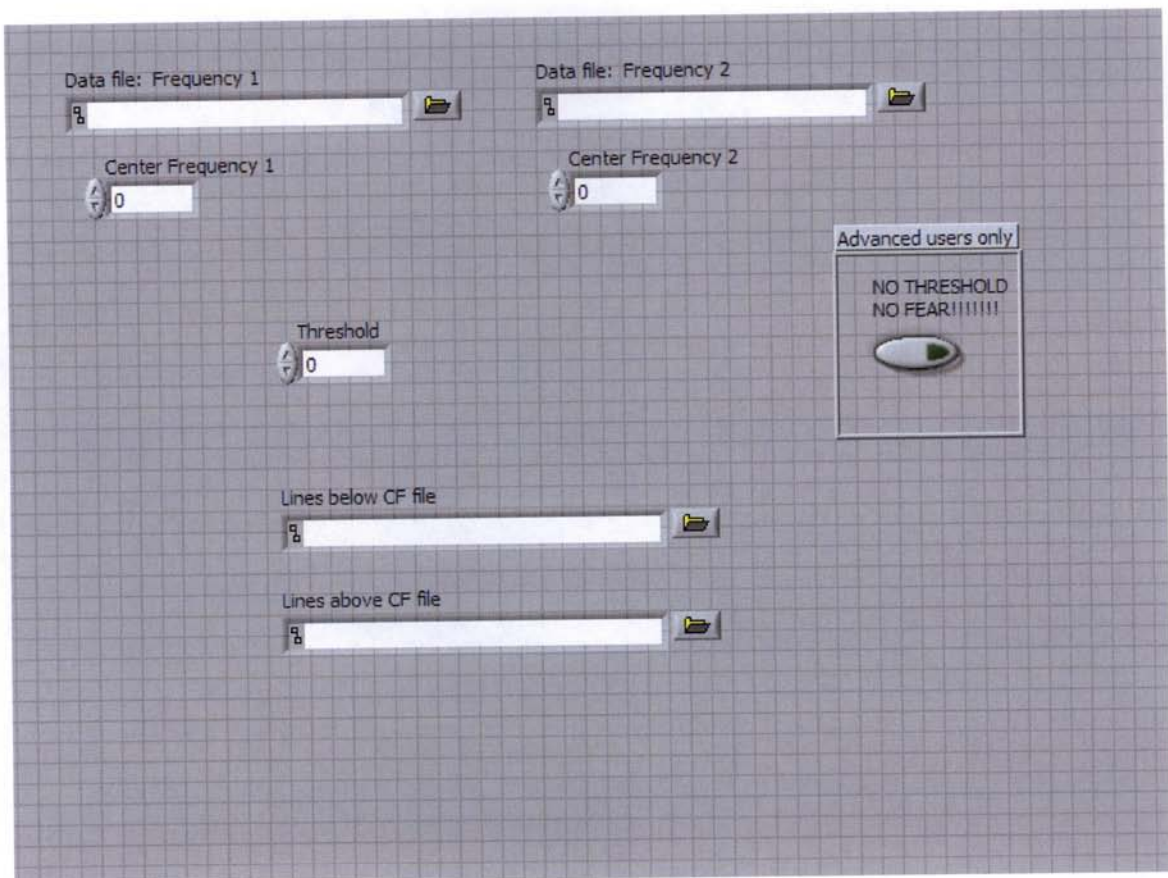
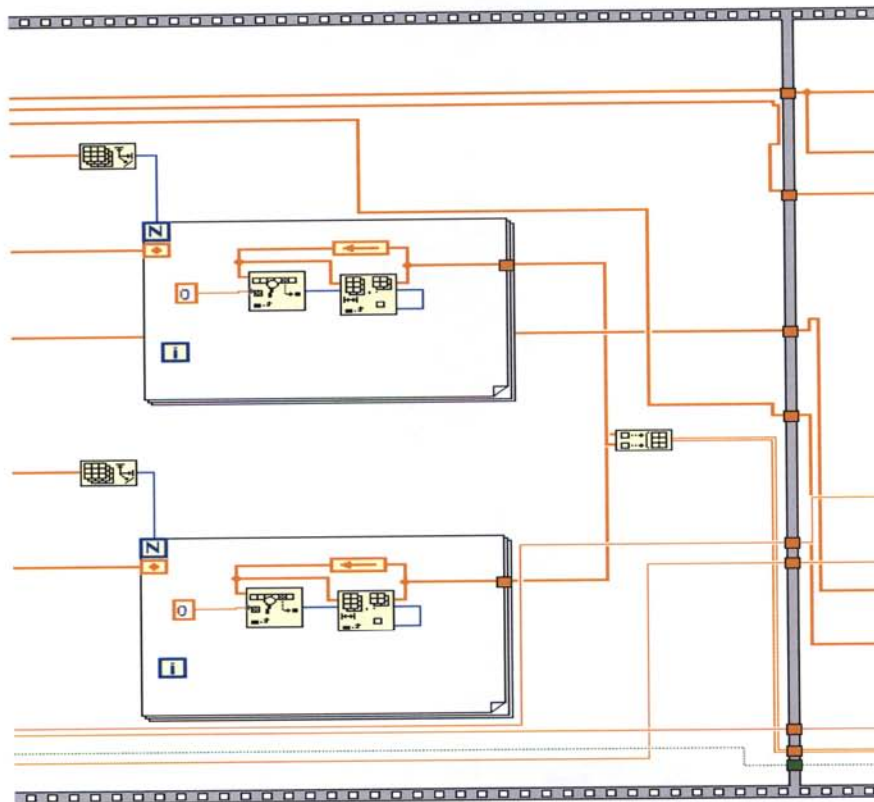
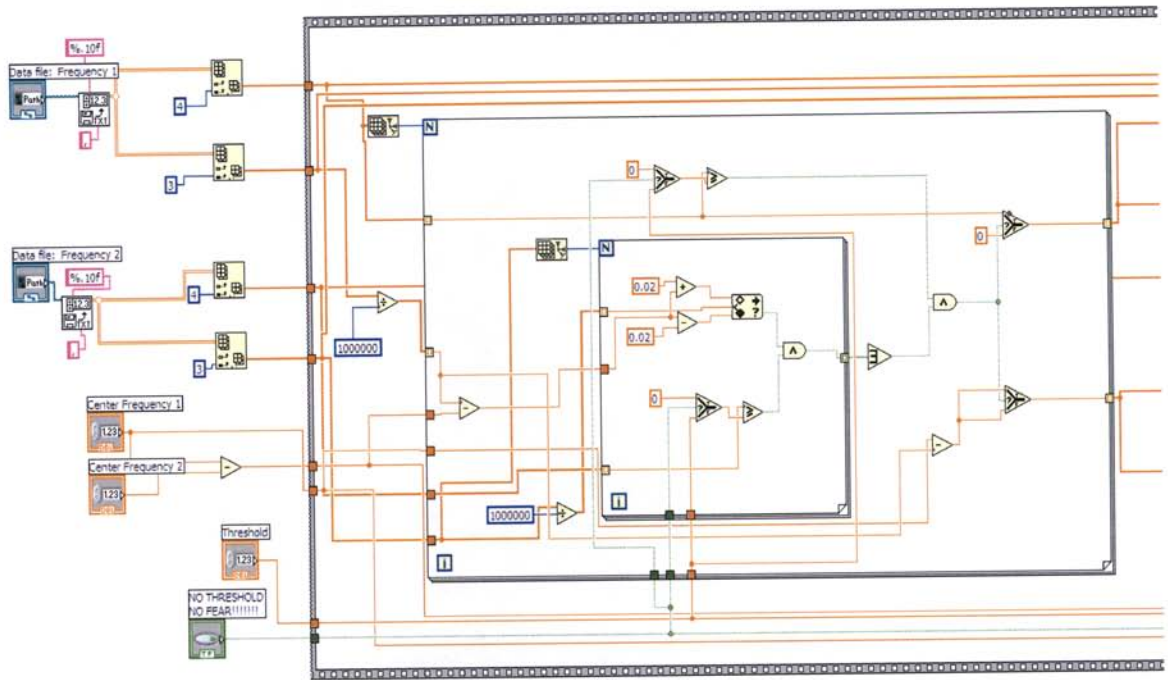


Figure C.4: Front Panel and Block Diagram of BroadbandSpectrumLineList.vi. This program inputs two .csv files on the front panel from the output of a broadband spectrometer. One of these files is the original broadband output, the second one is after the frequency has been stepped down. The program finds a peak in the first file according to an intensity threshold from the front panel control labeled as such, then searches the second file for a peak a set frequency above the first peak. This set frequency comes from the difference between the two center frequencies taken in the block diagram. These center frequencies, along with the threshold value are set by the user on the front panel through the appropriately labeled controls. The program then repeats the same thing, only searching for peaks below the frequencies in the first file. Two files are output; one is a line list of peaks occurring above the broadband center frequency. The second is the same type of list with peaks occurring below the center frequency.





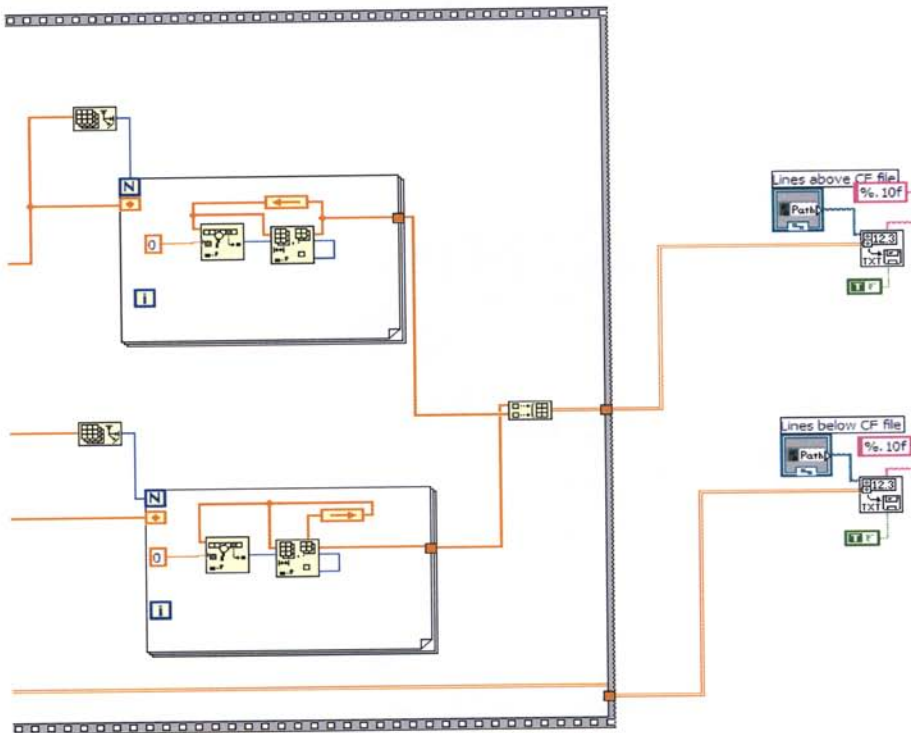
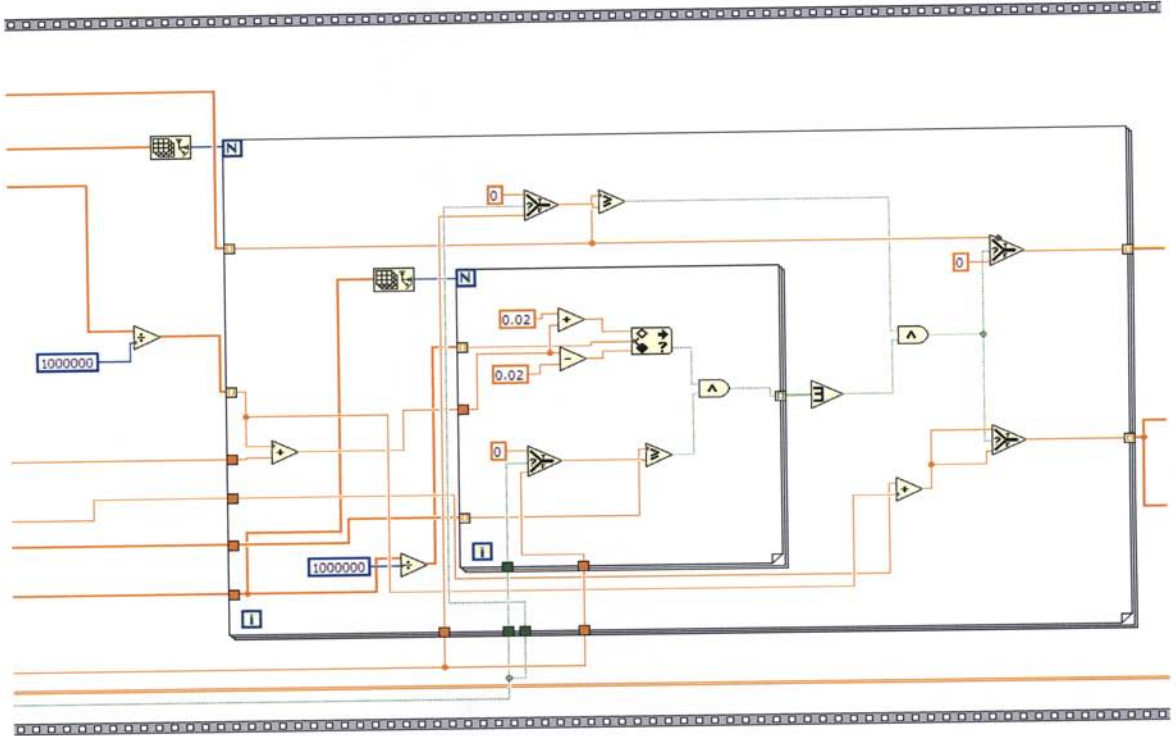


Figure C.5: Front panel and block diagram of BroadbandSpectrum.vi. This program uses the same two input files as Figure C.4. Inputs also include the center frequencies that were used during the spectrum acquisition. This program compares the peaks to a threshold in a manner similar to Figure C.4 to see which will stay and which get zeroed out as noise. Rather than producing a line list, this program converts the lines to their true frequencies by either subtracting or adding the center frequency to the frequency offset and outputs the true broadband spectrum of the molecule rather than the frequency offset from the center frequency.

